Defect Structure in Ultrafine-grained Silver and a Copper-Silver Alloy Processed by Severe Plastic Deformation

Zoltán Hegedűs

– Ph.D. Dissertation –

Supervisor: Prof. Jenő Gubicza, DSc
Eötvös Loránd University, Department of Materials Physics

Eötvös Loránd University, Doctoral School of Physics
Materials Science and Condensed Matter Physics program

Head of doctoral school: Prof. László Palla
Head of doctoral program: Prof. János Lendvai

Budapest
2013

Contents

Preface

In the last decades severe plastic deformation (SPD) of metals became one of the most important and most intensively investigated field of the materials science, because of the outstanding mechanical strength of SPD-processed ultrafine-grained (UFG) metals. Besides the strength there is another very important factor, namely, the ductility of materials. We are able to design very light materials with high strength or toughness, but to combine these features with ductility is still a challenge. From this point of view stacking fault energy (SFE) is one of the most important parameters of a material. SFE influences the mechanisms of plastic deformation, therefore it has a strong effect on the ductility. Usually the lower the SFE the better the ductility. In the literature the microstructure and the mechanical properties of low SFE alloys and pure metals with medium or high SFE processed by SPD were widely investigated, however studies on SPD processed pure face centered cubic (fcc) metals with low SFE, such as silver have not been reported. In low SFE alloys the effect of alloying and SFE are superimposed, therefore the sole influence of SFE on the defect structure can not be extracted from these results.

The main topic of this thesis is the study of the defect structure and its thermal stability in SPD-processed silver samples with different impurity contents. In addition, an UFG Cu-alloy processed by SPD is also investigated, which contains silver precipitates. In chapter 1 I would like to introduce the SPD techniques, which were used to produce UFG samples. In addition the microstructure and the mechanical behavior of SPD-processed metals are overviewed. Then in chapter 2 the applied measurement techniques will be discussed focusing on the x-ray line profile analysis (XLPA) . In the second part of the thesis the own research results are presented. In chapters 3, 4 and 5 I will show the evolution of microstructure in pure silver samples during equal-channel angular pressing (ECAP) , their room temperature (RT) and high temperature thermal stability, respectively. After that in chapter 6 the evolved microstructure of silver during processing by high-pressure torsion (HPT) is investigated with special attention to its thermal stability. Finally, chapter 7 deals with the defect structure of a copper-silver alloy produced by rolling and subsequent heat treatment in order to achieve a combination of good ductility and high strength.

Part I

Literature Overview and Experimentals

Chapter 1

Literature Overview

In this chapter the fundamentals related to the topic of my thesis are briefly reviewed. First, the SPD methods applied in this research are introduced, then, the significance of the stacking fault energy regarding the mechanical properties and the deformation mechanisms of fcc metals is discussed according to the literature.

1.1 Severe Plastic Deformation

Although the physical and mechanical properties of metals are determined by several factors, the average grain size generally plays a very significant role. In the early 1950s two scientists (Hall and Petch) found the same relationship between the yield strength and the grain size, independently [1, 2]. Thus the formula describing the correlation between the grain size (d) of a polycrystalline material and its yield strength (σ_y) is called Hall–Petch-equation:

$$\sigma_y = \sigma_0 + kd^{-1/2}, \tag{1.1}$$

where σ_0 is the friction stress and k is a constant depending on the material. From (1.1) it follows, that the yield strength increases with the reduction of the grain size. Therefore high strength materials can be processed by refining the grain size into UFG or nanocrystalline regimes. The formal definition of ultrafine-grained materials is that they have an average grain size smaller than $\sim 1\,\mu$m. Additionally for bulk UFG metals there are other requirements of fairly homogeneous and equiaxed microstructure. At the same time polycrystalline materials having grain size smaller than $\sim 100\,$nm are termed as nanocrystalline materials.

Two different approaches have been developed to produce UFG metals which are referred to as 'bottom-up' and 'top-down' methods [3].

In the bottom-up approach nanoparticles or individual atoms are assembled to a dense solid material. There are different methods of this approach, like inert gas condensation [4, 5], electrodeposition [6], isostatic pressing or hot isostatic pressing [7], however this list is far from complete. These techniques are often limited to the production of small samples that are generally not appropriate for structural applications. Additionally, the final product contains some residual porosity and also contamination which is introduced during the fabrication procedure.

In the top-down approach a coarse grained bulk material is processed through heavy straining in order to produce UFG materials. Using this approach one can avoid the small product sizes, the residual porosity and the presence of contamination which are unavoidable using the bottom-up approach. This approach was first applied in the early 1990s on pure metals and alloys [8–10].

In order to produce UFG samples from coarse-grained bulk materials, it is necessary to impose exceptionally high strain in order to introduce high density of dislocations, which can form grain boundaries. The processing methods in which very high strain is imposed on a bulk coarse-grained solid, without significant change in any dimension of the work-piece, are referred to as severe plastic deformation methods. During SPD, dislocations with very high density are formed and their rearrangement into boundaries lead to a very significant grain-refinement. This usually results in UFG metals with a typical grain size of several ten to several hundreds of nanometers.

Several SPD processing methods were developed since the invention of the applicability of the high imposed strain to produce metals and alloys with superior properties. The most often applied and most established[1] SPD methods are ECAP [9, 12–14], HPT [15–17], multi-directional forging [18, 19] and accumulative roll-bonding [20, 21].

In the following subsections rolling, ECAP and HPT will be introduced in details as these techniques were used to produce the UFG samples in my studies.

1.1.1 Rolling

Rolling is the most widely used deformation process, in which the metal workpiece is passed through between two rolls and a reduction in thickness results from compressive stresses.

Rolling may be characterized by its temperature. Hot rolling is basically used for homogenization of cast metals. The temperature is above the recrystallization temperature, therefore recrystallization occurs during/after rolling, which prevents work hardening, but able to reduce the cast inhomogeneities by achieveing an equiaxed grain structure.

Cold rolling is when the temperature is below the recrystallization temperature. In this case the induced lattice defects can not annihilate after the rolling process, and therefore strain hardening and grain refinement occurs. Hence cold rolling may be considered as an SPD method.

Usually in SPD methods a basic requirement is not to reduce the size of the sample too much, therefore the deformation process can be repeated several times. As a consequence, the application

[1] There are lots of other not so well-established SPD methods [11] but these are not the main topic of the present thesis. Therefore only the most important ones were mentioned.

of shearing as basic deformation mode is plausible (such as in ECAP or in HPT, see the next subsections). Although in rolling main deformation originates from compression, under certain conditions this method is also capable to produce bulk UFG samples. Additionally nowadays rolling is the only really continuous process, which is capable to produce large amount of product to fulfill the industrial expectations.

Figure 1.1a shows the conventional rolling when the speeds of the rolls v_1 and v_2 are the same. In conventional rolling the equivalent strain can be described as follows [11]:

$$\varepsilon_{\text{eq}} = \frac{2}{\sqrt{3}} \ln\left(\frac{h_0}{h}\right), \tag{1.2}$$

where h_0 and h are the initial and final thicknesses of the sample, respectively (see figure 1.1a).

Figure 1.1a shows the schematic of the differential speed rolling, in which process the circumferential velocity of the upper and the lower rolls are different, and therefore shear deformation can be applied throught the thickness of the sample. In this process with increasing the ratio of the circumferential speeds of the two rolls more homogeneous microstructure has been achieved in 5052 Al alloy [22], as suggested by the more homogeneous distribution of microhardness. It has been found that sample processed by larger speed ratio showed considerably higher hardness than the sample processed by conventional rolling ($v_1 = v_2$) [23]. In pure Cu it was found that the increase of the speed ratio resulted in a decrease of the distance between lamellar boundaries and an increase of the fraction of the high angle grain boundaries [24]. Another study showed that significant improvements can be achieved in the grain refinement by differential speed rolling compared to conventianal rolling in AZ31 magnesium alloy processed at different temperatures [25].

In figure 1.1b the asymmetric rolling is presented, where due to the different radii of the rolls the stability of the evolved microstructure may be different. It was reported that the volume fraction of recrystallized grains in austenitic steels was higher after processing by asymmetric rolling, than by symmetric rolling [26]. It also turned out that there is an optimal roll ratio (in that study it was 1.05), for which the grain refinement is the most effective.

Figure 1.1c shows the flow chart of the accumulative roll-bonding [20], where the sample is rolled up to 50% reduction in width, cut into two pieces and then the pieces stacked to each other after some surface treatment to get the original dimensions and rolled again. During the rolling the stacks 'bonded' together and form one sheet, therefore this process is not simply a deformation process, but a bonding method too. With this technique the reduction of thickness can be avoided and UFG microstructure can be produced by the repetition of the process. It was reported for 1100 Al alloy, that after 6 cycles the whole volume of the sample was UFG and further passes caused no change in the microstructure [20, 21]. The induced strain caused by accumulative roll-bonding may be described as

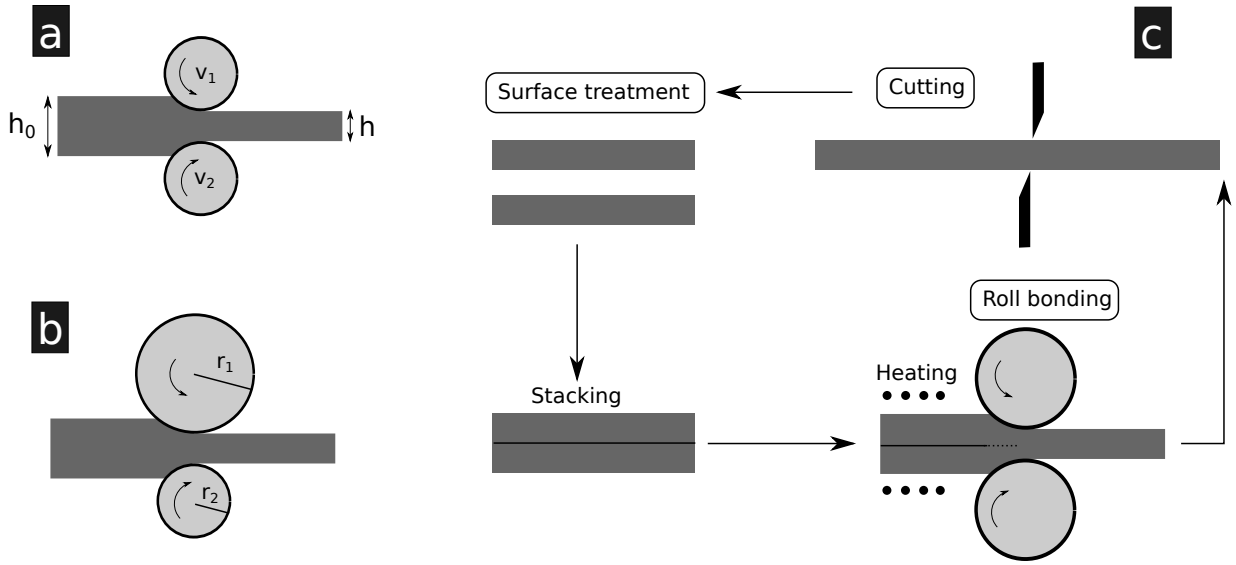

Figure 1.1: Schematic of different types of rolling. (a) differential speed rolling, (b) asymmetric rolling and (c) accumulative roll-bonding.

follows:

$$\varepsilon_{\text{eq}} = \left(\frac{2}{\sqrt{3}} \ln \left(\frac{1}{2} \right) \right) n, \tag{1.3}$$

where n is the number of cycles [11].

1.1.2 Equal-channel Angular Pressing

Among the various SPD methods ECAP is an especially attractive technique. In this procedure a billet, having circular or rectangular cross-section, is pressed through a massive die containing two intersecting channels with an arbitrary channel angle (Φ). The outer arch of the intersection of the channels can be curved with an inclination angle (Ψ). The schematic of the ECAP device is presented in figure 1.2. The main advantages of this procedure are that it can be applied to fairly large samples, the product has roughly the same dimensions as the original billet, therefore the process can be repeated, and the homogeneity of the sample can be assured by the repetition of the procedure continued until sufficiently high strains are reached. The imposed shear strain (γ) during ECAP can be determined from first principles and it depends on the angle of the die (Φ) and the angle associated with the arc of

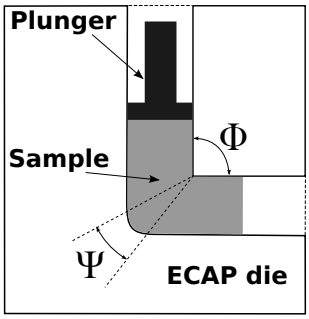

Figure 1.2: Schematic of the ECAP die. In this particular case $\Phi = 90°$ and $\Psi = 20°$

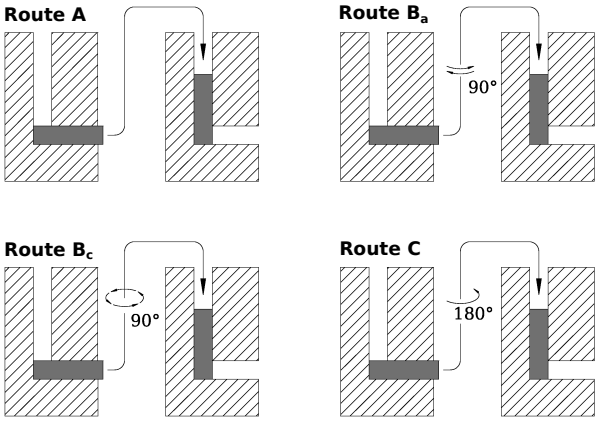

Figure 1.3: Schematic figure of the four basic ECAP routes.

curvature where the two parts of the channel intersect (Ψ), according to the following relation[2] [27]:

$$\gamma = \frac{2}{\tan\chi} + \frac{\Psi}{\sin\chi}, \qquad \text{where} \quad \chi = \frac{\Phi}{2} + \frac{\Psi}{2}. \tag{1.4}$$

The equivalent strain can be expressed from γ as:

$$\varepsilon_{\text{eq}} = \frac{N\gamma}{\sqrt{3}}, \tag{1.5}$$

where N denotes the number of passes. For example a common choice is that $\Phi = 90°$ and $\Psi = 20°$ for which the equivalent strain is $\varepsilon_{\text{eq}} = 1.05$, i.e. practically 1.

If more than one pass is carried out, then it is convenient to introduce the so called ECAP 'routes' [28] in which the billets are rotated along its longitudinal axis. There are four basic ECAP routes which introduce different slip systems during the ECAP [29–31] leading to various microstructures [32–34]. The schematic illustration of the different routes are presented in figure 1.3. In route A there is no

[2]Here the strain is estimated by assuming that any friction effect can be neglected.

rotation between consecutive passes, in route B_a the sample is rotated in alternating direction after each pass by $90°$, while in route B_c the sample is always rotated in the same sense also by $90°$ and in route C the sample is rotated by $180°$. There are different combinations of the mentioned routes, however combining them does not result in significant improvement of the mechanical behavior of the sample compared to the basic routes [31]. Detailed investigations of the dislocation structure, grain sizes and shapes showed that the optimal route to produce equiaxed very fine grain structure is route B_c[3] at least for Al [36] and Ti [37], but according to the knowledge of the author there is no evidence that other materials behave differently.

There are a lot of factors influencing the microstructure developed during ECAP such as the variation of the channel angle or the inclination angle, the ambient temperature, the velocity of pressing and the applied backpressure. These factors are very well described in a review article [27], but are not essential to understand the rest of this work. For this reason we will not deal with them here. However, there is one more important factor to discuss: the internal heating during deformation.

Experiments made on pure Al and Al-Mg alloys [38] showed that the internal heating of the sample is scaling with the ultimate tensile strength and also depends on the velocity of ECAP-processing. For pure Al at a pressing velocity of 18 mm/s the temperature increased from $\sim 11\,°C$ to $\sim 40\,°C$ at the intersection of the two channels. However, thereafter the temperature decreased below $15\,°C$ within $10\,s$. For materials with higher ultimate tensile strength this temperature rise could be more important. The temperature rise decreases with decreasing the pressing velocity according to theoretical heat transfer analysis [39], therefore for a lower passing velocity and for a material with good heat conduction the temperature rise during ECAP may be very low.

1.1.3 High-pressure Torsion

Besides ECAP, HPT is another commonly used SPD technique. Contrary to ECAP, HPT is not capable of producing bulk samples, but by using HPT, extremely large strains can be achieved. In this technique a disk-shape sample is placed between two anvils, a high pressure (typically several GPa) is applied, then one of the two anvils is rotated. Figure 1.4 shows the HPT procedure schematically.

The shear strain (γ_{HPT}) imposed by HPT can be written in the form of [40]

$$\gamma_{HPT} = \frac{2\pi N r}{h}, \tag{1.6}$$

[3] It has to be noted that these investigations were carried out with $90°$ die, nevertheless there are evidences showing that for other angles the optimal route is different [35].

where N is the number of rotations, r is the radius and h is the height of the disk. The equivalent strain can be calculated as

$$\varepsilon_{\text{eq}} = \frac{\gamma_{\text{HPT}}}{\sqrt{3}}. \tag{1.7}$$

This expression, however, does not deal with the reduction of the height of the sample caused by the high pressure during the deformation. Hence, for large strains ($\gamma_{\text{HPT}} \geq 0.8$), where the height reduction is obvious usually another fromula is used [41]:

$$\varepsilon = \ln\left(\frac{2\pi N r h_0}{h_{\text{f}}^2}\right), \tag{1.8}$$

where h_0 and h_{f} denote the initial and the final thickness of the sample, respectively. According to equation (1.8) the imposed equivalent strain depends logarithmically on the radius, which is important for smaller number of revolutions, but has less effect on the microstructure after a larger number of turns.

A fundamental difference between ECAP and HPT is the high applied pressure during HPT-processing. The effect of the pressure on the microstructure has been discussed in details [42, 43]. According to the experimental results obtained on Ni samples the difference in the microstructure of the center and the periphery of the disks decreased with increasing the applied pressure. Namely, it was found that the grain size in the center of the disk tends to be larger than in the peripheral region and this difference was more significant at low applied pressures. The results demonstrated that HPT at low pressure (1 GPa) is not sufficient to form a homogeneous microstructure throughout a Ni disk, since the grains were $2-3$ times larger in the center, than in the peripheral region, however at higher applied pressure (9 GPa) the microstructure was reasonably homogeneous after 5 turns [42]. These results are also consistent with earlier observations using transmission electron microcopy (TEM) [44].

Another study reported that the low applied pressure (1.25 GPa) resulted in the most homogeneous microstructure of pure Al after five turns of HPT [45]. However, this observation was related to the

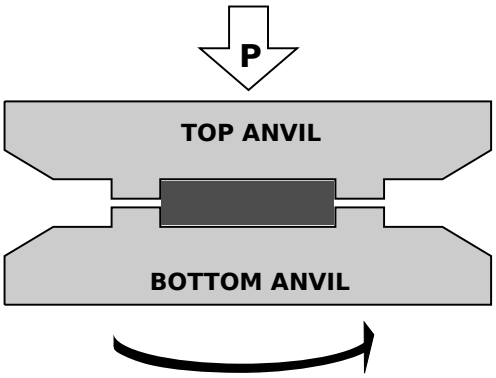

Figure 1.4: Schematic illustration of the cross section of a typical HPT device.

very fast recovery of pure Al, and it is reasonable to assume that there is no general (material independent) rule to the optimal value of applied pressure in order to achieve homogeneous microstructure.

The typical applied pressure during HPT (GPa range) is high enough to induce plastic deformation without any torsional straining, therefore the pressure itself can cause significant microstructural changes. For example in commercial purity Al having a microhardness of 210 MPa the applied pressure of 1 GPa caused a considerable hardening to 320 MPa [46].

Finally, similarly to the case of ECAP the rising of temperature during HPT is worth to be discussed. Finite element simulation results are available supplemented by experimental temperature values recorded in the anvils of the HPT device close to the sample [47, 48]. These results showed that the temperature rise is directly proportional to the strength of the material and the rate of deformation, similarly to the temperature rise during ECAP. For example both simulation and experimental results show that temperature in an iron sample can rise with 25 °C and 5 °C for rotation speeds of 1 rpm and 0.2 rpm, respectively. In Al these values are much lower 5 °C and ∼ 1 °C, respectively. It also turned out, that the pressure has only minor effect on the rise of the temperature during HPT.

1.2 Microstructure Evolution During Severe Plastic Deformation

1.2.1 Dislocation Density and Grain Size

Besides the decrease of the grain size during SPD, other important microstructural parameters also change. Usually the dislocation density increases, while the fraction of high angle grain boundaries (HAGBs) increases at the expense of the low angle grain boundaries (LAGBs) .

At high imposed strain in SPD-porcessing, the dislocation density as well as the grain size reach a saturation level. This saturation level depends on the material and also on the applied SPD method. Figure 1.5 shows the grain and the crystallite sizes for several metals and alloys processed by different methods of SPD as a function of the dislocation density. It is clear that there is no strict correlation between the dislocation density and the grain or crystallite size, however the higher dislocation density is generally associated with smaller grain or crystallite size. The reason of this observation it that, the basic grain-refinement mechanism during SPD is the arrangement of dislocations into grain and subgrain boundaries. Figure 1.5 also shows that the crystallite size is about 2-5 times smaller than the grain size. The former is determined by x-ray line profile analysis, while the latter is obtained by TEM investigations. The difference between the two characteristic lengths is due to the fact that x-ray line

profile analysis measures the coherently scattering domain size corresponding to subgrains or dislocation cells, while in TEM investigations the size of the grains separated by HAGBs are determined.

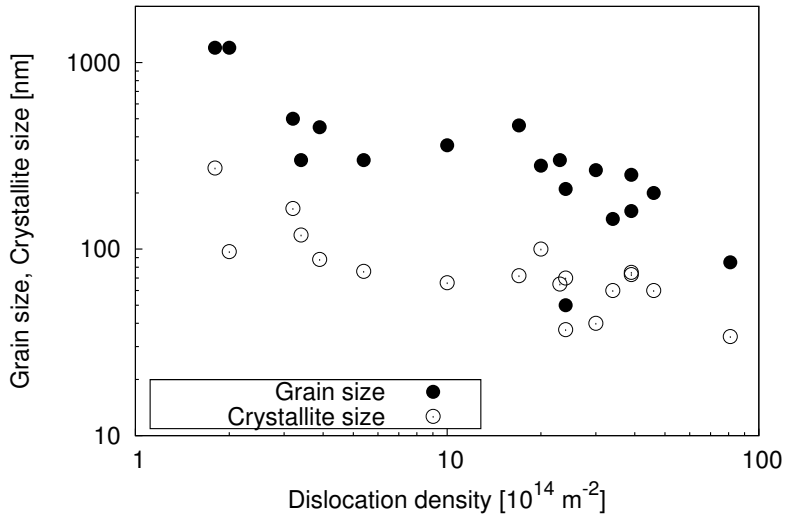

Figure 1.5: Grain and crystallite size as a function of the dislocation density for various metals processed by different methods of SPD. Data taken from reference [49].

The saturation dislocation density during SPD processing is determined as the equilibrium between dynamic recovery and formation of dislocations. The higher saturation dislocation density corresponds to a more difficult dynamic recovery due to 1) the low homologous temperature[4] of SPD, 2) the solid solution alloying, 3) the second phase particles and 4) the high degree of dislocation dissociation due to the low SFE (for details see section 1.3).

The homologous temperature of SPD may be kept low by processing at low temperature, e.g. by cryogenic rolling. The effect of homologous temperature on the saturation dislocation density can be explained by the thermally activated processes of dislocation annihilation. In fcc metals having medium to high SFE due to the low degree of dislocation dissociation the cross-slip of screw dislocations occurs relatively easy. At the same time the climb of edge dislocations is controlled by vacancy diffusion, therefore usually effectively hindered at low homologous temperature. As a consequence the maximum dislocation density is mainly determined by the climb of edge dislocation segments, while due to their easier annihilation the relative fraction of screw dislocations is very low at high strains. It was already mentioned that climb is a diffusion-controlled motion of dislocations, and since the diffusion coefficient depends on the melting point the climb velocity depends primarily on the homologous temperature. The higher the melting point, the lower the homologous temperature at a certain temperature (e.g. RT), therefore the slower the climb of edge dislocations, resulting in larger

[4]Homologous temperature is the actual temperature devided by the melting point (T/T_m).

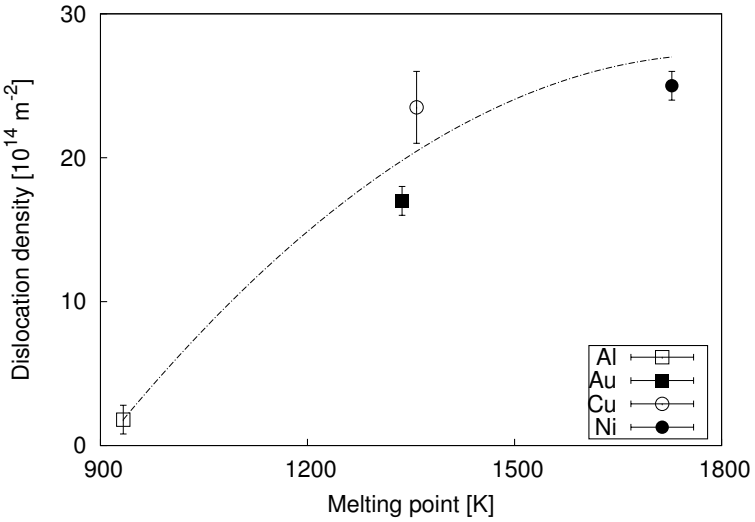

Figure 1.6: Saturation dislocation density vs. the absolute melting point for some pure fcc metals processed by ECAP at RT. Data taken from reference [49].

dislocation density. Figure 1.6 shows the saturation dislocation density against the melting point of different fcc metals processed by ECAP at RT. In general the saturation level was achieved after several passes. There is a quite clear correlation between the maximum dislocation density and the melting point (illustrated by dashed line on figure 1.6).

Although the effect of the SFE on the dislocation motion is reviewed in details in section 1.3, it has to be mentioned here that in low SFE fcc metals (e.g. in Ag) the dissociation of the dislocations can be very significant. The dissociation hinders the cross slip, hence the saturation dislocation density in low SFE metals may be larger than that predicted from the melting point according to figure 1.6.

It should be noted that climb is usually considered as an important annihilation mechanism only at high temperatures, because at lower temperatures (e.g. at RT) the diffusion is very slow. In UFG materials, however, the volume fraction of grain boundaries and the density of dislocations are high, and as diffusion along these defects has the activation energy of about one half of the self diffusion activation energy, therefore in UFG materials diffusion may be about $10^{10} - 10^{20}$ times faster than in coarse grained materials, therefore, climb can control the annihilation of dislocations in SPD-processed metals even at RT.

The different SPD methods usally lead to different saturation levels of the dislocation density. For example the dislcation density introduced by HPT in pure Cu and Ni at RT was $37 - 40 \times 10^{14}\,\mathrm{m}^{-2}$ [50, 51] and $34 \times 10^{14}\,\mathrm{m}^{-2}$ [50], respectively. These values are considerably higher than the maximum value achieved by ECAP in the same metal at the same temperature (see figure 1.6). This is because of the very high applied hydrostatic pressure applied during HPT-processing.

1.2.2 Vacancies Induced by Severe Plastic Deformation

During SPD the climb of edge dislocations may cause either the formation or the annihilation of vacancies depending on the direction of climb. When plastic deformation starts the dislocation density is usually low, therefore the diffusion path of vacancies to dislocations is long which hinders vacancy annihilation at RT. At the same time, the emission of vacancies at climbing dislocations is not limited which results in a considerable increase of the vacancy concentration with increasing strain. As deformation proceeds both the dislocation density and the rate of diffusion increase, hence the formation and annihilation of vacancies equilibrate, yielding a saturation concentration of excess vacancies, which depends on the given conditions of the SPD process. The concentration of excess vacancies may reach or even exceed the equilibrium vacancy concentration at the melting point ($\sim 10^{-4}$).

The concentration of excess vacancies produced during SPD was investigated on pure Cu [52] and Ni [50] processed by ECAP and HPT, respectively. For Cu the vacancy concentration was measured by differential scanning calorimetry (DSC) and electrical resistometry and a very good agreement was found. The measured vacancy concentration was about 1.5×10^{-4} and 4×10^{-4} after 1 and 5 ECAP passes, respectively. It should be mentioned that the saturation vacancy concentration is most probably not reached in these measurements. Another team obtained very similar results on Cu by DSC measurements: the vacancy concentration was 1×10^{-4} and 2.5×10^{-4} after 1 and 3 passes of ECAP [53]. Here a saturation level ($\sim 3.5 \times 10^{-4}$) was reached after 10 passes of ECAP. It has to be noted, that the slight difference between this two studies may be caused by the different ECAP conditions, since in the former case the internal channel angle was $120°$ while in the latter it was the conventional $90°$. The saturation vacancy concentration was in the same range in Cu samples processed by HPT [50].

Other authors estimated considerably higher vacancy concentration in pure Cu after HPT from positron annihilation measurements [54]. It was found that immediately after the first turn the concentration of vacancies was 5×10^{-4} in the center and about 12×10^{-4} at the periphery of the sample. It was also reported that vacancy concentration increased with increasing the number of HPT turns and the highest measured values were 12×10^{-4} and 20×10^{-4} at the center and at the periphery after 25 turns of HPT, respectively.

In pure Ni processed by HPT the vacancy concentration was lower than in Cu [50]. The maximum achievable concentration was $0.8 - 1.2 \times 10^{-4}$ and it depends slightly on the applied hydrostatic pressure during HPT, i.e. for low strains the concentration of vacancies increased with increasing the hydrostatic pressure. For high strains this difference disappeared.

It was also reported that the vacancies form vacancy clusters consisting of 4-5 and 7-9 vacancies in the middle and in the periphery of the HPT disk, respectively, both for Cu and Ni.

1.3 The Effect of Stacking Fault Energy on the Defect Structure in Face Centered Cubic Metals and Alloys

1.3.1 The Effect of Stacking Fault Energy on the Defect Structure in Pure Metals

It is well known that the energy of a dislocation is proprtional to the square of its Burgers vector (the energy of the dislocation core is not considered here). Therefore, in a real structure dislocations with the shortest possible Burgers vector are the most probable, since their energy is the lowest. In an fcc structure the shortest lattice vector points from one corner of the cube cell to the middle of any adjacent face of the cube (see figure 1.7). Therefore, the smallest Burgers vector is the $\frac{1}{2}[011]$ type. Consider a dislocation having a Burgers vector of $\frac{1}{2}[01\bar{1}]$. This dislocation can dissociate into two Shockley partial dislocations:

$$\frac{1}{2}[01\bar{1}] \rightarrow \frac{1}{6}[11\bar{2}] + \frac{1}{6}[\bar{1}2\bar{1}]. \tag{1.9}$$

On the right side of (1.9) the vectors are not lattice vectors, therefore the dislocations with those Burgers vectors are not full dislocations. This process is energetically favourable, because the energy of the two partials is less than the energy of the full dislocation, therefore in fcc systems dislocations are always dissociated. The degree of the dissociation depends on the properties of the material.

Between the two partial dislocations there is a stacking fault ribbon, in fcc case, on the $[111]$ lattice plane. The equilibrium width of this ribbon, i.e. the splitting distance between the partial dislocations may be determined by equating the attracting force originating from the formation of the stacking

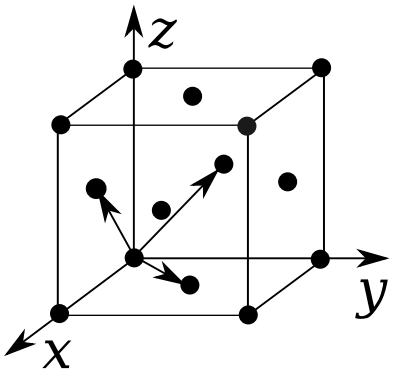

Figure 1.7: Fcc Bravais cell with the shortest possible lattice vectors.

fault between the partials and the repulsive force resulting from the interaction of the stress fields of the partials [55]:

$$d_{\mathrm{p}} = A\frac{Gb^2}{\gamma}, \tag{1.10}$$

where A is a constant, having a value of 0.019 for screw and 0.048 for edge dislocations, G is the shear modulus, b is the magnitude of the Burgers vector of the full lattice dislocation and γ is the stacking fault energy. It should be noted that the local stress acting on the actual lattice plane and the extremely small grain size (< 20 nm) affect the width of the dislocation ribbon (for details see [49]). The values of the equilibrium splitting distances for edge and screw dislocations, when expressed in terms of the Burgers vector units (d_{p}/b), were calculated using equation (1.10) from the values of G, b and γ. The results are listed for the most common fcc metals in table 1.1.

Table 1.1: The lattice parameter a, the stacking fault energy γ, the twin fault energy γ_{t}, the shear modulus G, the equilibrium splitting distance of partials in dissociated edge $d_{\mathrm{p}}^{\mathrm{e}}$ and screw $d_{\mathrm{p}}^{\mathrm{s}}$ dislocations and the d_{p}/b ratio for different fcc metals. (In the following for Ag the average splitting distances will be used; 2.6 nm for screw and 6.5 nm for edge dislocations.)

Metal	a [Å]	γ [mJ/m^2]	γ_{t} [mJ/m^2]	G [GPa]	$d_{\mathrm{p}}^{\mathrm{s}}$ [nm]	$d_{\mathrm{p}}^{\mathrm{s}}/b$	$d_{\mathrm{p}}^{\mathrm{e}}$ [nm]	$d_{\mathrm{p}}^{\mathrm{e}}/b$
Ag	4.09	22 [56]		30 [57]	2.2	7.5	5.5	18.9
		16 [58]	8 [58]		3.0	10.3	7.5	26.0
Au	4.08	45 [56]		27 [57]	0.9	3.3	2.4	8.3
		32 [58]	15 [58]		1.3	4.5	3.4	11.5
Cu	3.61	78 [56]		47 [57]	0.7	2.9	1.9	7.4
		45 [58]	24 [58]		1.3	5.1	3.3	12.8
Ni	3.52	125 [58]	43 [58]	82 [57]	0.8	3.1	2.0	7.8
Al	4.05	166 [58]	75 [58]	26 [57]	0.2	0.9	0.6	2.2

The effect of dissociated dislocations on the mechanism of deformation was studied in details by Müllner and Solenthaler [59] for metals having low SFE. According to their model at relatively low strains the deformation is controlled mainly by the planar glide of dissociated dislocations and the dislocation density increases rapidly. As the deformation proceeds, dislocation pile-ups form at glide obstacled such as Lomer–Cottrell locks or grain boundaries. Obstacles hinder very efficiently the motion of dislocations, since to move on, the dislocation have to cross-slip or climb to the adjacent slip plane which is retarded by the high degree of dislocation dissociation. To change slip plane the dislocation ribbon has to contract and this is an energetically unfavourable process. At these

obstacles if the local stress exceeds the critical stress required for twin nucleation, the deformation continues by twinning. Therefore, with increasing strain both the dislocation density and the twin boundary frequency increase. Since twin boundaries obstruct the glide of dislocations, the dislocation activity decreases with increasing twin fault frequency. Therefore, there is a well-defined saturation in the dislocation density, and further straining causes a decrease in the dislocation density, while twin fault frequency further increases. The reduction of the dislocation density may be explained in terms of the twinning mechanism. In the literature there are several twinning mechanisms such as pole mechanism, dissociation of lattice dislocations into Schockley and Frank partials, emission of twinning partials from grain boundaries or nucleation of three-layer twins [49]. All of these mechanisms are based on the dissociation of dislocations into twinning partials and their slip on $\{111\}$ planes. When a twinning partial reaches the grain boundary it annihilates there, therefore twinning contributes to the annihilation of dislocations, resulting in a decrease of the overall dislocation density.

Since glide obstacles retard the motion of dislocations more efficiently in metals having low SFE, deformation twinning is more important in these materials, and the twin boundary probability is usually higher in the deformed state.

In some alloys (Cu-Al, Cu-Zn) the increase of the alloying element concentration results in the decrease of the SFE, therefore the influence of the SFE on the defect structure can be studied by varying the alloying concentration. It should be noted, that since the SFE is modified due to alloying, the effects attributed to the alloying such as solid solution hardening can not be easily separated from the effect of the lower SFE.

For Cu-Zn alloys it was found that the strength and the ultimate elongation of the alloy increased with decreasing SFE [60], however this tendency breaks for the lowest values of SFE (below $7\,\mathrm{mJ/m^2}$). Therefore, Cu-Zn alloy has an optimum SFE yielding the best ductility and it is because if the SFE is too low, extremely small grains form during SPD, leading to a poor ductility [61].

For Cu-Al alloys several studies established that decreasing the SFE results in the increase of strength even in simple compression tests [62] or after cold rolling [63]. Another study reported that the SFE influences significantly the grain refinement in Cu-Al alloys, and by enhancing the Al content the SFE can be reduced, therefore the grain size can be refined to less than 100 nm by ECAP at room temperature [64]. According to this study this remarkable effect of SFE on grain refinement was attributed to the transition of the dominant deformation mechanism from subgrain division to deformation twinning and shear banding. The critical value for this transition was found at $\gamma = 28\,\mathrm{mJ/m^2}$, corresponding to an Al content of $5\,\mathrm{at}\%$ in Cu. It was also shown that the low SFE causes high dislocation density and twin boundary frequency after deformation, and the latter hinders the recovery, thereby contributing to the improvement of ductility [62].

A simulation study [65] revealed that in metals with high SFE grain boundaries are only able to emit twinning partial dislocations if the grain size is smaller than 100 nm. However, this critical grain size increases with decreasing SFE, therefore in low SFE metals, such as in Ag, grain boundaries are able to emit partial dislocations even when the grain size exceeds several hundreds of nanometers.

These few examples showed that SFE has a complex effect on the deformation mechanisms, on the microstructure evolved during SPD and even on the thermal stability of the UFG microstructure.

1.3.2 The Effect of Low Stacking Fault Energy on the Defect Structure in Ultrafine-grained Alloys

In some binary systems alloying is accompanied by the decrease of SFE, therefore the influence of SFE on the deformation mechanisms and the microstructure evolved during SPD can be studied by varying the solute atom concentration in these alloys (e.g. Cu-Zn, Cu-Al), as was mentioned above. Figure 1.8 shows the dislocation density, the average crystallite size and the twin boundary frequency against the SFE for different Cu-Zn alloys after 5 revolutions of HPT (values recorded at the half-radius) [66]. The dislocation density increases with increasing the Zn content, i.e. decreasing the SFE. However, this is a consequence partly of the pinning effect of alloying elements on dislocations and partly of the decrease of SFE. As was discussed above, the decrease of the SFE leads to a higher dissociation of dislocations and therefore a more retarded annihilation of dislocations during SPD. The increase of the twin boundary frequency and the decrease of the average crystallite size are most probably a consequence of the low SFE and the high dislocation density (for details see subsection 1.3.3).

1.3.3 Grain Refinement Mechanisms in Low SFE Alloys

During SPD in metallic materials with medium or high SFE dislocations form low angle grain boundaries by their arrangement into dislocation walls. As deformation proceeds more dislocations join to the walls and the angle of misorientation increases, which leads to grain refinement.

In contrast, low SFE alloys deform mainly by the motion of partial dislocations and twinning. It was observed in a Cu-30 wt.% Zn alloy [67], having extremely low SFE (about 10 mJ/m^2), that during HPT, first stacking faults and twin boundaries form mainly due to partial dislocation glide. Hence, the initially equiaxed grains were devided into elongated regions. Then dislocations accumulated at stacking faults and twin boundaries, changing the originally flat boundaries into curved, incoherent high

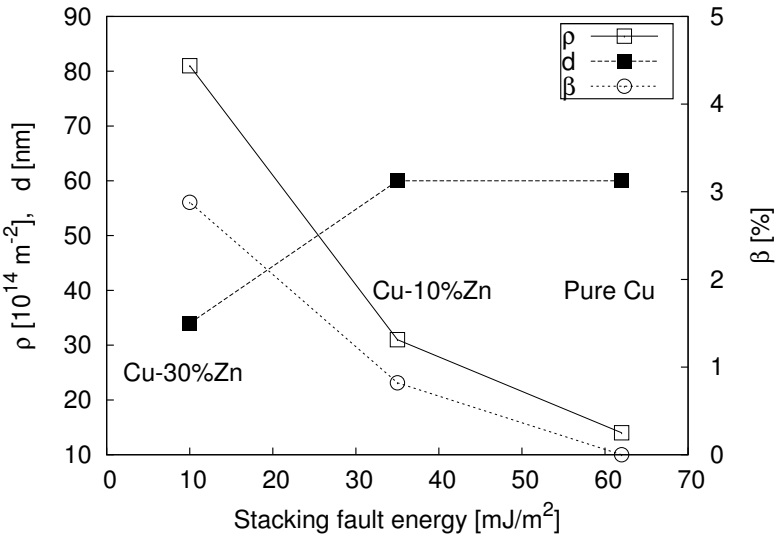

Figure 1.8: Dislocation density (ρ), average crystallite size (d) and the twin boundary frequency (β) obtained on Cu-Zn alloys after HPT at the half-radius of the disk.

angle grain boundaries. After that secondary stacking faults and twin boundaries were emitted from the new grain boundaries[5]. This further refinement of the grains led to an equiaxed grain structure with an exceptionally small grain size (about 10 nm).

Similar results were presented for Cu-Al alloys [70] having low SFE (Cu-5 at.% Al with 28 mJ/m^2, Cu-8 at.% Al with 17 mJ/m^2 and Cu-16 at.% Al with 7 mJ/m^2). In Cu-5 at.% Al the main grain refinement mechanism was the dislocation activity, although the contribution of twinning was also detectable. The increasing Al content (decreasing SFE) yields to a transition of the main grain refinement mechanism from dislocation subdivision to twin fragmentation. These authors concluded, that due to the increase of stacking fault and twin boundary probability, the strength and the ductility of the Cu-Al alloy increased simultaneously.

1.4 Mechanical Properites of SPD-processed Metals

1.4.1 Yield Strength of SPD-processed Metals

For UFG materials the dislocation density and the yield strength (σ_y) show similar evolution as a function of the strain applied in SPD-processing. Both quantities saturate at approximately the same

[5]It has been shown by molecular-dynamic simulations, that partial dislocations are emitted from the grain boundaries and twinning occurs due to this process [68, 69].

strain and therefore it seems reasonable to study the relation between these quantities. This relation is generally characterized by the Taylor equation:

$$\sigma_{\mathrm{y}} = \sigma_0 + \alpha M G b \varrho^{1/2}, \tag{1.11}$$

where σ_0 is the friction stress, α is a constant depending on the arrangement of the dislocations, M is the Taylor factor, G is the shear modulus, b is the magnitude of the Burgers vector and ϱ is the dislocation density. Since for pure fcc metals the αM product is approximately 1, the validity of equation (1.11) can be verified by plotting $\sigma_{\mathrm{y}} - \sigma_0$ against $Gb\varrho^{1/2}$. This plot is shown in Figure 1.9 for pure fcc metals. The good correlation in this figure demonstrates that the yield strength of SPD processed metals is determined mainly by the interaction between dislocations.

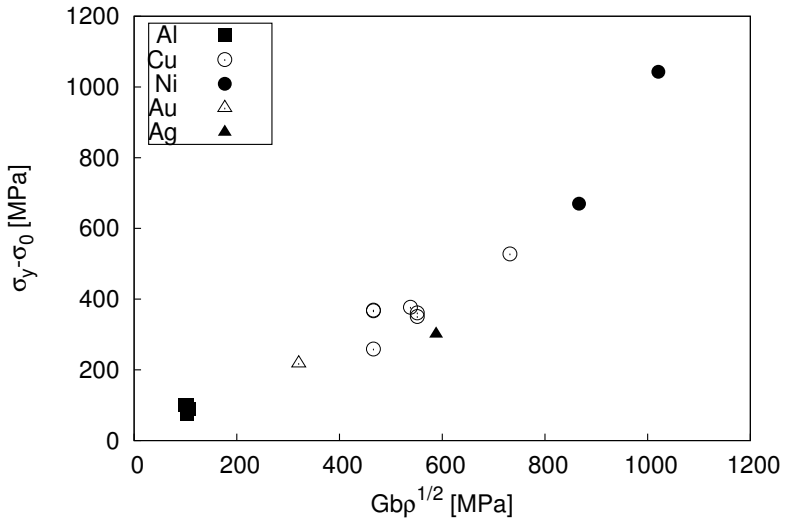

Figure 1.9: The yield strength reduced by σ_0 vs. the $Gb\varrho^{1/2}$ product for different pure fcc metals. Data are taken from [49].

The observation that equation (1.11) describes very well the change of the yield strength in severely deformed metals can be explained by the fact that the main grain refinement process in SPD processed metals is the arrangement of dislocations into subgrain/grain boundaries. Consequently, a large fraction of boundaries consists of dislocations and the effect of subgrain/grain boundaries on dislocation motion can be regarded as the interaction between dislocations. It is noted that the effect of HAGBs on the strength can also be taken into account by the Hall–Petch formula (1.1).

1.4.2 Ductility of UFG and Nanocrystalline Metals

The ductility of a material is usually characterized by the maximum true strain before inhomogeneous deformation (e.g. necking). This quantity is very important from the application point of view. In UFG materials the dislocation density is high and the grain size is small, therefore the flow stress at RT is high already at the beginning of tension/compression and additionally it tends to saturate at lower strains than for coarse-grained materials. As a consequence, ductility decreases with decreasing the grain size.

In figure 1.10 the uniform elongation can be seen for commercial 1100 Al and for interstitial-free steel as a function of the grain size. This figure reveals a loss of ductility in both materials when the grain size decreases below 1 μm. The inset shows another measurement carried out on stainless steel processed by ECAP. The loss of ductility is obvious as the applied plastic strain increases.

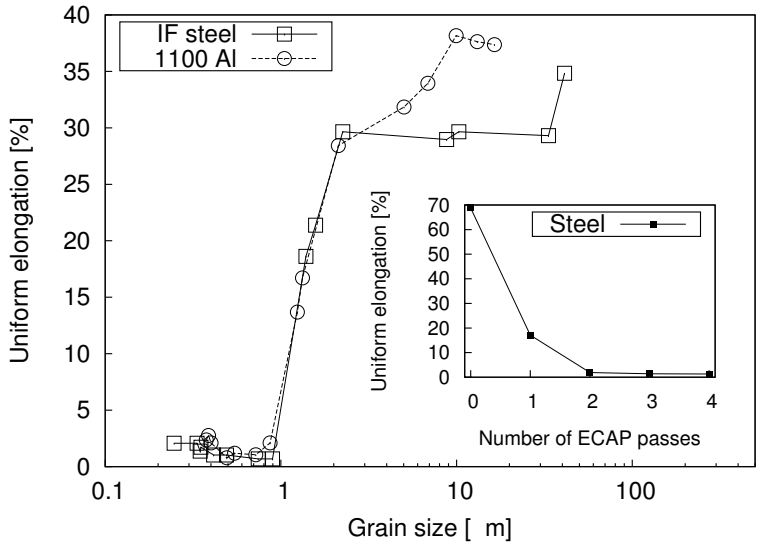

Figure 1.10: The uniform elongation against the grain size for interstitial-free (IF) steel and 1100 Al alloy [71]. The inset shows the uniform elongation of stainless steel versus the number of ECAP passes [72].

Achieving a reasonable ductility in bulk high-strength UFG materials is still a challenge. The different approaches proposed to improve ductility are: (i) bimodal grain size distribution [73]; (ii) controlled precipitation through ageing of SPD-processed alloys [74,75]; (iii) introduction of nanoscale twins [76–78]; (iv) through transformation/twinning-induced plasticity [79]; and (v) control of the grain boundary character [61]. It may be noted that except for the bimodal grain size approach, the applicability of the other methodologies is strongly dependent on the structure and composition of the alloy. Even the bimodal grain size approach is indirectly dependent on the composition if

SPD-processing followed by controlled recrystallization annealing is used to produce the bimodal microstructure, as suggested by Wang et al. in their work on Cu [73]. However, such an approach when applied on Ni did not result in the simultaneous improvement in strength and ductility, though a bimodal grain size distribution was obtained [80]. This is attributed to the higher SFE of Ni (see table 1.1), which may cause a higher rate of recovery than in Cu during annealing [80]. Recent research showed that nano-sized deformation twins (obtained by SPD-processing of low-SFE alloys) increase the strength significantly but the ductility is still limited [76,77,81]. In most cases, a short-time or low-temperature annealing of SPD-processed medium/low-SFE alloys with nanosized deformation twins improves the ductility but at the cost of strength [77,82]. For example, Cu processed by dynamic plastic deformation has a yield strength of ~ 600 MPa with low uniform elongation ($\sim 1\%$) and annealing at 120 °C for 1 h resulted in the decrease in the yield strength to ~ 300 MPa, while recovering the uniform elongation to $\sim 8\%$ [82]. The loss in strength is due to the significant decrease in defect density during annealing. It is clear from the above results that a short-term annealing/ageing treatment is needed to recover the ductility following SPD-processing. The question is whether it is possible to retain the strength of UFG alloys while the ductility is being recovered. For retaining strength, the recovery, the grain growth and the precipitate coarsening have to be controlled.

1.5 Stability of SPD-processed Metals

UFG and nanostructured metals have non-equilibrium microstructures with high stored energy due to the large amount of lattice defects. This stored energy acts as driving force for annihilation of lattice defects, although SPD-processed commercial purity metals are usually stable at the processing temperature. This is due to the pinning effect of the impurity atoms on the lattice defects. On the other hand in high purity nanometals annihilation of lattice defects (recovery) and grain growth (recrystallization) may also occur at the processing temperature during long term storing.

As an example, in 99.98% purity Cu during four years of storage at RT the area under the exothermic DSC peak decreased with a factor of 2-3 [51]. This refers to a reduction of the energy stored in the lattice due to annihilation of lattice defects. As neither the dislocation desnity nor the crystallite size of the sample (both determined by x-ray line profile analysis) did not vary during the four year storage or their change was marginal, the difference should be caused by vacancy-type deffects, which can not be seen by XLPA, but their presence was shown in earlier studies [52, 83, 84]. The reduction of vacancy type defects did not yield considerable decrease of the hardness of the ECAP processed samples during four years of storage. It should be noted, that recovery and recrystallization may occur in these Cu samples during longer storage at RT similarly as reported in a previous study [85].

The same material (99.98% purity Cu) processed by 25 revolutions of HPT exhibited even stronger recovery during RT storing for four years [51]. In this case the reduction of the dislocation density from $37 \times 10^{14}\,\mathrm{m}^{-2}$ to $13 \times 10^{14}\,\mathrm{m}^{-2}$ was observed during four years of storage at RT, as well as the increase of the crystallite size from 75 nm to 122 nm. The reduction of the lattice defect densities and the grain growth were accompanied by considerable softening, when the hardness decreased from 1.69 GPa to 1.07 GPa during four years of storage at RT.

This significant difference of the thermal stability of Cu processed by ECAP and HPT may be attributed to the very high hydrostatic pressure during processing by HPT, which can effectively retard the annihilation of lattice defects during HPT. After releasing the pressure, the diffusion of vacancies became quicker, resulting in the annihilation of edge dislocations by climb. As the achievable saturation dislocation density is usually lower after ECAP, the driving force for recovery is also lower in the samples processed by ECAP, which yields a better thermal stability.

During the DSC investigation of the high temperature thermal stability of fcc metals with medium or high SFE a single exothermic peak evolved at the temperature of about $0.3 - 0.4 \times T_{\mathrm{m}}$, where T_{m} is the absolute melting point [51, 86]. In the temperature range corresponding to the exothermic peak, both recovery (annihilation of vacancies and dislocations) and recrystallization occurred [87, 88]. For UFG fcc metals the activation energy of recovery/recrystallization is about $0.5 \pm 0.1 \times Q_{\mathrm{self}}$, where Q_{self} is the activation energy of self-diffusion, irrespective of the SPD processing method [86, 89–96]. Earlier studies showed that the activation energy of diffusion along grain boundaries and dislocations is also about one-half of the activation energy for self-diffusion [97–99]. It suggests that the vacancy diffusion during recovery takes place along dislocation cores and grain boundaries.

Experiments on 99.998 and 99.99% purity Ni samples processed by HPT at RT revealed the occurrence of two exothermic peaks in the DSC thermograms [50, 83]. The smaller first peak appearing at a lower temperature corresponded to the disappearance of excess mono-vacancies while the larger second peak was associated with the annihilation of vacancy clusters and dislocations as well as recrystallization. The first peak was not observed for 99.99% Cu HPT-processed under the same conditions since probably all vacancies were clustered [50]. In the case of Ni, the high values of SFE and melting point retarded the clustering of vacancies at RT because the formation of clusters on $\{111\}$ planes is accompanied by the development of stacking faults and the higher melting point is associated with a larger activation energy for diffusion, thereby giving a slower vacancy migration at RT.

It is apparent from the DSC results on HPT-processed Ni [50] that the value of SFE significantly influences the thermal stability of UFG fcc metals. Additional evidence for this effect is the so-called self-annealing phenomenon in low or medium SFE Au and Cu samples when a UFG microstructure tends to recover/recrystallize during storage at RT [100–102].

Chapter 2

Measurement Techniques

In this chapter the measurement techniques used in this thesis will be discussed, especially x-ray line profile analysis since this was the main examination method during the whole investigation. Besides x-ray line profile analysis other complementary techniques such as different kinds of microscopies should be used to validate the assumptions in the evaluating method of line profiles. Other techniques (micro and nanohardness, uniaxial compression tests) were used to characterize the mechanical properties of the lattice defects, and additionally the high temperature thermal stability of the samples were analyzed by differential scanning calorimetry and positron annihilation spectroscopy.

For the shake of clarity it should be mentioned here, that in this thesis pure silver samples processed ECAP and HPT and a copper-silver alloy processed by rolling will be investigated.

2.1 X-ray Line Profile Analysis

When x-ray scatters on a crystalline material, high intensity peaks evolve in specific directions (θ) with respect to the incoming beam. These specific directions are determined by the structure of the crystalline material, its lattice parameter (a) and the wavelength of the radiation (λ) according to the following relation, where n is an integer

$$2d_{hkl}\sin\theta = n\lambda. \tag{2.1}$$

Equation (2.1) is called Bragg-equation after the inventors W.H. Bragg and W.L. Bragg. In equation (2.1) d_{hkl} is determined as the distance between the adjacent lattice planes with hkl Miller-indices [103]. For cubic lattices

$$d_{hkl} = \frac{a}{\sqrt{h^2+k^2+l^2}}. \tag{2.2}$$

X-ray diffraction is applicable on a solid crystalline material for different purposes, such as phase analysis, lattice parameter measurements (see section 2.5) or even defect structure analysis. In this section the defect structure analysis will be presented in details.

If the scattering crystal is perfect (free of defects) and its spatial dimensions are infinite, then the Bragg-peaks would have Dirac delta shape. Nevertheless any imperfection in the crystal results in the broadening of the Bragg-peaks. This phenomenon provides the opportunity for the x-ray line

profile analysis, in which the microstructure is characterized through the detailed investigation of the broadening of the Bragg-peaks. There are numerous broadening effects such as finite crystallite size, lattice distortions, planar faults etc. We should also mention the instrumental broadening effect, which comes for example from the divergence or the width of the beam, which are always present in a real measurement.

According to the kinematical theory of x-ray scattering the measured intensity profile is the convolution of the size, the strain, the planar fault and the instrumental profiles. Therefore the Fourier-coefficient of the measured profile $A^{\mathrm{M}}(L)$ is the product of the Fourier-coefficients of the different broadening effects:

$$A^{\mathrm{M}}(L) = A^{\mathrm{S}}(L) \cdot A^{\mathrm{D}}(L) \cdot A^{\mathrm{P}}(L) \cdot A^{\mathrm{I}}(L), \tag{2.3}$$

where A^{S}, A^{D}, A^{P} and A^{I} are the Fourier-coefficients of the size, strain (distortion), planar fault and instrumental broadening, respectively and L is the Fourier length, defined as

$$L = \frac{n\lambda}{2(\sin\theta_2 - \sin\theta_1)}, \tag{2.4}$$

n is an integer, λ is the wavelength of x-rays while θ_1 and θ_2 are the endpoints of the angular range of the measured diffraction profile.

2.1.1 Size Broadening

There are different theoretical functions describing the distribution of the size of the crystallites[1], such as the Gaussian or normal, lognormal, gamma and York's distribution[2]. In the case of SPD materials the most commonly used function is the lognormal distribution, which has two parameters, m corresponding to the median of the distribution and σ is the variance

$$f(x) = \frac{1}{\sqrt{2\pi}\sigma}\frac{1}{x}\exp\left[-\frac{\left(\log\left(\frac{x}{m}\right)\right)^2}{2\sigma^2}\right]. \tag{2.5}$$

It was shown that the lognormal, the gamma and the York's distributions describe very well the experimental crystallite size distributions, so that on experimental basis it is not possible to distinguish between these distributions [104], hence we choose the lognormal distribution in this work.

[1] In this context those regions which scatter x-rays coherently are referred to as crystallites.

[2] $f(x) = \frac{a}{b\Gamma(a)}\left(\frac{ax}{b}\right)^c \exp\left(-\frac{ax}{b}\right)$, where $c = a$ for the York's and $c = a - 1$ for the gamma distribution and Γ is the gamma function.

If the crystallites have spherical shape and lognormal size distribution, the intensity profile can be described as [105, 106]:

$$I^{\mathrm{S}}(g) = \int_0^\infty \mu \frac{\sin^2(\mu\pi g)}{(\mu\pi)^2} \operatorname{erfc}\left(\frac{\ln\frac{\mu}{m}}{\sqrt{2}\sigma}\right) \mathrm{d}\mu, \tag{2.6}$$

where g is the magnitude of the diffraction vector, m and σ are the parameters of the lognormal distribution and

$$\operatorname{erfc}(\xi) = \frac{2}{\sqrt{\pi}} \int_\xi^\infty \exp(-y^2)\mathrm{d}y \tag{2.7}$$

is the complementary error function.

The Fourier-coefficient of the size broadening can also be expressed as follows:

$$\begin{aligned} A^{\mathrm{S}}(L) &= \frac{m^3}{3} \exp\left(\frac{9}{4}(\sqrt{2}\sigma)^2\right) \operatorname{erfc}\left(\xi - \frac{3}{2}\sqrt{2}\sigma\right) \\ &- \frac{m^2}{2} \exp\left((\sqrt{2}\sigma)^2\right) |L| \operatorname{erfc}\left(\xi - \sqrt{2}\sigma\right) + \frac{|L|}{6} \operatorname{erfc}(\xi), \end{aligned} \tag{2.8}$$

where

$$\xi = \frac{\ln\frac{|L|}{m}}{\sqrt{2}\sigma}. \tag{2.9}$$

Usually the mean crystallite size is taken as the area-weighted mean crystallite size, which can be calculated from the parameters of the crystallite size distribution as follows:

$$\langle x \rangle_{\mathrm{a}} = m \exp(2.5\,\sigma^2). \tag{2.10}$$

It is important to note that the peak shape described in equation (2.6) does not depend of the hkl indices, therefore size broadening is order independent.

2.1.2 Strain Broadening

If there are lattice distortions in the sample, the shape of the peak can not be given in a simple form as the size profile in the previous section (equation (2.6)). Instead, the Fourier-transform of the strain-broadened peak can be given simply as [107]:

$$A^{\mathrm{D}}(L) = \exp(-2\pi^2 g^2 L^2 \langle \varepsilon_L^2 \rangle), \tag{2.11}$$

where $\langle \varepsilon_L^2 \rangle$ is the mean square strain caused by the displacement of the atoms relative to their ideal position. If the distortion is caused by randomly distributed dislocations, the mean-square strain has the following form [108, 109]:

$$\langle \varepsilon_L^2 \rangle = \left(\frac{b}{2\pi}\right)^2 \pi \varrho C f\left(\frac{L}{R_e^*}\right), \tag{2.12}$$

where b is the magnitude of the Burgers vector of dislocations, ϱ is the dislocation density, C is the contrast factor of dislocations, f is the so-called Wilkens function [108] and R_e^* is the effective outer cut off radius of dislocations. Substituting equation (2.12) into (2.11) one can obtain the strain Fourier-transform:

$$A^{\mathrm{D}}(L) = \exp\left[-\frac{\pi b^2}{2}(g^2C)\varrho L^2 f\left(\frac{L}{R_e^*}\right)\right]. \tag{2.13}$$

Dislocations have anisotropic strain field, which means that the line broadening depends on the relative orientation of the diffraction, the line, the Burgers vector of the dislocation and the normal vector of the slip plane. The contrast factor C describes the 'visibility' of dislocations in a particular hkl reflection in the diffraction experiments. Although the contrast factors can be determined for each slip systems and hkl indices, in randomly oriented polycrystalline materials only an average contrast factor can be observed. It has been shown [110], that if the specimen is untextured or every possible slip systems are equally populated by dislocations, the average contrast factor for cubic materials can be expressed as

$$\overline{C} = C_{h00}(1 - qH^2), \tag{2.14}$$

where

$$H^2 = \frac{h^2k^2 + h^2l^2 + k^2l^2}{(h^2 + k^2 + l^2)^2} \tag{2.15}$$

and q describes the edge/screw character of dislocations. Since in this thesis only cubic materials are discussed, the formulas of the average contrast factors for other structures (e.g. hexagonal or orthorhombic) are not presented here, but may be found in reference [110]. The value of C_{h00} can be calculated on the basis of the dislocation crystallography and the elastic constants of the material.

The individual contrast factors as well as their average ($\overline{C}$) can be calculated numerically by the program ANIZC [111] using the elastic constants of the material and the line, Burgers and normal vectors describing the orientation of the dislocations with respect to the diffraction vector.

It should be noted that the order-dependence of the strain Fourier-transform is given by g^2C, and therefore line broadening caused by micro strains is order dependent in contrast to the size broadening. This difference provides the opportunity for the separation of the two effects in the Williamson–Hall analysis [112].

2.1.3 Planar Faults

If a material contains planar faults such as stacking faults and twin faults, then their line broadening effect has to be taken into account. The planar faults cause Lorentzian shape of every individual

subreflection[3], except for the subprofiles for which the sum of the hkl indices is a multiple of three. These subreflections are broadened and shifted due to planar faults. The sum of these subprofiles gives the total diffraction lines for polycrystalline materials. Due to the different shifts and breadth of subreflections, extrinsic and intrinsic stacking faults cause asymmetric profile shape. However in the case of twin faults the diffraction peaks are symmetric for fcc crystals due to the lack of shift of subreflections [113].

In the most general case the intensity profile caused by planar faults can be expressed in the following form [114]:

$$I^{\mathrm{P}}(g) = p_0^{hkl}\delta(g) + \sum_{n=1}^{3} \frac{p_n^{hkl}}{1 + \left(\frac{g - g_n^{hkl}}{w_n^{hkl}}\right)^2}, \tag{2.16}$$

where the first term is a Dirac delta and the three others are shifted and broadened Lorentzian functions[4]. The width (w_n^{hkl}) and the shift (g_n^{hkl}) of the Lorentzian curves as well as the p_n^{hkl} values can be evaluated numerically (using the DIFFaX software package [115]) for the different types of stacking faults.

2.1.4 Measurement, Evaluation and Instrumental Broadening

The measurements of x-ray diffraction lines were performed using a special high-resolution diffractometer (Nonius FR591) with CuKα_1 radiation ($\lambda = 0.154059\,\mathrm{nm}$ [116]). The schematic of the measurement layout as well as a photo of the device is shown in figure 2.1. The cross-section of the beam is a rectangle with a size of $130 \times 1200\,\mu\mathrm{m}^2$. The sample-detector distance may be adjusted in a wide range, but usually 200 or 492 mm was used. The diffracted intensity is detected by imaging plate detectors, two plates for the 200 mm and four plates for the 492 mm sample-detector distance measurements. One measurement took one or two days depending on the sample-detector distance. It should be noted, that the larger sample-detector distance results in a better 2θ resolution and smaller covered solid angle. Although, in this case a larger area of the imaging plates can be used, due to the air scattering the intensity is reduced, therefore the measurement time is longer. In SPD processed metals the high defect density results in very broadened peaks, hence lower angular resolution is usu-

[3]Here reflections differing only in the direction of the diffraction vector, but not in its absolute value (e.g. reflection (110) and (101)) are termed as subreflections.

[4]Equation (2.16) contains four terms related to the four different combinations of the hkl indices; $(h+k+l)$, $(h+l-l)$, $(h-k+l)$ and $(h-k-l)$. In the case of the combinations for which the sum of indices is a multiple of three, the subprofile is a Dirac delta function. However, there are reflections (e.g. 953) for which the sum for any combination is not a multiple of three, i.e. the whole peak profile is the sum of four Lorentzian functions.

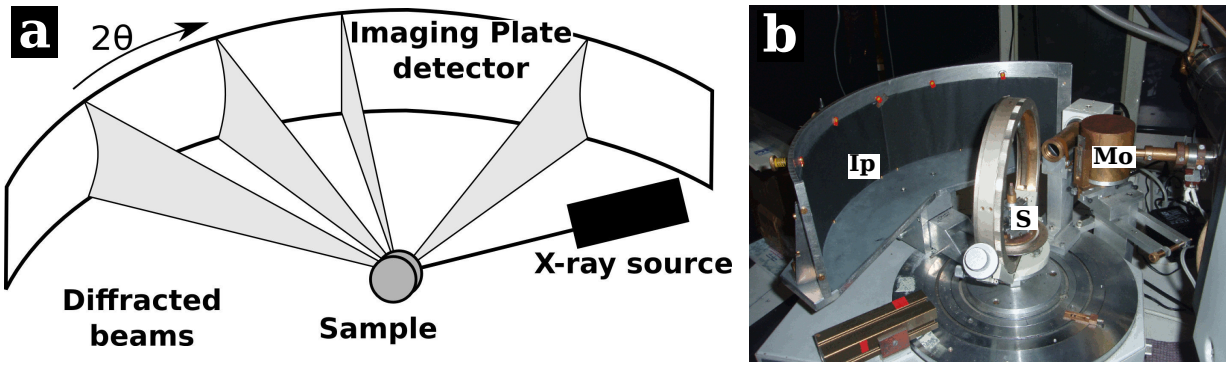

Figure 2.1: Schematic of the x-ray diffraction experiment (a) and photo of the device (b). Mo - monochromator, S - sample, Ip - imaging plate detectors.

ally satisfactory.

Figure 2.2a shows a typical intensity distribution on the imaging plates. After the measurements the imaging plates were read out by a special scanner (Fujitsu BAS Reader) having a maximal spatial resolution of $50\,\mu$m and the intensity depth of 16 bit. These image files were than processed on a computer. The area of interest was cut out for further evaluation. This area is usually incorporates the whole angular range, but covers only the middle of the imaging plate with height of 500–800 pixels (as illustrated in figure 2.2a). The reason of this processing step is the larger instrumentals broadening in the bottom and top parts of the imaging plates due to the vertical elongated shape of the incident beam. Even smaller area in the imaging plates were used when intensity spots were present, generally after recrystallization of a sample, as the width of these intensity spots is too close to the instrumental broadening, therefore they can not be evaluated. Figure 2.2b shows a Debye–Scherrer ring of a reflection with considerable number of sharp spots (area 2) and a homogeneous part which can be used for evaluation (marked as 1). After the selection of the region of interest the intensity as a function of 2θ was obtained by integrating this distribution along the Debye–Scherrer ring for each value of 2θ. A typical diffraction pattern can be seen in figure 2.3.

In the present experiment the relatively large sample-detector distance, the narrow beam and the significantly broadened peaks (for metals deformed by SPD the lines are usually very broad) enables the neglect of the instrumental broadening. Therefore, instrumental correction was not used.

The line profiles were evaluated using the eCMWP (extended convolutional multiple whole profile) fitting procedure [117]. In this method, the diffraction pattern is fitted by the sum of a background spline and theoretical peak profiles. The profile functions are calculated as the convolution of the theoretical size, strain and planar fault peak profiles (as mentioned earlier in this section). These

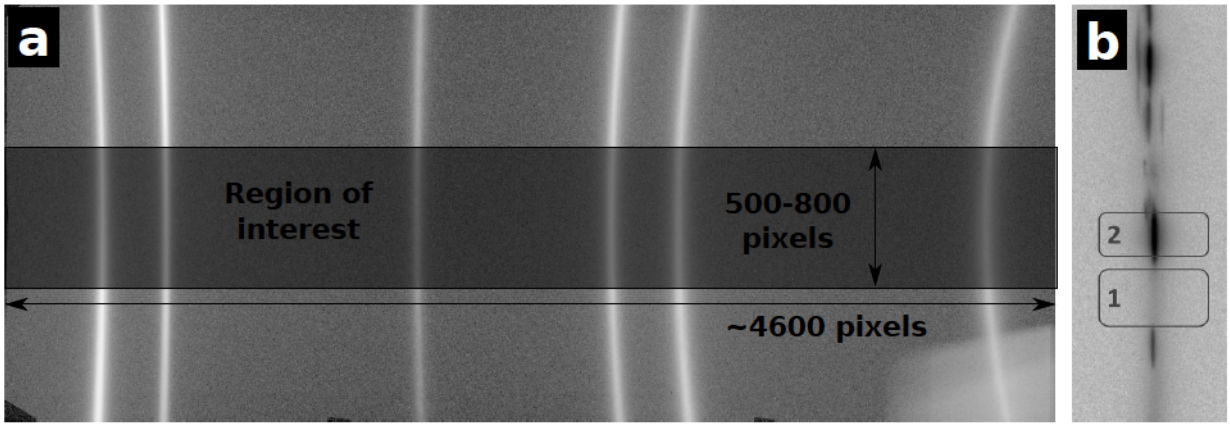

Figure 2.2: (a) Typical homogeneous intensity distribution in the Debye–Scherrer rings detected on an imaging plate. The lighter pixels indicate higher intensity. The peaks from left to right are the 311, 222, 400, 331, 420 and 422 reflections of a silver sample. In the figure the region of interest is also shown. (b) Magnified area of an inhomogeneous intensity distribution in another measurement for reflection 222 of a partially recrystallized silver sample showing narrow intensity spots diffracted by large grains (area 2) and the homogeneous intensity (area 1) obtained from fine grained volumes of the sample.

theoretical profile functions are calculated on the basis of a model of the microstructure. In this model, the crystallites have spherical shape and lognormal size distribution, and the lattice defect structure comprises dislocations and twin faults. This method gives both the dislocation density and the twin fault probability with good statistics, where the twin fault probability is defined as the fraction of the faulted $\{111\}$ planes along their normal vector. The two parameters of the crystallite size distribution function as well as the screw/edge character of the dislocation structure are also obtained from the evaluation. Figure 2.4 shows a fitted pattern.

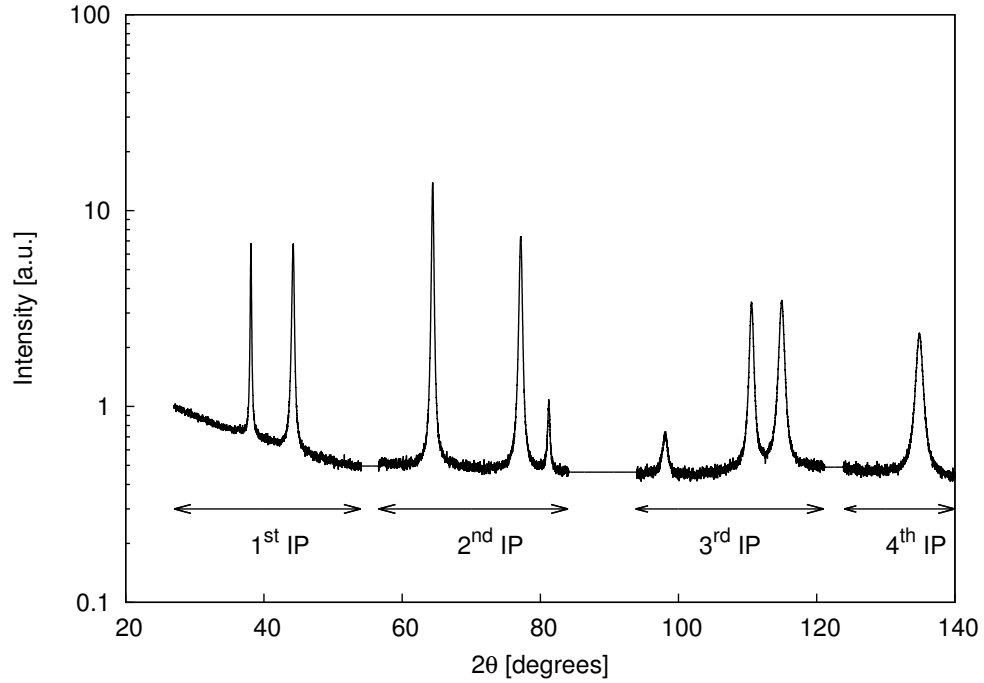

Figure 2.3: X-ray diffractogram of a silver sample measured with four imaging plates.

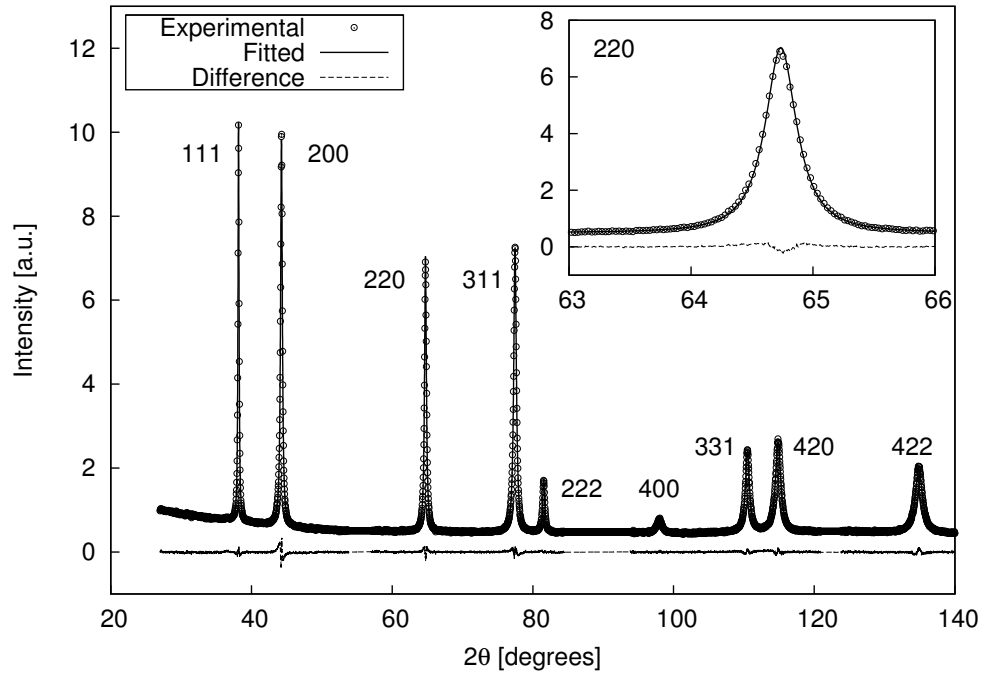

Figure 2.4: Fitted x-ray diffractogram. For a better visibility only every fifth experimental point is plotted. On the bottom of the figure the difference between the experimental and the fitted pattern is also shown. The inset shows the enlarged 220 reflection.

2.2 Microscopy Techniques

Transmission and Scanning Electron Microscopy

Since transmission electron microscopy (TEM) and scanning electron microscopy (SEM) are common techniqes in microstructure investigations, here only the experimental specialities are given.

The microstructures produced by ECAP, HPT, and rolling were examined using a Philips CM-20 transmission electron microscope operating at 200 kV. In the case of Ag the TEM samples were mechanically thinned to $\sim 50\,\mu$m, cooled to liquid nitrogen temperature and then thinned with 6 keV Ar^+ ions from both sides until perforation. Finally, the thin damaged surface layer was removed using 2 keV Ar^+ ions. Cu-Ag samples were prepared for TEM analysis by ion-beam polishing (Gatan PIPS 691, USA).

In the initial, annealed Ag samples, where the grain size was too large for TEM investigations, the microstructure was characterized by scanning electron microscopy. Before the SEM investigations, the Ag samples were polished using an alumina suspension with the particle size of $1\,\mu$m, then the samples were etched electrochemically usually using an A2 solution[5]. The quality of the etched surface was very sensitive to the etching conditions, therefore the solution was cooled to $5\,^\circ$C in order to slow down the etching process. Alternatively another solution[6] was also used. Sometimes the first solution gave better results, but in other cases the second solution was more effective.

For the Cu-Ag samples SEM analyses were carried out using Nova Nanosem 230 (FEI, USA) microscope.

Electron Backscatter Diffraction

The axial inhomogeneity of the grain structure in the HPT-processed specimens was studied on the cross-section of the disks by electron backscatter diffraction (EBSD) using an FEI Quanta 3D scanning electron microscope. First, the investigated surface was mechanically polished using an alumina suspension with an average particle size of 50 nm. Then, a $100\,\mu$m wide ditch was milled into the sample by focused ion beam (FIB) of Ga^+ ions with an inclination angle of 3° to the surface using an accelerating voltage of 30 kV and an ion current of 15 nA. The finest step size in the EBSD experiments was 20 nm.

[5] A2 solution is a standard product of Struers. Composition given by the manufacturer: 910 ml of A2:I containing 65-85% ethanol, 10-15% 2-butoxyethanol and 5-10% water; and 78 ml of A2:II which is perchloric acid (60%).

[6] 115 ml acetic acid, 43 ml concentrated sulphuric acid, 350 ml anhydrous methyl alcohol and 77 g tiourea (NH_2CSNH_2) [118]

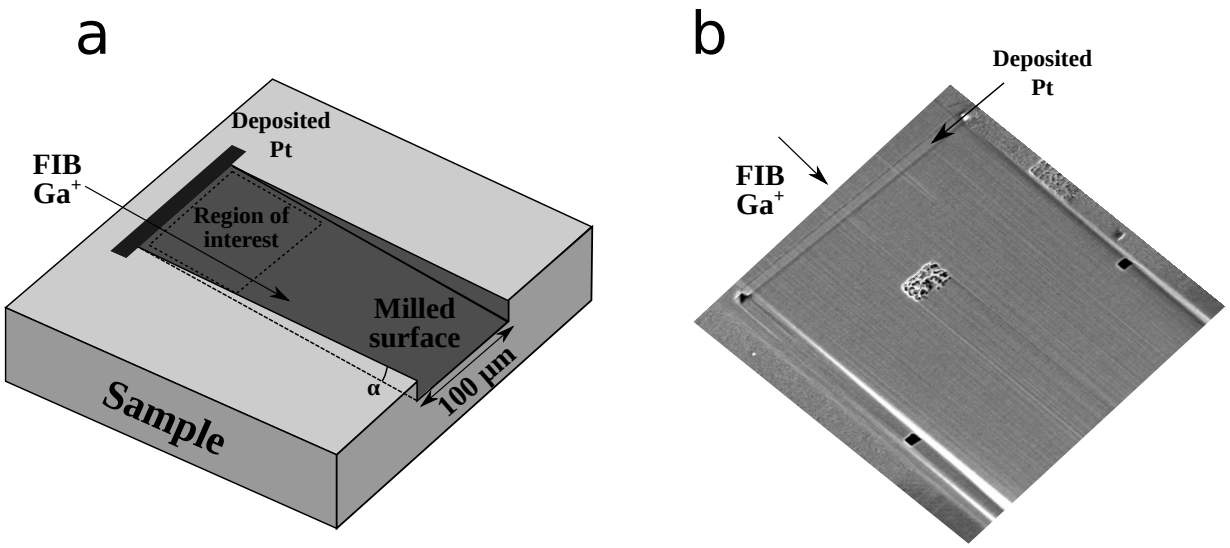

Figure 2.5: a) Schematic illustration of the FIB milling. α is the inclination angle (3°) of the Ga^+ ions to the surface of the sample. b) SEM image showing the sample during FIB milling procedure. In the middle of the milled area there is a trace of an earlier ion focusing process. It can be seen on the milled surface that it has a shallow fluctuation. This artifact can be minimized using the deposited Pt ribbon.

It should be mentioned that prior to the FIB milling a thin layer of Pt was deposited on the surface next to the region of interest as shown on figure 2.5. Using this Pt ribbon the fluctuations perpendicular to the FIB direction (see figure 2.5b) can be minimized.

In the case of Cu-Ag samples the EBSD analysis was carried out by a FEI Nova Nanosem 230 equipped with a TSL-OIM EBSD system.

When an EBSD measurement is carried out on a sample, the result is the well-known Kikuchi pattern, which can be indexed similar to a conventional diffraction pattern. If the surface of the sample is not enough clear or the beam is pointed on a grain boundary the Kikuchi pattern has low quality and the indexing procedure is nebulous, however if the surface is very clear and the beam is pointed on a single grain the Kikuchi pattern has a very high quality; this is called image quality (IQ). Each pixel on an EBSD picture has an IQ value, therefore the investigated area can be described by an IQ map. This is a gray-scale picture (see figure 2.6), on which the defects such as grain boundaries has deeper tone, since there the Kikuchi pattern has lower quality.

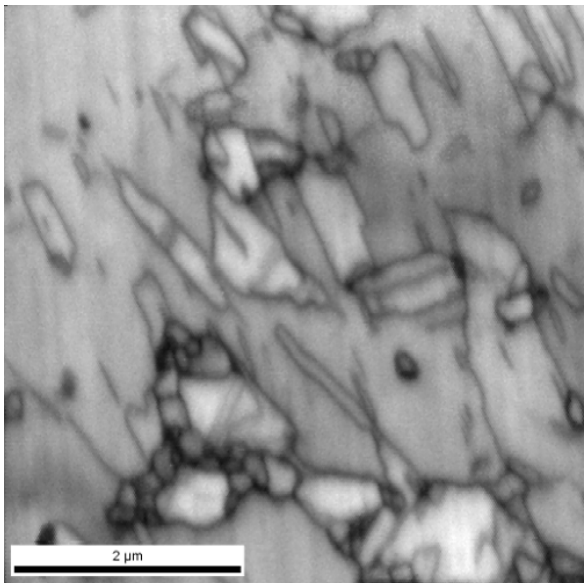

Figure 2.6: IQ picture showing UFG grains and twin boundaries in silver.

2.3 Mechanical Tests

2.3.1 Nano- and Microhardness

To examine the axial inhomogeneity of the HPT-samples, nanohardness measurements were carried out on the cross-sections at the center, half-radius and periphery of the disks, using a UMIS nanoindentation device with a Berkovich indenter and applying a maximum load of 5 mN. First the surface was fine polished, then a series of 400 indentations was recorded with the indents arranged in a 10×40 matrix with the distance of $15\,\mu$m between neighboring indents (see figure 2.7a). The indentation measurement was started and finished at a distance of $\sim 25\,\mu$m from the top and bottom surfaces of the disk and forty indentations were made parallel to the axial direction which corresponds to the total thickness of the disk ($650\,\mu$m). This process was repeated ten times, giving ten hardness values at each position along the axial direction. These ten measurements were then averaged, resulting in a mean nanohardness distribution along the axial direction of the HPT processed disk.

As an example a SEM image (figure 2.7b) shows four nanohardness indents on a polished surface of an Ag sample processed by 1 turn of HPT.

The microhardness of the samples was measured using a Zwick Roell ZHμ Vickers microhardness indenter with an applied load of 2000 mN and a dwell time of 10 s.

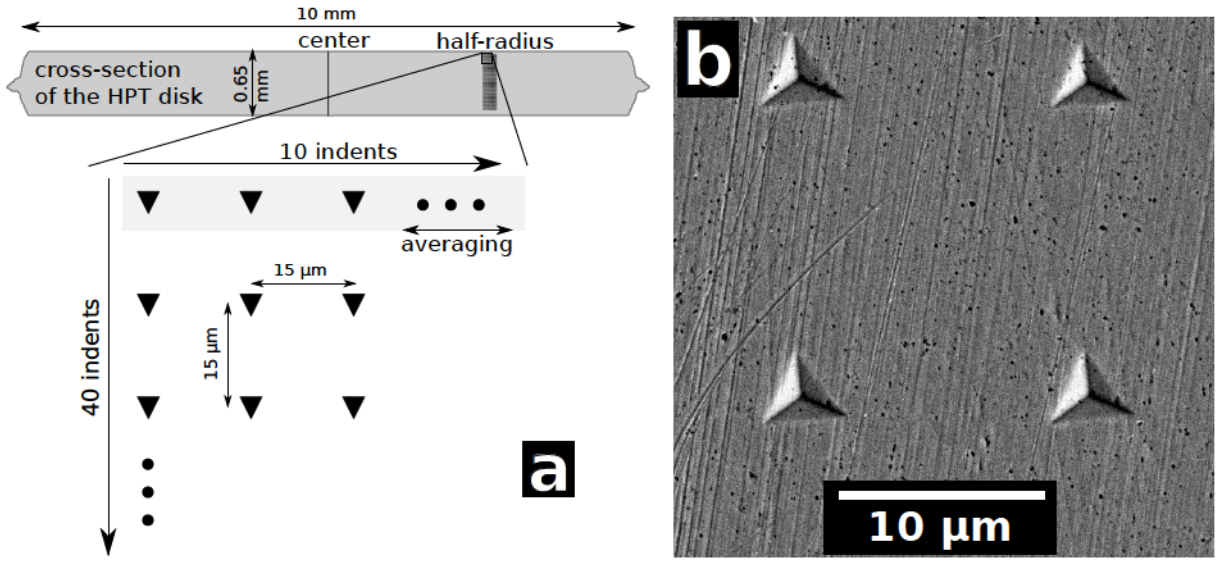

Figure 2.7: a) Nanoindentation layout on the cross-section of an HPT-processed disk. b) SEM image of four nanohardness indents taken on an Ag sample processed by 1 turn of HPT.

2.3.2 Uniaxial Compression

The deformation behavior of the ECAP-processed Ag samples was studied by uniaxial compression using a computer-controlled hydraulic mechanical testing MTS 810 machine. For all of these tests, the direction of compression was parallel to the longitudinal axis of the billet.

A typical stress–strain curve can be seen in figure 2.8. The yield strength (σ_y) is defined as the stress required for 0.2% plastic deformation. Figure 2.8 shows the fitted linear to the elastic range (dashed line) and the line with the same tangent corresponding to the 0.2% plastic deformation. In this thesis the flow stress (σ_f) is defined as the stress needed for approximately 10% plastic deformation.

Figure 2.8 shows the full stress–strain curve, however later only the plastic strain is shown without the elastic component.

2.4 Differential Scanning Calorimetry

Since differential scanning calorimetry (DSC) is a common technique in materials science, here only the specialities of the present investiations are given.

The thermal stability at elevated temperatures was investigated in Ar atmospehere by a Perkin

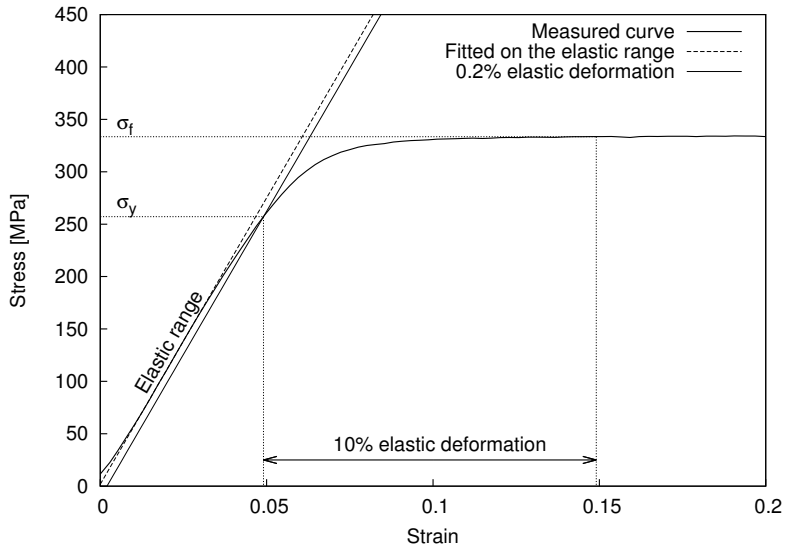

Figure 2.8: Typical true stress– true strain curve in a uniaxial compression test. σ_y is the yield strength and σ_f is the flow stress.

Elmer DSC2 calorimeter at a heating rate of 10 K/min[7]. The baseline of the DSC measurement was determined according to the second heat up cycle, then this baseline was subtracted from the measured signal and this final signal is referred to as DSC curve. The released heat during the DSC experiment was determined as the area under the DSC peak. The activation energy was determined from the shift of the peaks obtained at different heating rates using the Kissinger method [119].

2.5 Lattice Parameter Determination from X-ray Diffraction

The lattice parameter of a cubic lattice can be determined from equation (2.2). Due to the systematic errors (e.g. the uncertainty of the sample alignment) the d_{hkl} values determined from different hkl reflections usually do not give the same lattice constant. The systematic error decreases with increasing the Bragg-angle (2θ), therefore it is plausible to use the reflections having high 2θ to determine the lattice parameter. However, due to the angle dependence of the atomic scattering factor, as 2θ increases the intensity decreases, and the reflections with high 2θ have worst statistics, therefore the Bragg angle has larger error.

To minimize this error the Nelson–Riley method was used [120], in which the lattice parameter is

[7]For the activation energy measurements other heating rates were also applied.

determined by extrapolating the d_{hkl} values to $\theta = 90°$ using the following formula:

$$a_{hkl} = a_0 - \delta \cos\theta \left(\mathrm{ctg}\theta + \frac{\cos\theta}{\theta} \right), \tag{2.17}$$

where δ is a constant depending on the different systematic errors. Plotting the a_{hkl} values against $\cos\theta \left(\mathrm{ctg}\theta + \frac{\cos\theta}{\theta} \right)$, the intercept gives the lattice parameter (a_0).

2.6 Positron Annihilation Lifetime Spectroscopy

Positron annihilation spectroscopy (PAS) refers to several techniques (lifetime spectroscopy, Doppler-shift or angular correlation) based on the annihilation of thermalized positrons in the sample, however the most common applied method is positron annihilation lifetime spectroscopy. PAS proved to be a very efficient tool for the study of the microstructure of metals. In this section a brief overview of this technique is presented.

In the PAS experiment a β^+ decaying positron source is placed next to the sample and the emitted positron penetrates into the sample and annihilates there recombining with an electron. If the sample contains defects such as vacancies or microvoids, the lifetime of the positrons increases, since these defects may capture the positrons and the lower electron density in the defects results in a lower probability of annihilation. As the different type of defects have different trapping ability, the type of defects can be determined from the lifetime of the positrons. When more than one type of defect is present (and usually this is the case), positrons are captured at different trapping rates by the different defects, and the amount of defects may be calculated from the relative intensity of the signals corresponding to different lifetimes. In the last decades serious efforts were made to measure or determine theoretically the specific trapping rates of the different defects in many metals.

The annihilation of the positron is detected through the outcoming two γ photons having the specific energy of 511 keV in a coincidence measurement. Nevertheless a start signal is still needed for the lifetime measurement of the positrons. This signal is provided by the γ photon of the β^+ decay. The photons are detected by scintillation detectors. The principle of the PAS measurement is shown in figure 2.9a. Figure 2.9b shows the experimental layout with the two coincident scintillation detectors covering as large solid angle as possible.

In metals the positrons lifetime is typically in the order of $100 - 250$ ps and it increases to around $200 - 650$ ps if defects are present. For these extremely small time intervals fast spectrometers are essential.

The evolution of the vacancy concentration in silver samples was studied by PAS using a ^{22}Na

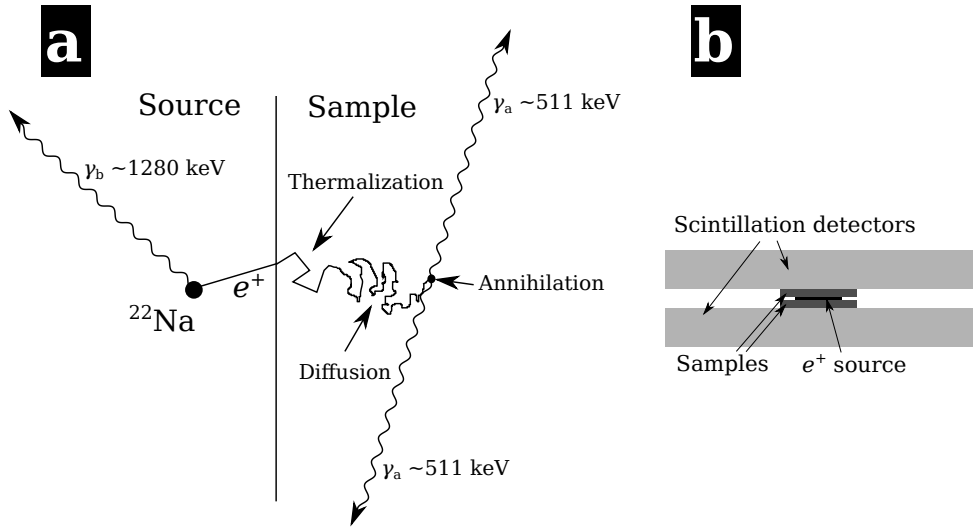

Figure 2.9: Schematic of the positron annihilation spectroscopy. The process theoretically with ^{22}Na source (a) and the measurement layout (b).

positron source with an activity of $\sim 10^5$ Bq covered by two Kapton foils with a thickness of $14\,\mu$m. The spectra was detected by a fast-fast spectrometer with a time resolution of ~ 205 ps and a channel time of about ~ 10 ps. About 1.5×10^6 counts were collected in each positron lifetime spectrum and this was fitted by the sum of three exponential components using the software RESOLUTION [121]. One of these components corresponds to the positrons annihilated in the source with fixed lifetime (390 ps) and intensity (14%). The second component arose from positrons annihilated in the bulk crystal with a lifetime between 92 and 110 ps [122, 123], while the third component corresponds to positrons trapped and annihilated at lattice defects such as vacancies and vacancy agglomerates. The concentration of these defects was calculated from the positron lifetime data applying the two-state simple trapping model with the specific trapping rate of $23 \pm 2 \times 10^{13}\,\mathrm{s}^{-1}$ [124].

Part II

Results

Chapter 3

Microstructure and Mechanical Properties of Silver Processed by Equal-channel Angular Pressing [R1–R4]

In this chapter I will show the development of microstructure (grain or sub-grain size, dislocation density, twin boundary probability) during ECAP deformation in silver. I will demonstrate the influence of the impurities on the evolution of the microstructure during the ECAP deformation. The mechanical properties of the samples will also be characterized by microhardness measurements and uniaxial compression tests.

3.1 Influence of the Impurity Level on the Evolution of Microstructure in Silver Processed by ECAP

Samples of silver of 99.99 at.% (4N) and 99.995 at.% (4N5) purity were manufactured by American Elements[1] and ESPI Metals[2], respectively. The alloying elements and their concentrations are listed in table 3.1. For both compositions, billets having lengths of ~ 70 mm and diameters of 10 mm were annealed at 741 K for one hour. This temperature corresponds to $0.6 \times T_m$, where T_m is the absolute melting point of Ag. The annealed samples were processed through 1, 4, 8 and 16 passes of ECAP at RT with a pressing velocity of $8\,\mathrm{mm} \cdot \mathrm{s}^{-1}$. The pressing was conducted using route B_c where the billet was rotated in the same sense by 90° about its longitudinal axis after each pass[3]. The ECAP die had an internal channel angle of 90° and an outer arc of curvature of 20°. In this configuration one pass corresponds to an equivalent strain of ~ 1 according to equation (1.5).

The values of the mean grain size were about 60 μm in the initial state of the samples after the one hour annealing irrespectively of their level of impurity. In figure 3.1 SEM images show the microstructure of both samples. The difference between the two pictures was caused by the different etching conditions during the sample preparation. In the 4N5 purity sample (left image) the grain boundaries were well etched, whereas for the 4N purity sample (right image) the effect of etching on grain boundaries was weak. This difference was most probably caused by the various types and concentrations

[1] http://www.americanelements.com/

[2] http://www.espimetals.com/index.php

[3] For further information about the ECAP routes see subsection 1.1.2

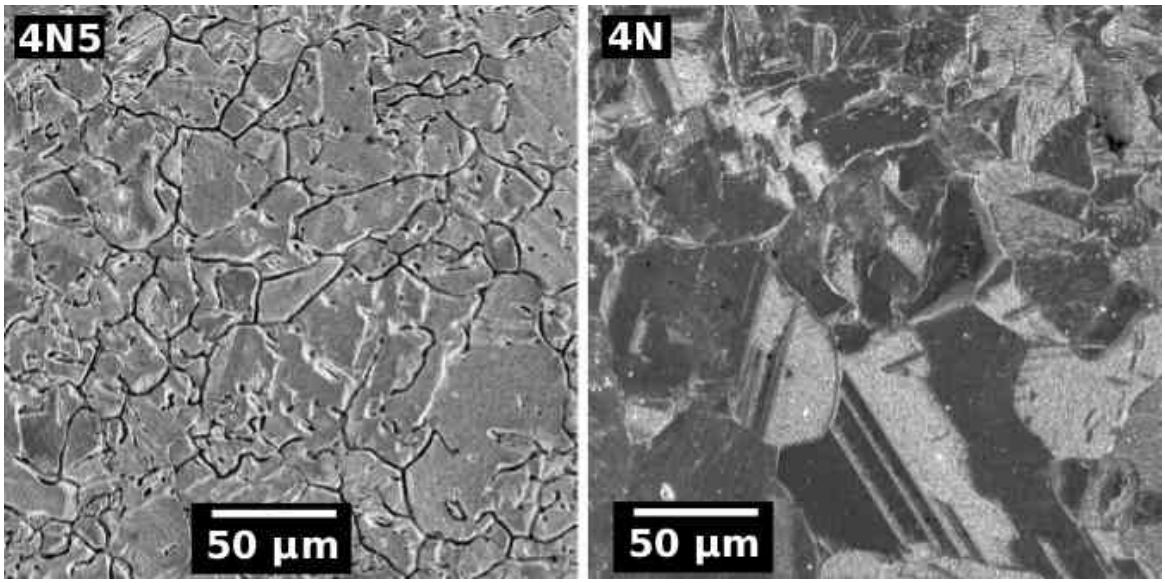

Figure 3.1: SEM images showing the microstructure of the initial samples with different impurity levels after annealing.

of impurities in the two samples. Figure 3.2 shows the large scale SEM images of the 4N5 (left) and the 4N purity samples processed by 1 pass of ECAP. After 1 pass of ECAP the grain size reduced to $\sim 20\,\mu$m in both samples.

Figure 3.3 illustrates the grain structure in the samples processed by 4, 8 and 16 passes of ECAP. The mean grain size was slightly higher than 200 nm after 4 passes irrespectively of the impurity level and further ECAP deformation resulted in only minor additional grain refinement. Since the mean grain size of the two series of samples were similar, one can conclude that the two times larger impurity content in the present case did not affect significantly the minimum grain size achievable by ECAP.

The dislocation density and the twin boundary frequency were determined by x-ray line profile

Table 3.1: Chemical composition of the samples (in *ppm*).

4N	Ag	Cu	Pd	Fe	Se	Sb	Bi		sum.
(99.99 %)	bal.	30	10	10	10	10	20		90
4N5	Ag	Cu	Pb	Fe	Se	Ir	Au	Pd	
(99.995 %)	bal.	13	14	5	6	6	10	2	56

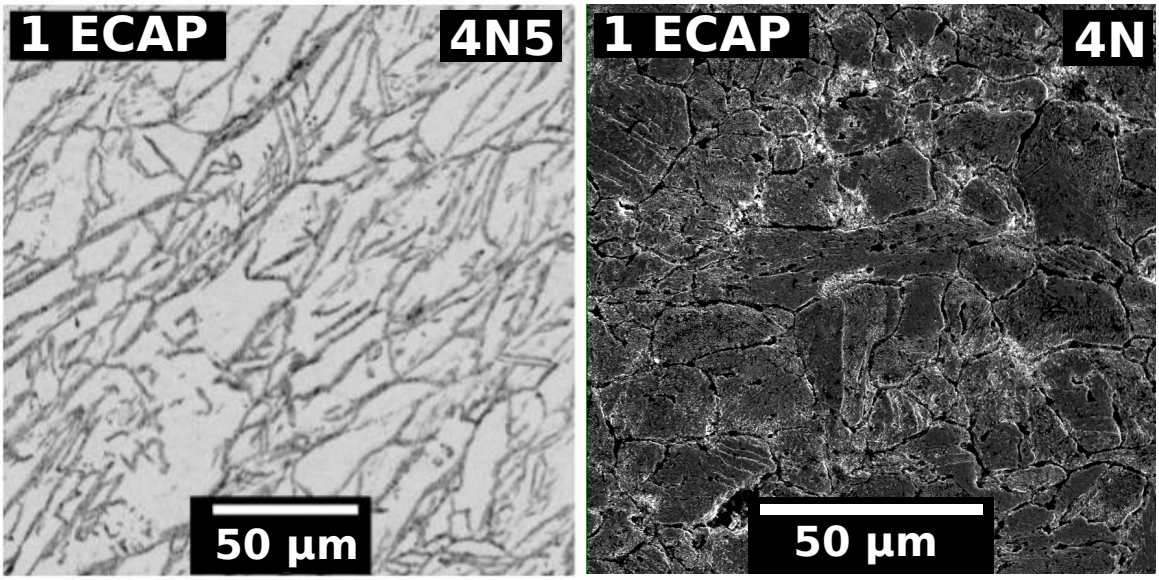

Figure 3.2: SEM images showing the microstructure of the 4N5 (left) and the 4N purity (right) samples processed by 1 pass of ECAP.

analysis[4]. In figure 3.4 the dislocation density and the twin boundary frequency are plotted as a function of the number of ECAP passes for 4N5 and 4N purity Ag. For both series, the evolution of the dislocation density was similar, increasing up to 8 passes and then decreasing. For 1 pass the dislocation density was larger for 4N purity Ag ($26 \pm 4 \times 10^{14}\,\mathrm{m}^{-2}$) than for the more pure 4N5 sample ($16 \pm 2 \times 10^{14}\,\mathrm{m}^{-2}$). Gallagher [125] has shown that both the impurities and solid solution alloying reduce SFE in Ag. As for small impurity contents, the relative change of SFE has the same order of magnitude as the impurity concentration. Therefore in the present materials where these concentrations are not more than 10^{-4} the reduction of SFE due to contamination is marginal. As a consequence, the equilibrium splitting distances calculated for screw (2.6 nm) and edge dislocations (6.5 nm) in pure Ag can be used for both 4N and 4N5 purity samples[5]. The high degree of dislocation dissociation due to low SFE hindered dislocation annihilation, led to a large dislocation density even after the first pass of ECAP. As this effect was similar for the two compositions, the larger dislocation density in 4N Ag after 1 pass can be explained solely by the stronger pinning effect of the larger concentration of impurities that hinders dislocation annihilation.

In addition to dislocation glide, twinning also contributes to plastic deformation for both impurity levels. In the TEM images of figure 3.3 some twin boundaries are indicated by white arrows. The

[4]For more details see section 2.1

[5]For more details about the splitting distances see section 1.3

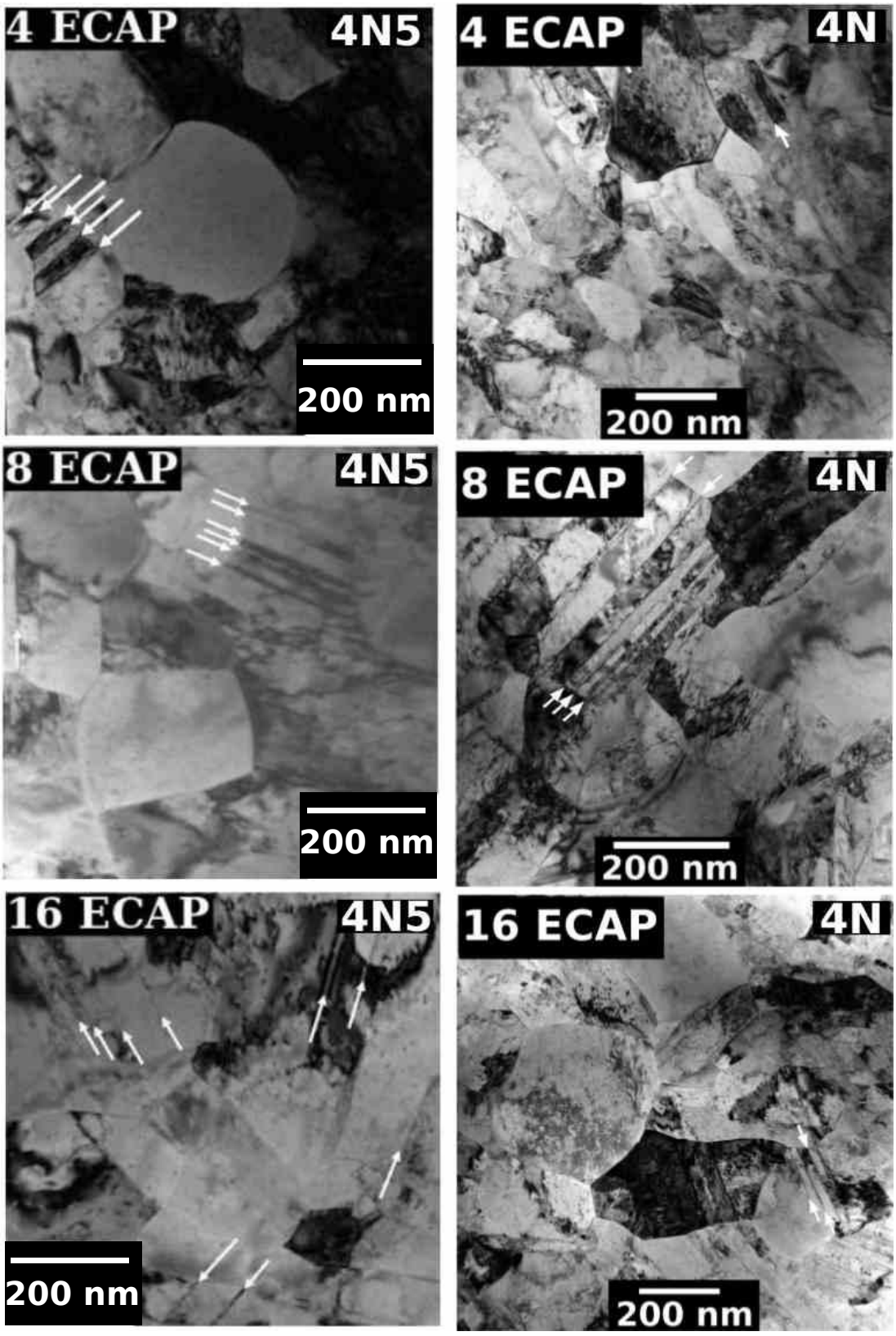

Figure 3.3: TEM images showing the microstructures of the 4N5 and the 4N purity Ag samples after different passes of ECAP: examples for twin boundaries are indicated by white arrows.

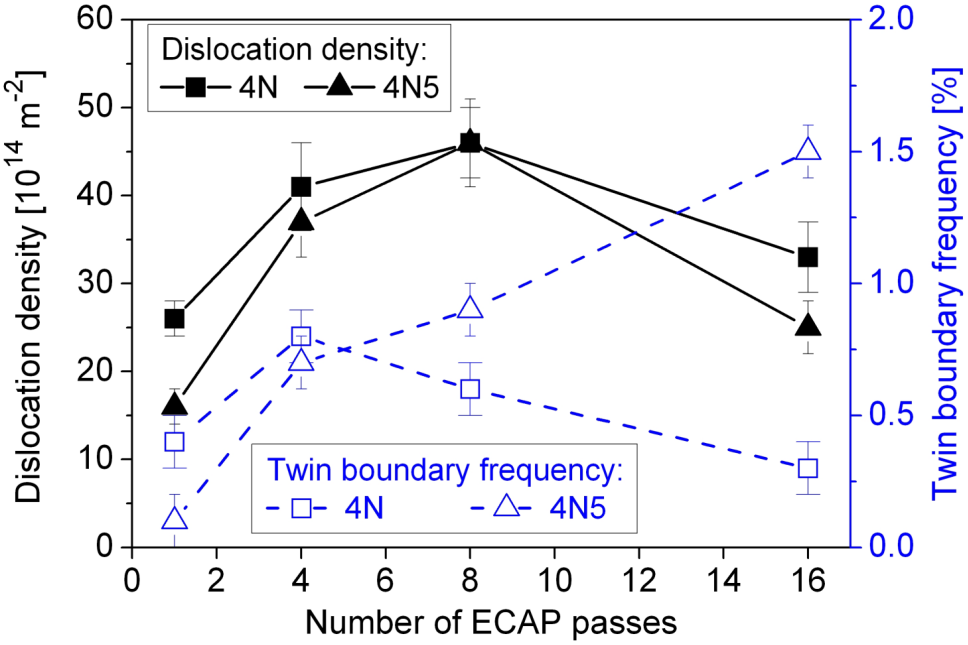

Figure 3.4: The variation of the dislocation density and the twin boundary frequency with the number of ECAP passes for the 4N5 and 4N purity Ag.

twin sources are usually located at dislocation glide obstacles such as Lomer–Cottrell locks or grain boundaries where the local stress exceeds the critical stress needed for twin nucleation [59]. The larger dislocation density in 4N purity Ag processed by 1 pass increases the number of twin nucleation sites at glide obstacles, thereby leading to a higher twin boundary frequency than in 4N5 Ag.

For both impurity contents, the dislocation density increased with increasing number of passes and saturated after 8 passes with a very large value of $46 \pm 5 \times 10^{14}\,\mathrm{m}^{-2}$ as compared to other pure fcc metals processed by ECAP at RT[6]. This large dislocation density can be attributed to the retarded annihilation due to the high degree of dislocation dissociation. After 8 passes of ECAP, the grain size was reduced to 200 nm and the majority of impurities are most probably segregated at the grain boundaries as was shown for other UFG materials [128]. As a consequence, there was a reduction in the difference between the impurity concentrations along dislocations inside the grains in 4N5 and 4N samples that led to similar saturation dislocation densities for the two compositions. In addition to cross-slip and climb, twinning also contributes to the annihilation of dislocations as the lattice dislocations were dissociated into twinning partials at glide obstacles and a twin forms by slipping of these partials in neighboring {111} lattice planes [65, 129–131]. As the twin boundaries obstruct the activity of dislocation glide sources [59], therefore the thermally activated annihilation

[6]The saturation dislocation density for other pure fcc metals are $2 - 8 \times 10^{14}\,\mathrm{m}^{-2}$ for Al [96], $20 - 21 \times 10^{14}\,\mathrm{m}^{-2}$ for Cu [52, 126] and $17 \times 10^{14}\,\mathrm{m}^{-2}$ for Au [127]

and the dissociation due to twinning give a reduction in the dislocation density in Ag between 8 and 16 passes. A similar decrease of the dislocation density due to dynamic recovery was observed also in Cu processed by more than 8 passes in ECAP [132].

After 4 passes the evolution of the twin boundary frequency was different for 4N5 and 4N samples (see figure 3.4). In the former case, the twin boundary frequency increased monotonously up to 16 passes while for 4N specimens it decreased slightly after 8 passes. As was noted, after 4 passes the grain size was reduced to ~ 200 nm and, due to the large number of grain boundaries, the twins were mainly nucleated at the grain boundaries as was already observed for other nanomaterials [133]. The impurities and the alloying atoms in solid solution are usually segregated at grain boundaries during SPD at RT [128]. As a consequence, the higher impurity content in 4N Ag hindered the nucleation of twins at grain boundaries. The interaction of dislocations and twins gave untwining inside the grains [59]. Therefore, the reduced activity of twin sources at the grain boundaries in 4N purity Ag led to a significant decrease in the total twin boundary frequency after 16 passes. Between 8 and 16 passes, the lower twin formation rate in 4N purity Ag contributed to the smaller reduction of the dislocation density compared to the 4N5 purity material.

3.2 Mechanical Properties

Figure 3.5 shows the true stress – true strain compression curves for the 4N purity samples after different number of ECAP passes. The compression curve of the initial annealed sample is also shown, which exhibits a considerable work hardening. It can be seen that the first pass of ECAP caused a significant change. After 4 passes of ECAP the compression curve was very similar to the one obtained after 1 pass of ECAP, but both the yield strength and the flow stress[7] was higher. Further passes of ECAP caused only minor changes as it is illustrated on figure 3.5, however in the 4N purity sample after 16 passes the flow stress decreased slightly.

The yield strength, the flow stress and the microhardness of the 4N5 and the 4N samples after different number of ECAP passes can be found in table 3.2. After the first pass of ECAP, both the yield strength and the microhardness increased drastically from about 35 MPa and 0.4 GPa to 266 MPa and 0.9 GPa, in the 4N5 purity sample and from 38 MPa and 0.45 GPa to 255 MPa and 0.9 GPa in the 4N purity sample respectively. After 4 passes the yield strength and the flow stress reached a saturation value parallel to the microhardness. These saturation values were 260 ± 10 MPa, 330 ± 10 MPa and 1.1 GPa for the yield strength, the flow stress and the microhardness, respectively. Further

[7] The definition of the yield strength as well as the flow stress can be find in section 2.3.2.

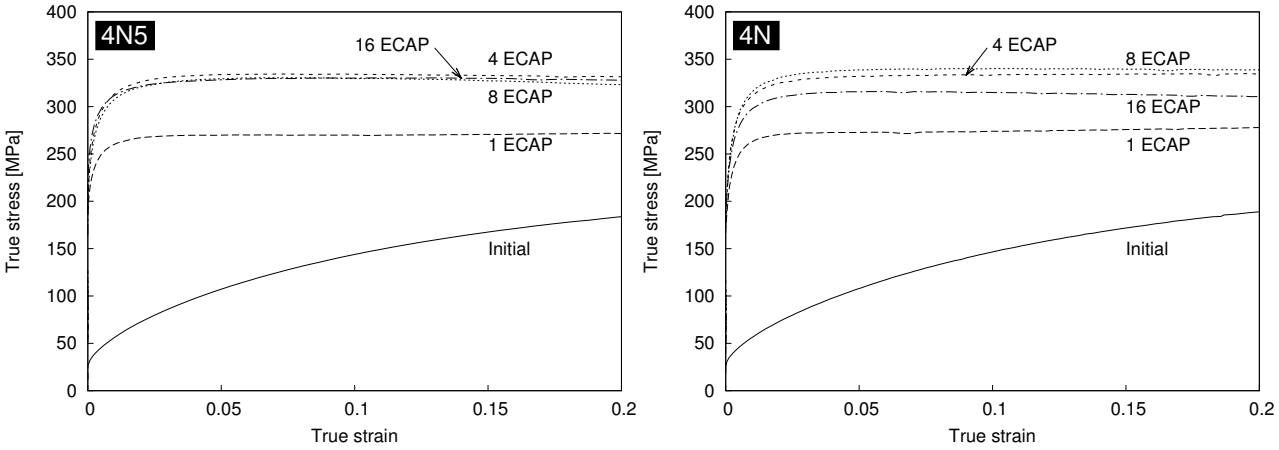

Figure 3.5: True stress – true strain uniaxial compression curves for the 4N5 (left) and 4N (right) purity samples. The compression curve of the initial sample is also shown.

passes caused only negligible effect on the measured mechanical properties, except of the 16 passed 4N sample, which shows a minor decrease in its flow stress.

Table 3.2: The yield strength (σ_y), the flow stress (σ_f) and the Vickers-microhardness (HV) for the 4N5 and the 4N purity samples after different number of ECAP passes. For the 4N5 purity sample processed by 16 passes of ECAP the yield strength was not determined, because the elastic part of the curve was too unprecise.

	4N5			**4N**		
	σ_y [MPa]	σ_f [MPa]	HV [GPa]	σ_y [MPa]	σ_f [MPa]	HV [GPa]
Initial	35 ± 10	–	0.4 ± 0.1	38 ± 10	–	0.45 ± 0.1
1 ECAP	233 ± 10	270 ± 10	0.9 ± 0.1	223 ± 10	275 ± 10	0.9 ± 0.1
4 ECAP	266 ± 10	334 ± 10	1.1 ± 0.1	255 ± 10	336 ± 10	1.1 ± 0.1
8 ECAP	260 ± 10	330 ± 10	1.1 ± 0.1	253 ± 10	336 ± 10	1.1 ± 0.1
16 ECAP	–	332 ± 10	1.1 ± 0.1	247 ± 10	314 ± 10	1.1 ± 0.1

For the 4N5 samples after 16 passes the dislocation density decreased and the twin boundary probability increased (for details see figure 3.4), whereas the yield strength[8] remained unchanged. The decrease of the dislocation density should result in the decrease of the yield strength of the material. At the same time, the increase in the twin boundary frequency is in fact a decrease of the grain size. As it is well known according to the Hall–Petch relation (equation (1.1)) the decrease of the grain size

[8]The yield strength was also determined from the stress–strain curves.

causes an increase in the yield strength. It seems that these two opposite effects extinguish each other in this particular case results in a constant yield strength.

For the less pure 4N sample both the dislocation density and the twin boundary frequency decreased after 16 passes of ECAP, however the decrease of the dislocation density was less significant as for the 4N5 sample. After all, it seems that the decrease of both microstructural parameters resulted in the slight decrease of both the flow stress and the yield strength, although this decrease was only about 7%.

It can be concluded that the small difference between the impurity concentrations did not cause significant variation in the grain size, the flow/yield strength and the hardness in ECAP-processed silver. However, the evolution of the defect structure (e.g. dislocations and twin boundaries) differed considerably in the 4N5 and 4N purity materials, which has an influence on the thermal stability of UFG microstructures, as it will be shown in the next chapters.

Chapter 4

Thermal Stability of ECAP-processed Silver at Room Temperature [R2, R3, R5–R7]

In this chapter the room temperature thermal stability of silver with different impurity concentrations processed by ECAP is discussed. During storage at room temperature, samples with high enough previous deformation show self-annealing, which manifests in different degree of recovery and recrystallization as was observed parallel by microhardness measurements and x-ray line profile analysis. The uniaxial compression test, made after storage at room temperature, provide direct evidence that self-annealing was not only a surface effect, but it was extended to the whole volume of the samples.

There was a significant difference in the room temperature thermal stability between the 4N5 and 4N samples induced by their different microstructural evolution during the equal-channel angular pressing deformation, as was discussed in chapter 3. The 4N5 samples appeared to be less stable during the four months of storage, which is a consequence of their higher twin boundary frequency after the deformation, while the slightly higher concentration of impurities in the 4N samples hindered the annihilation of dislocations, through this delaying the recovery process.

4.1 The Mechanical Properties During Storage at Room Temperature

Figure 4.1 shows the microhardness of the samples (4N5 on the left and the 4N on the right) processed by different passes of ECAP as a function of the time of storage at room temperature, where the lower horizontal line denotes the hardness of the initial sample. It is apparent that the hardness after 1 pass remains unchanged within experimental error even after storage for 4 months for both compositions. By contrast, for the 4N5 samples the hardness gradually decreases with increasing storage time for the samples processed by 4, 8 and 16 passes thereby demonstrating that the severely deformed microstructure is inherently unstable and subject to self-annealing, most probably by recovery and recrystallization, during long-term storage at room temperature. For the 4N purity samples there were only a slight decrease in the microhardess values during the 4 months period of storing. It seems that, despite the very small difference in the impurity content between the 4N5 and the 4N samples, it influenced the stability of the microstructure effectively since the degree of recovery and recrystallization is considerably smaller for the 4N samples. For this reason, in the following mainly the results obtained

on the 4N5 samples will be shown.

Uniaxial compression tests were made after different times of storage at RT to clarify that the softening, which was experienced in the microhardness measurements, has occurred in the whole volume of the samples. Figure 4.2 shows compression true stress – true strain curves obtained on the samples processed by ECAP right after the ECAP deformation and after 4 months of storage at RT as examples showing the variance during the storage. It is clear that there was no change in the 1 passed sample, as the solid and the dashed lines representing the compression curves obtained immediately after ECAP deformation and after 4 months of storage, respectively, are similar. At the same time, remarkably change took place after higher number of ECAP passes. After 4 months at RT the compression curve is more like the initial sample, than its former state, implying a considerable microstructural similarity, which means that the recovery and recrystallization occurred in the whole volume of the sample not only on its surface. The softening was the strongest in the sample processed by 16 passes of ECAP.

4.2 Microstructure Changes During Storage at Room Temperature

Figure 4.3 shows TEM images of the 4N5 sample after 8 passes of ECAP and after 4 months of storage at RT. Figure 4.3a shows the UFG microstructure achieved during the 8 passes of ECAP, whereas figure 4.3b shows that during storage essential changes took place. The grain size increased from about 200 nm to several microns. This grain growth during storing at RT resulted in the experienced softening of the 4N5 samples.

The microhardness measurements showed that the softening process is considerably slower in the 4N samples since the microhardness of these samples showed only a slight decrease after 4 months of storage at RT (see figure 4.1). This difference of the RT thermal stability of the samples was confirmed by TEM experiments as well. Figure 4.4 shows bright field TEM images (a) taken on the 4N5 sample processed 8 passes of ECAP after 4 months of storage at RT and (b) on the 4N sample also processed by 8 passes of ECAP but after 1 year of storage at RT. On the 4.4a image only large grains can be seen[1]. However at the middle left of image 4.4b a remained UFG region can be seen. Despite that these TEM images were taken on very large areas (to TEM investigations), the absence of UFG regions on image 4.4a does not imply that there are no remained UFG regions[2] in the 4N5 sample after 4 months of

[1]These grains are recrystallized grains as was proven by XLPA mesaurements, see later in this section

[2]In section 4.2 clear evidence is presented for the presence of UFG regions in the 4N5 samples after 4 months of storage at RT.

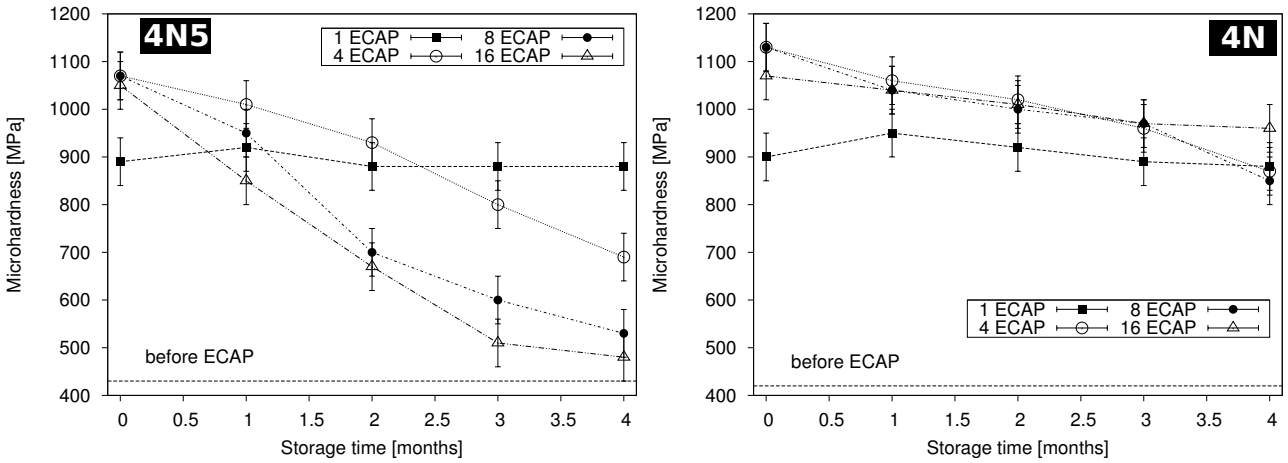

Figure 4.1: Values of the microhardness after processing by ECAP for 1, 4, 8 and 16 passes as a function of the storage time at room temperature for the 4N5 (*left*) and the 4N (*right*) purity Ag. The dashed lines at the bottom of both figures show the initial microhardness of the annealed samples before ECAP deformation.

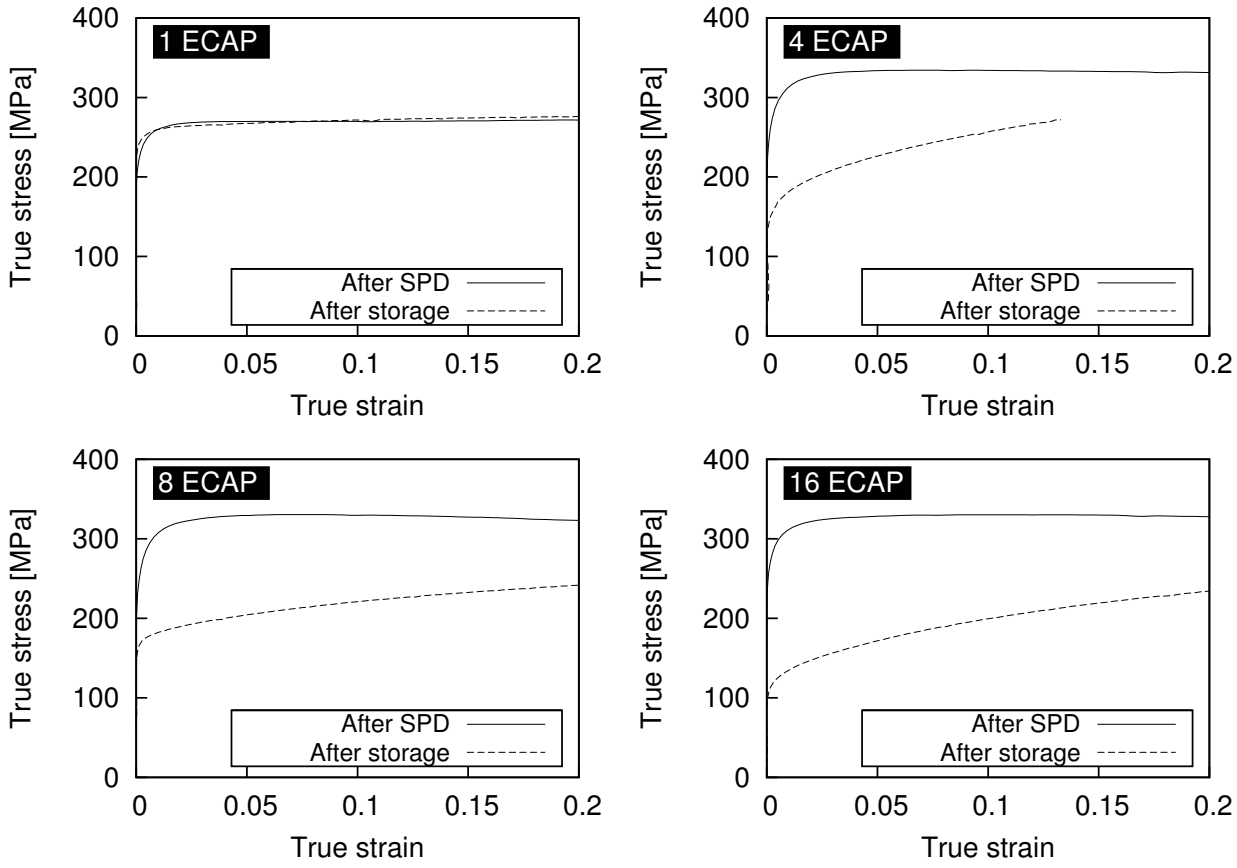

Figure 4.2: True stress – true strain curves for the 4N5 purity level samples processed by different number of ECAP-passes obtained by uniaxial compression test. The solid lines represent compression curves right after the ECAP deformation, while their dashed line counterparts were made after 4 months of storage at RT.

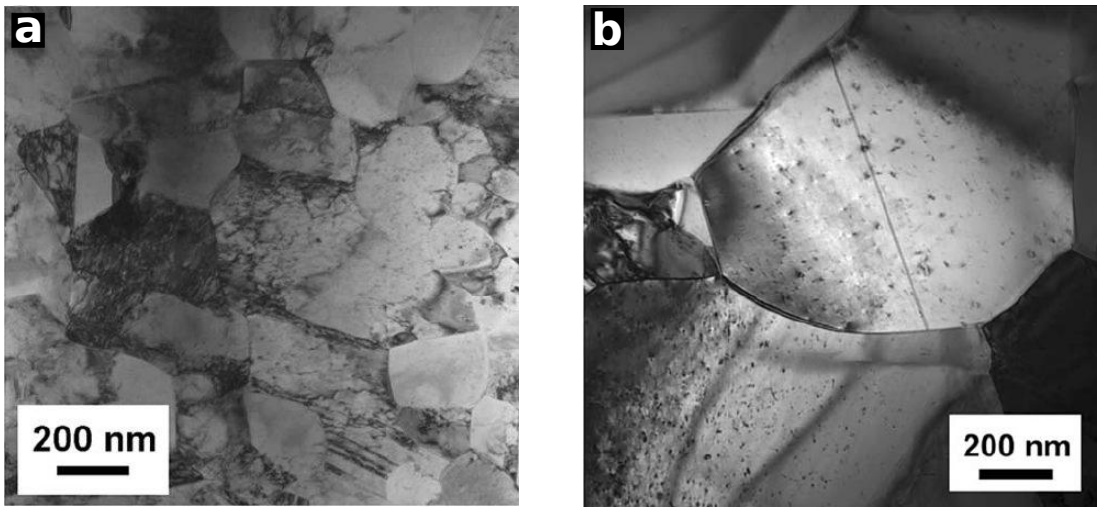

Figure 4.3: TEM images taken on the 4N5 sample immediately after 8 passes of ECAP deformation (a) and after 4 months of storage at RT (b).

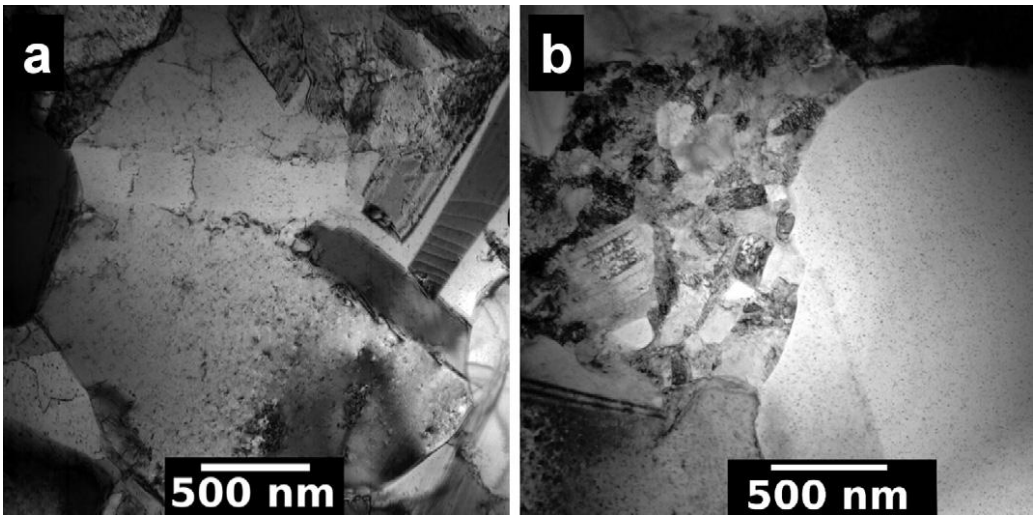

Figure 4.4: Bright field TEM images showing the microstructures of (a) the 4N5 purity sample processed through 8 ECAP passes and stored at room temperature for 4 months and (b) the 4N purity specimen after 8 ECAP passes and storage for 1 year.

storage at RT, but their presence is most probably less frequent.

To understand the mechanisms of the observed softening and grain coarsening (most probably by recovery and recrystallization) during storage at RT, the dislocation density and the twin boundary probability were determined as a function of the storage time for both the 4N5 and the 4N purity sample series using x-ray diffraction line profile analysis. Figure 4.5 shows the Debye–Scherrer diffraction

rings of the 2 2 0 reflection obtained (a) immediately after 8 passes of ECAP and (b) after 4 months of storage at room temperature for the 4N5 sample. Immediately after the ECAP deformation the intensity distribution around the ring is relatively homogeneous, thereby indicating a high degree of homogeneity within the microstructure. Similar diffraction rings were also recorded for the other 4N5 purity samples immediately after processing by ECAP. After 1 month of storage at RT for the 4N5 samples processed through 4, 8 and 16 passes high intensity spots were observed on the Debye–Scherrer rings. Furthermore, these irregularities in intensity became even more visible after storage for 4 months. Figure 4.5b shows an example for the 2 2 0 reflection obtained on the 4N5 sample after processing through 8 passes and storing for 4 months.

The inhomogeneous intensity distributions in the Debye–Scherrer rings suggest there is a fluctuation in the degree of self-annealing within the microstructure. Since the breadths of the individual high intensity spots were close to the instrumental broadening, it was not feasible to evaluate these parts of the diffraction rings quantitatively. However, these high intensity spots are most probably scattered from recrystallized grains having larger sizes and lower dislocation densities than the detection limits of the line profile analysis ($\sim 800\,\mathrm{nm}$ and $\sim 10^{13}\,\mathrm{m}^{-2}$ for the crystallite size and the dislocation density, respectively) and the rather homogeneous portions of the Debye–Scherrer rings are most probably related to the recovered volumes. The Debye–Scherrer rings for the samples processed for 4 and 16 passes also became inhomogeneous during storage at RT.

The narrow spots in the Debye–Scherrer rings originated from the recrystallized volume of the samples were too narrow for investigation. Nevertheless, the homogeneous background of the rings, which came from the recovered volume of the samples, were eligible for qualitative evaluation. In this case a homogeneous part of the ring without high intenesity spots was cut for each reflection, which yields a peak profile related to the non-recrystallized regions. Therefore, it is essential to note that the subsequent results pertain only to the recovered regions of the samples and do not characterize the whole volume.

The dislocation density and the twin boundary probability evaluated from the homogeneous portions of the rings are shown as a function of the storage time in figures 4.6a and 4.6b, respectively, for the 4N5 samples. For the sample processed by 1 pass the dislocation density in figure 4.6a remains essentially unchanged whereas after 4, 8 and 16 passes the dislocation density decreases with the time of storage. The reduction in the dislocation density is fastest after 8 passes, but stops after about 1 month when it reaches the value characteristic of the sample processed only by 1 pass ($\sim 16 \times 10^{14}\,\mathrm{m}^{-2}$). For the specimen deformed by 4 passes, the dislocation density decreases more slowly and after 2 months it also converges to the same value. For 16 passes, the dislocation density decreases only slightly from $\sim 25 \pm 3 \times 10^{14}\,\mathrm{m}^{-2}$ to $\sim 20 \pm 3 \times 10^{14}\,\mathrm{m}^{-2}$ during 4 months of storage, but a further reduction during

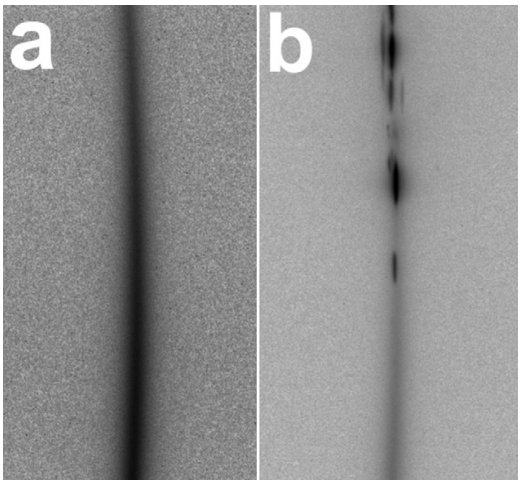

Figure 4.5: Debye–Scherrer rings of the 2 2 0 reflection, obtained on the 4N5 purity samples. (a) immediately after 8 ECAP passes, (b) after 4 months of storage at RT. The narrow intensity spots in figure (b) originated from the recrystallized volumes with large grain size and low dislocation density. The height of these images is about 1200 pixels.

storage for a longer time cannot be excluded. It is concluded that there is a more rapid reduction during storage when there is a higher initial dislocation density. Figure 4.6b shows that the twin boundary probability remains practically unchanged for specimens processed through 1, 4, and 8 passes, but for the 16 passes sample the twin probability decreases from $\sim 1.5 \pm 0.1\%$ to $\sim 1.1 \pm 0.1\%$ during the first month of storage and thereafter remains unchanged. It should be noted again that the defect densities plotted in figure 4.6 were determined from the homogeneous parts of the Debye–Scherrer rings which are free from the large intensity spots. Consequently, these values are characteristic only of the recovered parts of the samples and most probably the mean dislocation density and twin probability are lower for the whole specimens due to the contributions from the recrystallized fractions of the samples.

4.3 Discussion on the Room Temperature Thermal Stability

4.3.1 The Possibility of Delayed Recovery of the Dislocation Structure by Cross-slip

The present experiments provide clear evidence for the self-annealing of 4N5 Ag samples at RT after processing by at least 4 passes of ECAP. The x-ray diffraction and TEM results demonstrate that both delayed recovery and recrystallization occur during self-annealing. During recovery, the screw and edge dislocations are annihilated by cross-slip and climb, respectively. The probability of the occur-

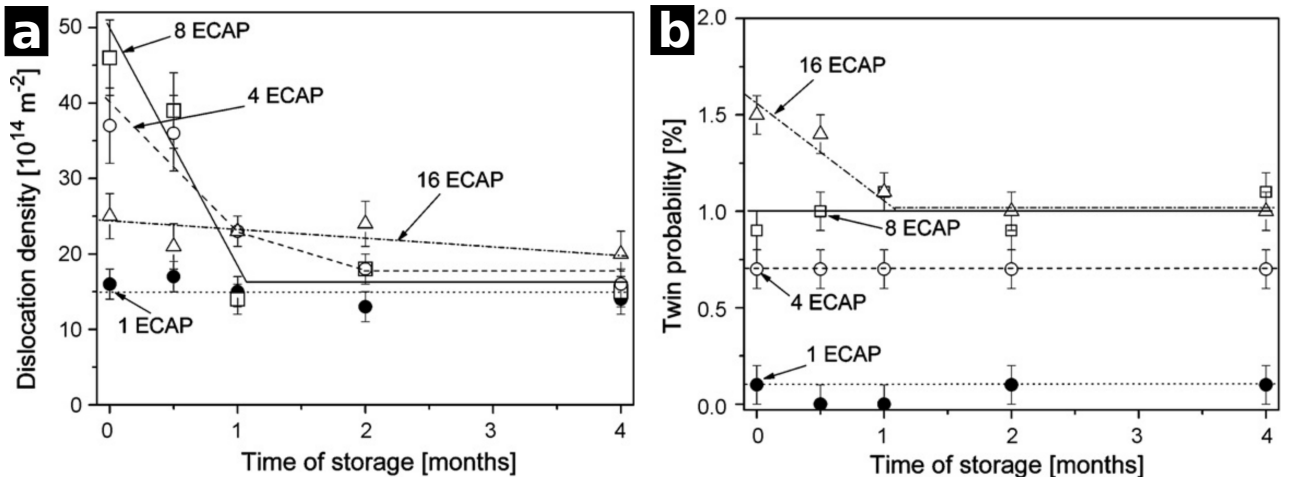

Figure 4.6: (a) The dislocation density and (b) the twin probability in the recovered volumes of 4N5 samples stored at room temperature for up to 4 months after processing by ECAP through 1, 4, 8 and 16 passes.

rence of these mechanisms is dependent upon the degree of dislocation dissociation. As was mentioned in section 1.3, in fcc metals the lattice dislocations are dissociated into partials bordering a ribbon of stacking fault. The equilibrium splitting distance (d_p) between these partials is given by equation (1.10) and listed in table 1.1. These calculations show that the splitting distance is exceptionally high in Ag because of the very low SFE.

This high degree of dislocation dissociation impedes by cross-slip. In the cross-slip model developed by Friedel [134], cross-slip occurs in fcc crystals by the formation of an initial constriction in the dissociated dislocation and the subsequent extension of this constricted segment onto the cross-slip plane. The cross-slip process (illustrated in figure 4.7) is stress-assisted because the activation energy of the process is reduced by the shear stress, σ_1, pushing the partials towards each other on the initial glide plane (S_1) and by the shear stress, σ_2, pulling the partials in opposite directions on the cross-slip plane (S_2). The energy, W, required for cross-slip is given by the relationship [135]:

$$W = W_0 \left(1 - 1.2\frac{\sigma_2 b}{\gamma} - 1.5\frac{\sigma_1 b}{\gamma}\right), \tag{4.1}$$

where b is the magnitude of the Burgers vector of the full lattice dislocation, γ is the stacking fault energy and W_0 is the constriction energy which is given by

$$W_0 = \frac{Gb^2 d_p}{37}\left(\ln\left(\frac{2\sqrt{3}d_p}{b}\right)\right)^{1/2}, \tag{4.2}$$

where d_p is the equilibrium splitting distance between the partials and G is the shear modulus.

Although there are other slightly different relationships for the constriction energy [136, 137], the

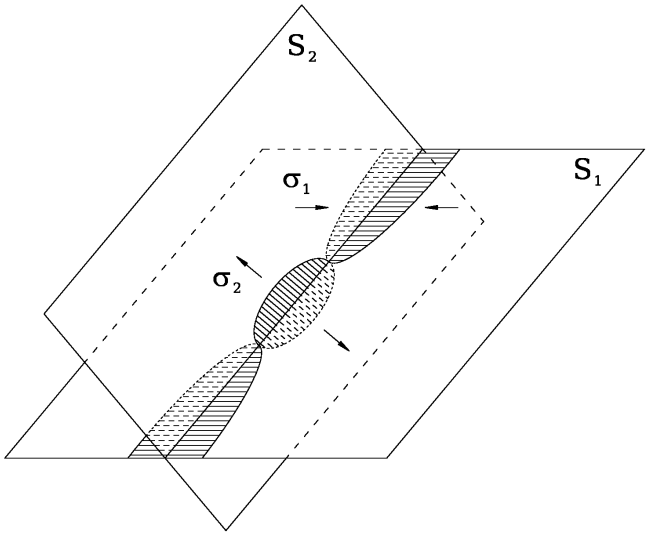

Figure 4.7: Schematic of the cross-slip process of a screw dislocation from the S_1 to the S_2 glide plane. The σ_1 and σ_2 assisting stress components are also indicated.

order of magnitude of W_0 remains similar and all relationships predict an increasing constriction energy with increasing d_p/b.

The energy required for cross-slip is supplied by the thermal fluctuations occurring in the crystalline lattice. From the thermal activation of cross-slip, it follows that the waiting time for this process, t_{cs}, may be expressed as:

$$t_{cs} = \frac{1}{\nu_0} \exp\left(\frac{W}{kT}\right), \tag{4.3}$$

where ν_0 is the frequency for the crystal vibrations ($\sim 10^{13}$ Hz), k is the Boltzmann's constant and T is the absolute temperature (300 K in this case). Thus, higher values of W correspond to longer waiting times for cross-slip.

The waiting times for cross-slip were calculated from equations (4.1)-(4.3) for five different pure fcc metals (Al, Ni, Cu, Au and Ag). Since the values of the stresses σ_1 and σ_2 are not known, a first approximation was adopted whereby the cross-slip energy was taken as the constriction energy, W_0 (the stresses are assumed to be zero). The resulting calculated values of t_{cs} are represented by the circles in figure 4.8 where the waiting time is plotted as a function of the normalized equilibrium splitting distance, d/b, for dissociated screw dislocations of these five different metals and the dotted horizontal line denotes the estimated time associated with pressing through 16 passes of ECAP (equivalent to $\sim 10^3$ s). Thus, the smallest and largest values of t_{cs} are related to the lowest and the highest degrees of dissociation in Al and Ag, respectively, and for metals having intermediate values of d_p/b (Ni, Cu and Au) the estimated values of t_{cs} lie between the extreme values for Al and Ag.

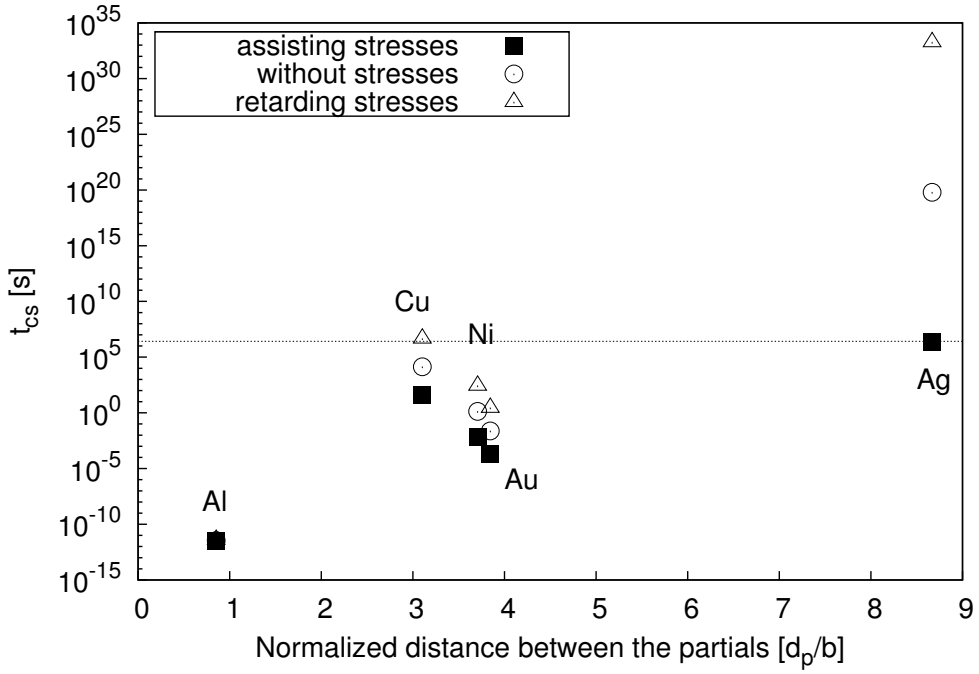

Figure 4.8: The waiting time required for cross-slip of a screw dislocation as a function of the equilibrium splitting distance (d_p) between partials normalized by the Burgers vector, d_p/b, for the situation where cross-slip is either not assisted by stresses or where it is facilitated or hindered by shear stresses having a value of $G/3000$. The dotted horizontal line denotes approximately one month.

Figure 4.8 shows that for Al, Ni, Cu and Au the waiting times for cross-slip are significantly smaller than or close to the total time for processing by ECAP through 16 passes so that the annihilation of the screw dislocations by cross-slip takes place during the ECAP processing operation. By contrast, the waiting time for cross-slip in Ag is of the order of $\sim 10^{19}$ s, equivalent to a waiting period of $\sim 10^{11}$ years, which means in practice that the dislocations formed during ECAP are not annihilated by cross-slip without the benefit of some assisting stresses. However, there is evidence for internal stresses in the microstructures produced by SPD due to the presence of other dislocations and in practice these internal stresses may either assist or hinder the cross-slip process.

The activation energy for cross-slip is sensitive to the presence of these internal stresses. Unfortunately, no internal stress data are available in the literature for severely deformed Ag. At the same time, the residual internal stresses in deformed Cu were measured as $\sim G/3000$ [138]. Taking this value for the assisting stresses, σ_1 and σ_2, the waiting time for cross-slip is significantly reduced for all materials as illustrated by the solid squares in figure 4.8. This decrease in waiting time is most significant for Ag where t_{cs} is reduced to $\sim 2 \times 10^6$ s (equivalent to ~ 1 month). This means, therefore that it is difficult for cross-slip to occur during ECAP of Ag so that a very high dislocation density is

introduced, but at the same time these dislocations may be annihilated several months after processing thereby giving a delayed recovery for the dislocation structure. The present calculation is therefore in agreement with, and provides an explanation for, the experimental data.

In severely deformed polycrystals, the magnitude and direction of the remaining stresses acting on the glide planes after deformation change from grain to grain due to the distributions of the dislocations and other defects, such as twins, so that the probability of cross-slip depends upon their specific locations within the specimen. In some locations in the microstructure the stresses may hinder cross-slip resulting in an increase in the waiting time as illustrated by the triangles in figure 4.8 for a stress value of G/3000. As a result of the stress distributions which are an inherent feature of all deformed materials, it is anticipated that there will be fluctuations in the waiting times for dislocation annihilation.

It is apparent from figure 4.6 that higher dislocation densities after ECAP are associated with faster rates of recovery so that shorter times are then needed to achieve the stable dislocation density during storage at RT. For all ECAP samples, the stable dislocation density is close to the value obtained immediately after 1 pass ($\sim 16 \times 10^{14}$ m^{-2}). For the sample processed by 16 passes, the initial dislocation density is much smaller than for 8 passes so that the recovery occurs more slowly. Furthermore, the higher initial dislocation density corresponds to a shorter mean spacing between dislocations and therefore higher assisting stresses and consequently faster cross-slip. For the sample processed by 1 pass, the assisting stresses are sufficiently low that the microstructure remains reasonably stable within the storage time of 4 months. Considering the factor of 3 between the dislocation densities of the samples processed by 1 and 8 passes, it is estimated that the microstructure of the 1 pass sample has a higher mean spacing between dislocations by a factor of $\sqrt{3}$. As a result, the internal stresses due to dislocations in the sample after 1 pass are lower by a factor of $\sqrt{3}$ than in the sample after 8 passes. Using equation (4.3), it was calculated that this reduction of assisting stresses leads to an increase in the waiting time for cross-slip by several orders of magnitude, thereby explaining the lack of any significant recovery in the 1 pass sample and also the termination in recovery in the samples processed by 4 and 8 passes when the dislocation density reaches the value characteristic for 1 pass. It should be noted that an apparent decrease of the dislocation density in the recovered, but non-recrystallized fraction of the samples may also occur if the recrystallization starts in the volumes having the highest dislocation density.

4.3.2 Annihilation of Dissociated Dislocations by Climb

In addition to the cross-slip of screw dislocations, recovery may occur through the climb of edge dislocations. The climb velocity of an extended dislocation is [139]:

$$v_c = \frac{1050\sigma\Omega D}{bkT} c_j \left(\frac{d_p}{b}\right)^{-2}, \tag{4.4}$$

where σ is the stress acting across the extra half plane of the dislocation producing a climb force $b\sigma$, Ω is the atomic volume, D is the diffusion coefficient and c_j is the number of jogs along the dislocation line. The characteristic waiting time for the annihilation of edge dislocations by climb, t_{climb}, may be approximated as the ratio of the mean spacing between dislocations ($\varrho^{-1/2}$ where ϱ is the average dislocation density) and the climb velocity so that

$$t_{\text{climb}} = \frac{\varrho^{-1/2}}{v_c}. \tag{4.5}$$

It can be established from equation (4.4) that the velocity of climb decreases with an increase in the splitting distance between partials, d_p/b, and therefore dislocation dissociation also hinders annihilation by climb. Equations (4.4) and (4.5) show that the waiting time for climb depends quadratically on d_p/b but for cross-slip the waiting time depends exponentially on the splitting distance which means that cross-slip is more sensitive to an increase in the splitting distance. There is a similar effect for the stress sensitivity of the two mechanisms. For fcc metals having relatively small splitting distances (e.g. Al, Ni, Cu or Au), cross-slip is usually considered to be much faster than climb at RT [55] so that the minimum distance between dislocations, and therefore the maximum dislocation density achieved by ECAP, is determined primarily by the rate of climb. Furthermore since climb is a diffusion-controlled mechanism, it becomes significant only at elevated temperatures where the rates of diffusion are reasonably fast. Nevertheless, experimental evidence suggests that, due to the high volume fraction of grain boundaries and large concentration of dislocations in materials processed by SPD, diffusion may be faster than in coarse-grained specimens by up to several orders of magnitude [140]. This faster diffusion suggests the possibility of a significant role for climb in the annihilation of dislocations even at RT. The velocity of climb is also enhanced by the high concentration of deformation-induced vacancies in SPD-processed materials. Since the diffusion activation energy is proportional to the absolute melting temperature, T_m, in pure fcc metals, the appropriate velocity of climb will depend strongly on T_m and this explains the observed correlation in pure fcc materials between the maximum dislocation density achieved by ECAP at room temperature and the melting temperature [141].

The characteristic waiting time for climb in Ag may be estimated by substituting appropriate values into equations (4.4) and (4.5): $\sigma = G/3000$ which is similar to the value used for cross-slip,

$\Omega/b = 10^{-19}\,\mathrm{m}^2$, $c_j = 1$, $kT = 4 \times 10^{-21}\,\mathrm{J}$, $d_\mathrm{p}/b = 22$ from equation (1.10) for edge dislocations and taking $\varrho = 46 \times 10^{14}\,\mathrm{m}^{-2}$ as the value after 8 passes so that $\varrho^{-1/2} = 15\,\mathrm{nm}$. The value of the diffusion coefficient depends on the migration path of vacancies since D is $\sim 10^{-35}\,\mathrm{m}^2\,\mathrm{s}^{-1}$ [142] in bulk Ag and $\sim 10^{-20}\,\mathrm{m}^2\,\mathrm{s}^{-1}$ along grain boundaries and dislocations [143]. Due to the high dislocation density and small grain size, it is assumed that vacancy diffusion occurs predominantly along dislocations and grain boundaries so that $D \approx 10^{-20}\,\mathrm{m}^2\,\mathrm{s}^{-1}$ and, from equations (4.4) and (4.5), $t_\mathrm{climb} \approx 10^3\,\mathrm{s}$. This value is smaller than the waiting time of $\sim 10^7\,\mathrm{s}$ for cross-slip in Ag so that the very slow cross-slip yields a higher saturation dislocation density ($\sim 46 \times 10^{14}\,\mathrm{m}^{-2}$) than the corresponding values for other fcc metals with similar melting points (e.g. $\sim 17 \times 10^{14}\,\mathrm{m}^{-2}$ in Au [127]). This high dislocation density therefore leads to a large driving force for self-annealing during storage at RT.

4.3.3 The Occurrence of Recrystallization During Self-annealing

The x-ray line profile analysis shows that in the recovered volumes of samples processed through 4-16 passes the dislocation density and the twin boundary probability do not decrease below the value characteristic of the sample pressed through 1 pass (figure 4.6) while the hardness (figure 4.1) and the flow stress (figure 4.2) for the samples processed by 4-16 passes fall below the values obtained for 1 pass after storage for a period of 4 months. This apparent dichotomy is readily explained by the advent of partial recrystallization in the samples processed through 4-16 passes. Indeed, the large intensity spots in the Debye–Scherrer rings (figure 4.5) and the TEM image in figure 4.4a indicate that, in addition to recovery of the dislocation structure, recrystallization also operates during storage at RT after processing by 4-16 passes. Since the activation energy for recovery is smaller than for recrystallization, it is anticipated that recovery will precede recrystallization. As a consequence, and as noted in other reports [144], recovery may diminish the driving force for recrystallization by reducing the dislocation density and/or by decreasing the internal stresses through dislocation rearrangement. In the samples processed by ECAP, recrystallization most probably starts at locations where there is no recovery due to the hindering stresses or where recovery is slow due to low assisting stresses and therefore the driving force remains high during the incubation period of recrystallization. Thus, higher dislocation densities in the non-recovered volumes of the samples will lead to higher driving forces for recrystallization. By increasing the numbers of passes up to 8, the mean dislocation density measured immediately after ECAP is increased and accordingly the rate of recrystallization should be faster after larger numbers of passes.

At the same time, the mean dislocation density measured immediately after 16 passes is smaller than after 8 passes and after 4 months the reductions in hardness and flow stress are the highest for

the sample processed by 16 passes. This is attributed to the higher degree of recrystallization in this sample. As shown in section 3.1, processing by ECAP between 8 and 16 passes gives an increase in the twin boundary probability together with a decrease in the total dislocation density. In locations where the twin boundary probability increases at the expense of dislocations, the stored energy will decrease as the twin fault energy in Ag is very low ($\sim 8\,\mathrm{mJ\,m^{-2}}$ [58]). Recrystallization may be promoted after 16 passes by the formation of small volumes where the stored energy is much lower than in the neighboring region due to the reduced dislocation/twin boundary density ratio. These volumes will then act as the embryos for the new grains formed by recrystallization and therefore the time required for grain nucleation will be the shortest for the sample processed by 16 passes. Since in this case the strongly twinned regions are recrystallized first, it follows that there will be a decrease in the twin density in the recovered, but non-recrystallized volumes for the sample processed by 16 passes, which is in line with the results of x-ray line profile analysis. This is consistent with the observations that the nuclei of recrystallized grains form primarily at deformation twins in low stacking fault energy metals such as Ag [145].

The formation of regions where twinning occurs at the expense of dislocations will increase the degree of inhomogeneity in the microstructure and introduce fluctuations in the stored energy in the sample processed by 16 passes. This is consistent with other studies suggesting that heterogeneities in the microstructure may promote recrystallization due to the higher strain energy gradients [100, 146]. It is noted that the high grain boundary energy may also contribute to the driving force for recrystallization in the samples processed by 4-16 passes as the grain size in these materials is smaller ($\sim 200\,\mathrm{nm}$) than in the sample processed by only 1 pass ($\sim 5\,\mu\mathrm{m}$). A recent study of annealing in Cu processed by ECAP showed that recrystallization starts heterogeneously primarily in regions where grain boundaries have high angles of misorientation [147]. Since the angle of misorientation at grain boundaries usually increases with increasing numbers of passes in ECAP [148, 149], it is reasonable to anticipate that recrystallization in Ag will be faster after larger numbers of passes. Twins can also be regarded as high angle boundaries, therefore the increase of twin boundary density with increasing number of passes may also contribute to faster recrystallization. It is important to note also that impurities have a strong influence on the occurrence of recrystallization during self-annealing. For example, recrystallization was observed in very high-purity (5N) Al even during processing by ECAP at RT [150] which explains the lack of any reports of self-annealing in very high-purity Al.

It is noted that self-annealing was also observed previously in ECAP-processed Cu at RT [85, 100]. For a similar impurity concentration, the self-annealing in Ag starts earlier (~ 1 month) than in Cu (~ 8 years [85]). As the minimum grain sizes achieved during ECAP are similar ($\sim 200\,\mathrm{nm}$) for both Ag and Cu, the grain boundary energy most probably makes a similar contribution to the driving force for recrystallization in the two materials. At the same time, the lower SFE in Ag is associated with a

lower twin fault energy which facilitates the formation of recrystallized embryos. The nuclei formed during recrystallization are usually separated by twins from the parent grains. Therefore, the lower value of the SFE in Ag leads to an easier nucleation of the recrystallized grains which also contributes to faster self-annealing in Ag.

In this chapter the room temperature thermal stability of ECAP processed pure silver samples have been investigated. It has been shown that the evolved microstructure (the dislocation density and the twin fault probability) and indirectly the impurity level has a very significant effect on the thermal stability of the samples. Finally, an important additional consideration is that the reduced stability of ultrafine-grained microstructures in low SFE metals may affect the viability of these materials for use as structural components. To avoid problems associated with self-annealing, the present research suggests the need to use an optimum and relatively low total strain when applying SPD-processing to pure, low SFE metals.

Chapter 5

Thermal Stability of ECAP-processed Silver at Elevated Temperatures [R8, R9]

Now the high temperature thermal stability of the silver samples processed by ECAP will be investigated. Differential scanning calorimetry was used to study the occurrence of recovery and recrystallization and also the amount of released heat, the latter was defined as the area under the exothermic calorimetric peaks.

5.1 DSC Study of Silver Processed by Different Numbers of ECAP Passes

The thermal stability at elevated temperatures was investigated in an Ar atmosphere by DSC using a Perkin Elmer (DSC2) calorimeter with a heating rate of 10 K/min. The heat released during annealing was determined as the area under the exothermic peak detected in DSC experiments as was already mentioned in subsection 2.4.

Figure 5.1 shows the DSC thermograms measured at a heating rate of 10 K/min for both 4N5 and 4N purity Ag samples processed by ECAP. An exothermic peak was observed for each sample that corresponds to the recovery and recrystallization of the UFG microstructure. The maximum of the peaks and the released heat during the scan are plotted in figure 5.2 as a function of the number of passes for both compositions. It can be concluded that the temperature of recovery/recrystallization is much smaller for 4-16 passes than for 1 pass for both series due to the smaller grain size and the higher defect density that give a larger driving force for annealing processes. For each number of passes the temperature of peak maximum is higher while the released heat is lower for the 4N purity sample than for the 4N5 purity counterpart. This can be explained by the hindering effect of impurities on recovery and recrystallization. It is noted that in the case of 4N5 purity Ag, the high-temperature stability of the sample processed by 16 passes is better than that for the specimens processed by 4 or 8 passes, while the self-annealing at RT was the fastest for the former sample, as shown in the previous chapter. This can be explained by the large number of recrystallization nuclei formed at high temperatures that suppress the role of the twinned volumes developed during processing by 16 passes of ECAP.

It is obvious that both the temperature of the peak maximum and the released heat show a saturation for both compositions. This result is in very good agreement with previous investigations carried

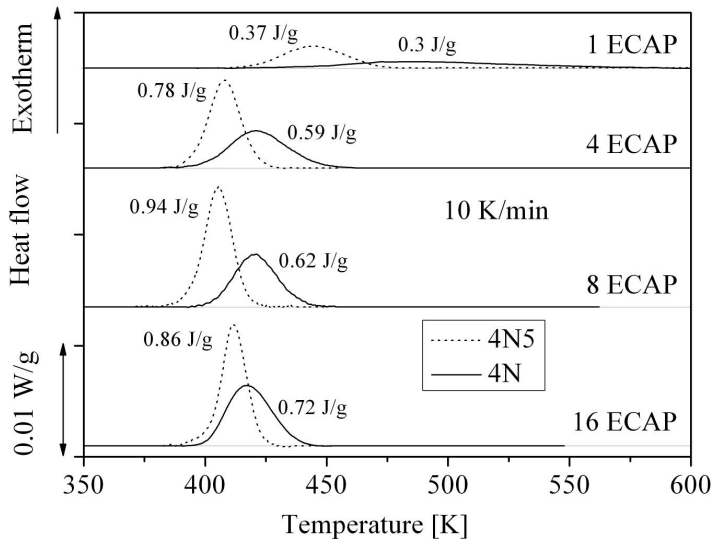

Figure 5.1: DSC thermograms obtained at a heating rate of 10 K/min for 4N5 (dashed line) and 4N (solid line) purity Ag processed by different numbers of passes. The values at the exothermic peaks represent the released heat.

out on copper processed by ECAP [89, 96].

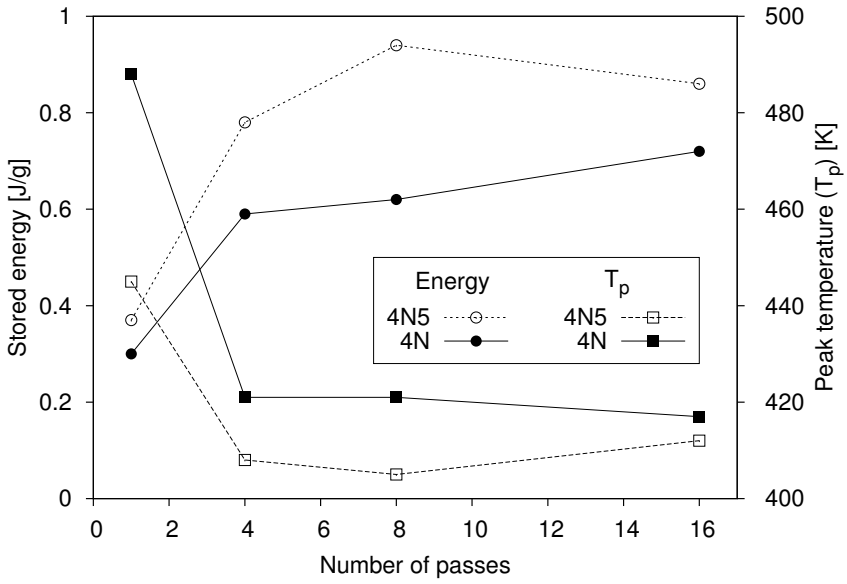

Figure 5.2: The stored energies and the position of the peaks (T_p) as a function of the number of ECAP passes.

5.2 Detailed Investigation of the Samples Processed by Four Passes of ECAP

After 4 passes the dislocation density was $37 \pm 4 \times 10^{14}\,\mathrm{m}^{-2}$ and $41 \pm 5 \times 10^{14}\,\mathrm{m}^{-2}$ while the twin boundary probability was $0.7 \pm 0.1\%$ and $0.8 \pm 0.1\%$ for the 4N5 and the 4N samples after 4 passes of ECAP, respectively (see figure 3.4), implying very similar microstructures. This microstructural similarity was confirmed by microscopy investigations. Bright-field TEM images taken after the ECAP process are shown in figure 5.3a and b for 4N5 and 4N purity Ag samples, respectively.

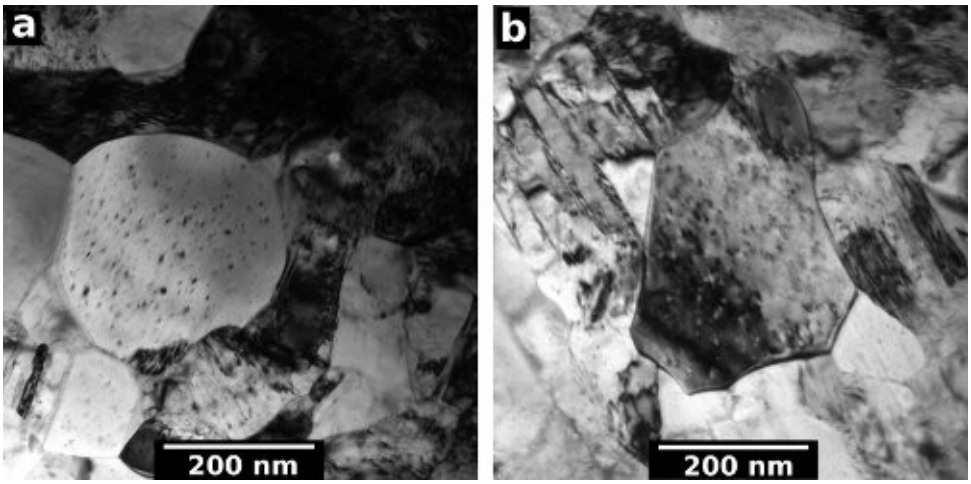

Figure 5.3: Bright-field TEM images showing the similarity of microstructures immediately after ECAP-processing by 4 passes for (a) the 4N5 and (b) the 4N purity samples.

There is a significant difference between the thermal stabilities of the 4N5 and 4N purity specimens as observed from the positions of the DSC peaks (see figure 5.1). Specifically, the maximum of the exothermic peaks for the 4N5 and 4N samples appear at 408 and 421 K, respectively. The higher stability of the less pure sample is attributed to the pinning effect of the impurity atoms on lattice defects (dislocations and grain boundaries).

The DSC experiments were carried out at different heating rates, as shown in figure 5.1. The activation energy of recovery/recrystallization was determined from the shift of the DSC peak maximum due to a change in the heating rate, using by the conventional Kissinger-analysis [119]:

$$\ln \frac{\zeta}{T_\mathrm{p}^2} = -\frac{Q}{kT_\mathrm{p}} + A, \tag{5.1}$$

where ζ is the heating rate, T_p is the peak temperature, Q is the activation energy, k is the Boltzmann constant, and A is a constant. The Kissinger plots (see the insets in figure 5.4) based on equation

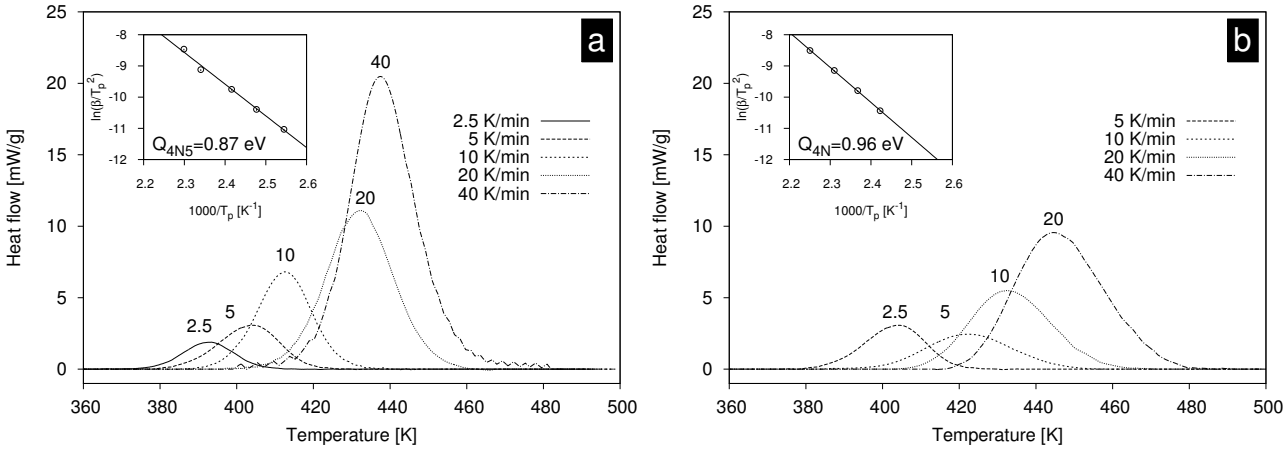

Figure 5.4: DSC curves obtained at different heating rates (also indicated by the numbers at the peaks) for the 4N5 (a) and for the 4N (b) samples processed by 4 passes of ECAP. The insets show the Kissinger plots which give the activation energy of recrystallization.

(5.1) gave 0.87 ± 0.04 and 0.96 ± 0.05 eV for the activation energies of recovery/recrystallization in 4N5 and 4N purity specimens, respectively[1]. These values are about one-half of the activation energy of self-diffusion in Ag (1.76 eV [152]) and thus they are similar to other fcc metals processed by SPD [83, 86, 89–93, 95, 96]. As the activation energy of diffusion along grain boundaries and dislocations is also about one-half of the value for self-diffusion [97–99], therefore the observed values of activation energy of recovery/recrystallization in UFG materials can be explained by the large density of dislocations and grain boundaries acting as diffusion paths during annealing.

It is apparent from figure 5.1 that not only the temperature of the peak maximum, but also the shape of the DSC peak is significantly affected by the impurity content. For the 4N purity sample, the maximum heat flow is smaller and the peak is wider than for the 4N5 purity specimen. In addition, the heat released in the DSC peak obtained with 10 K/min heating rate is significantly smaller for the 4N purity sample (0.59 ± 0.04 J/g) than for the 4N5 specimen (0.78 ± 0.05 J/g). In order to reveal the origin of the difference in the released heat, a detailed study of the microstructures was undertaken after the DSC peaks for both impurity levels.

Figure 5.5 shows EBSD orientation images and the corresponding image quality (IQ) maps taken on 4N5 and 4N samples annealed up to the end of the exothermic DSC peak. Most of the grains are larger than several microns and have straight boundaries, as it is usual in recrystallized volumes. However, some remaining UFG regions with an average grain size of $\sim 300 - 700$ nm are visible for both purity levels as indicated by the white arrows in figure 5.5b and d. From a comparison of several

[1]It should be noted that the method proposed by Chen and Spaepen [151] for the determination of the activation energy gives the same result within less than 4% uncertainty.

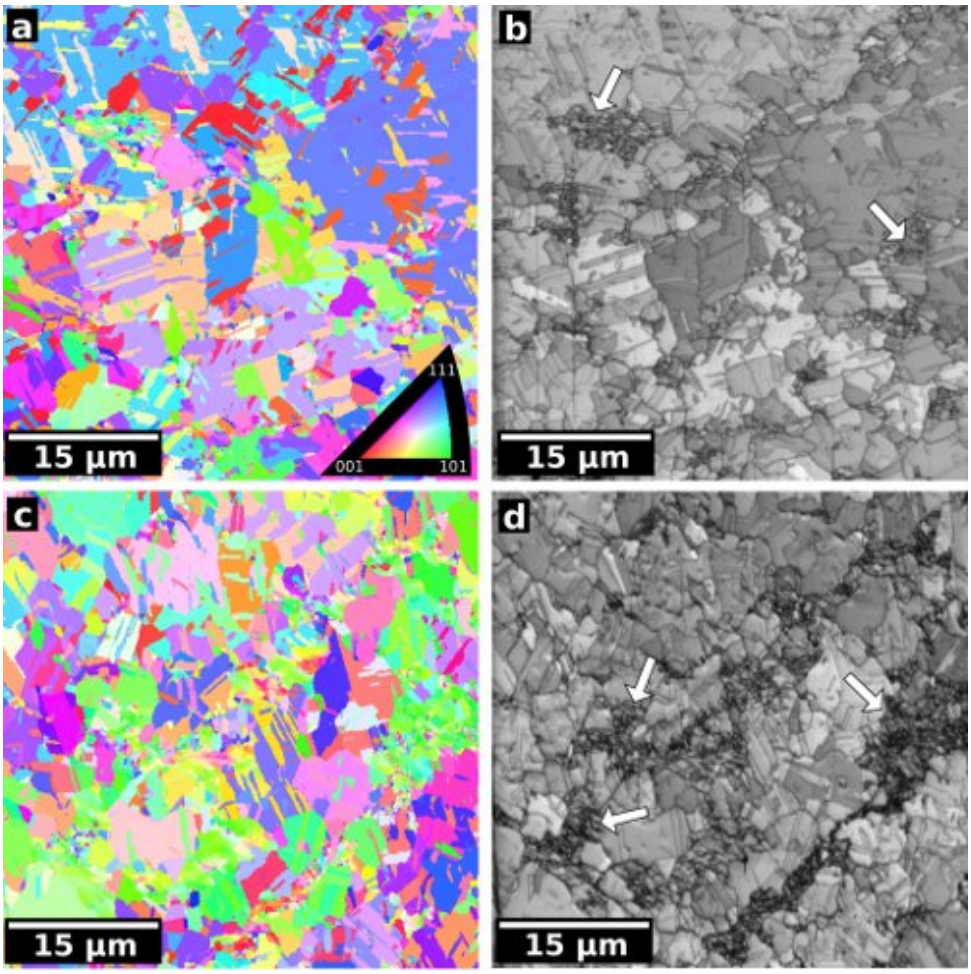

Figure 5.5: EBSD images showing the orientation distributions of grains in (a) the 4N5 and (c) the 4N purity samples annealed in DSC up to the end of the exothermic peak. The image quality pictures for the same areas show the grain boundaries in (b) the 4N5 and (d) the 4N purity samples. The remaining UFG regions are indicated by white arrows.

IQ maps obtained for the two impurity concentrations, the fraction of these UFG regions was slightly larger in the 4N purity sample (17%) than in the 4N5 specimen (10%) and this can be attributed to the pinning effect of impurities on the grain boundaries during recrystallization.

The misorientation angle distribution after the DSC peak was determined from the EBSD images and plotted in figure 5.6. For both annealed samples, the angle of misorientation is $60°$ for the majority of boundaries which indicate that they are $\Sigma 3$ coincidence site lattice (CSL) boundaries. These boundaries are most probably coherent twin boundaries formed during recrystallization. The fraction of low-angle grain boundaries with angles of misorientation below $15°$ was larger for the 4N purity specimen (12%) than for the 4N5 sample (7.3%). This difference is associated with the slightly larger

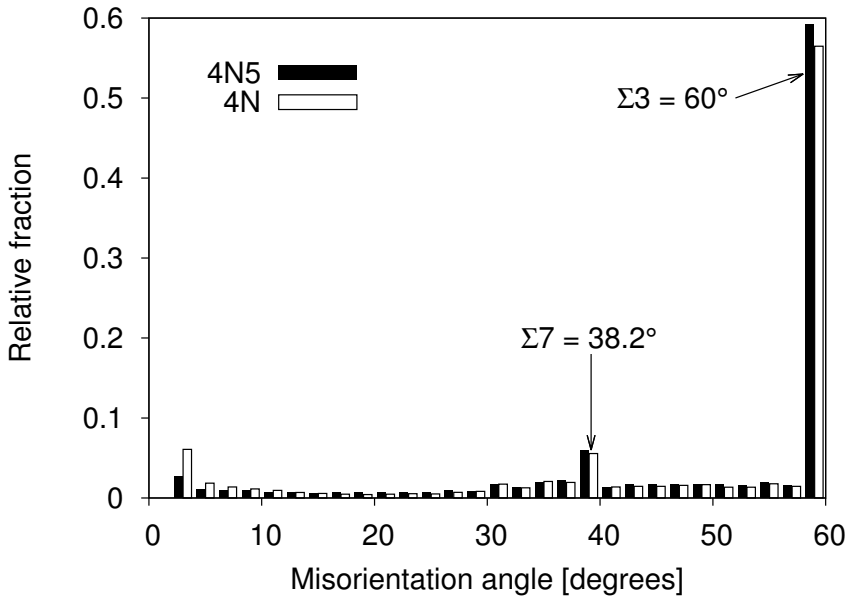

Figure 5.6: Grain-boundary misorientation distributions for 4N5 and 4N purity samples ECAP-processed and then annealed in DSC up to the end of the exothermic peak. The peaks corresponding to $\Sigma 7$ and $\Sigma 3$ boundaries in the histogram are indicated.

UFG fraction in the less pure material since the boundaries with small misorientations were found in these regions.

XLPA investigations were also carried out just before and after the DSC peak. It was found that during annealing up to the beginning of the exothermic peak the dislocation density decreased only by $\sim 10-20\%$ from $37 \pm 4 \times 10^{14}\,\mathrm{m}^{-2}$ and $41 \pm 5 \times 10^{14}\,\mathrm{m}^{-2}$ to $32 \pm 4 \times 10^{14}\,\mathrm{m}^{-2}$ for 4N5 and 4N samples, respectively. After the DSC peak, the values of both the dislocation density and the twin-boundary frequency were lower than the detection limits of XLPA ($10^{13}\,\mathrm{m}^{-2}$ and 0.05%, respectively), indicating that for both impurity levels the majority of dislocations were annihilated in the temperature range corresponding to the DSC peak. It is noted that if dislocation loops having a size of several nanometers remain in the microstructure after recovery/recrystallization, they are also invisible by XLPA due to their strongly shielded strain fields. The smaller released heat for the 4N purity sample is partly attributed to the larger remaining UFG fraction after the DSC peak, but it may be due to the higher concentration of vacancies, vacancy clusters or small dislocation loops remaining in the recrystallized grains due to the pinning effect of impurities. These defects are undetectable by either EBSD or XLPA and require additional studies by TEM and PAS.

Figures 5.7a and b show TEM images for the interiors of recrystallized grains in 4N5 and 4N purity samples annealed up to the end of the DSC peak. Careful inspection of the images[2] using the extinc-

[2]According to the extinction rule a dislocation gives only a very weak or invisible contrast if $\mathbf{gb} = 0$, where $\mathbf{b}$ is

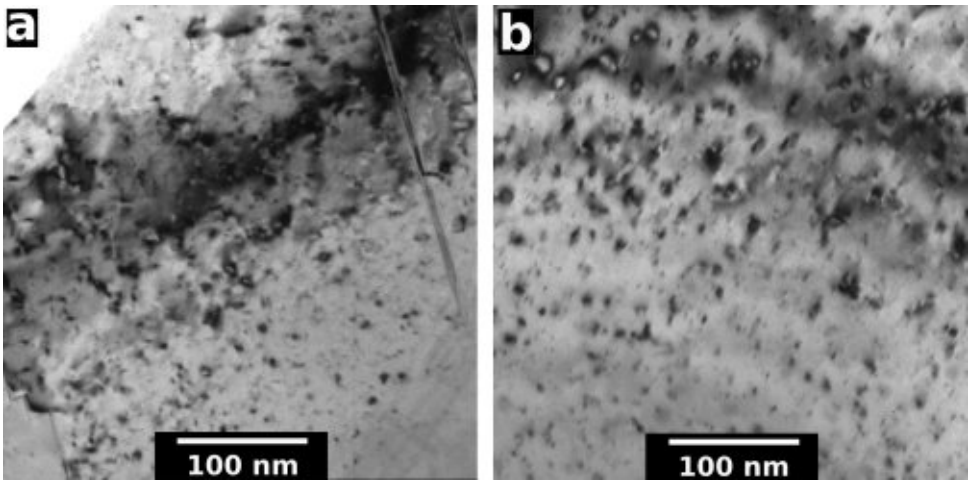

Figure 5.7: TEM images showing the recrystallized microstructures for (a) the 4N5 and (b) the 4N purity samples after heat treatment in DSC up to the end of the exothermic peak.

tion rule for dislocations showed that the dark spots are dislocation loops having Burgers vectors of $1/2\langle 110\rangle$ or $1/3\langle 111\rangle$. The numbers of the investigated loops in the 4N5 and 4N purity specimens were 51 and 101, respectively. In 4N5 purity Ag, the relative fractions of dislocations with Burgers vectors of $1/2\langle 110\rangle$ and $1/3\langle 111\rangle$ were 81 and 19%, respectively, and for 4N purity these fractions were 72 and 28%, respectively. Dislocations with Burgers vectors of $1/3\langle 111\rangle$ are sessile Frank-loops which bound 2D vacancy agglomerates on $\{111\}$ planes. Clustering of vacancies into 2D configurations on $\{111\}$ planes is energetically more favorable in Ag than in other fcc metals due to the low SFE. The diameters of the dislocation loops are between 3 and 14 nm (the average diameter is ~ 7 nm), irrespective of their Burgers vectors and the purity level. The volume density of the dislocation loops was about $8 \pm 2 \times 10^{22}\,\mathrm{m}^{-3}$ for both impurity concentrations.

The present TEM observations reveal that after the DSC peak a considerable number of dislocation loops remain in the material even in the recrystallized volumes. It is noted that dark spots are also observed inside the grains immediately after ECAP (see figures 5.3a and b). These spots probably also correspond to dislocation loops which are formed during four passes of ECAP. However, an evaluation of these types of loops in the TEM images was unsuccessful due to the highly distorted microstructures. The density of loops after ECAP was similar to the density after the DSC peak, but their size was slightly smaller.

The change of vacancy concentration during the evolution of the exothermic DSC peak was investigated by PAS. The experimental lifetimes of positrons annihilated at defects in both 4N5 and 4N

the Burgers-vector of the dislocation and $\mathbf{g}$ is the diffraction vector. Hence using multiple images obtained at different two-beam conditions, the type of the Burgers-vector of a dislocation can be determined.

purity samples before and after the DSC peak are between 181 and 201 ps. These values are close to the positron lifetime of mono-vacancies in plastically deformed Ag (196 ps, [122]). However, even at the beginning of the exothermic peak, at ~ 380 K, the temperature is too high for mono-vacancies to exist. If the vacancies agglomerate into 3D clusters, the positron lifetime would be much higher than the value for a mono-vacancy. The absence of 3D vacancy agglomerates can be attributed to the low SFE of Ag because, even if they formed, their collapse into 2D clusters is energetically favorable [153].

In Ag, the 2D vacancy clusters usually form on $\{111\}$ planes and these agglomerates may be regarded as a stacking fault bordered by a Frank dislocation loop with a Burgers vector of $1/3\,\langle 111\rangle$. The lifetime of positrons annihilated at these 2D clusters is only slightly smaller than the value for mono-vacancies [154, 155]. The positron lifetime for free volumes of approximately the size of a mono-vacancy in the grain boundaries is also close to the value characteristic for mono-vacancies [156]. Therefore, it is expected that the concentration obtained by PAS describes vacancies in 2D collapsed clusters and grain boundaries.

At the beginning of the exothermic peak, at ~ 380 K, the vacancy concentration in 4N5 purity sample was larger than the detection limit in the PAS experiments ($\sim 5 \times 10^{-5}$) while for the 4N specimen the value was determined as $0.8 \pm 0.1 \times 10^{-5}$. The considerably smaller vacancy concentration in the 4N sample compared to the 4N5 specimen can be explained by the segregation of impurity atoms at the grain interfaces (see figure 5.8) which make small free volumes in the boundaries invisible for positrons.

During the evolution of the DSC peak, the vacancy concentration decreased from a value higher than 5×10^{-5} to $0.7 \pm 0.1 \times 10^{-5}$ in the 4N5 specimen while in the 4N sample the vacancy concentration increased from $0.8 \pm 0.1 \times 10^{-5}$ to $1.5 \pm 0.1 \times 10^{-5}$. This increase in vacancy concentration is due to the release of the free volumes in the grain boundaries into the lattice in the form of vacancies during recrystallization [157–159]. Therefore, the former small interface free volumes became detectable for positrons, resulting in an increase in the measured vacancy concentration. Similar vacancy production most probably also occurs in the 4N5 purity sample, but all of these vacancies were annihilated before the end of the DSC peak. At the same time, in the 4N specimen a fraction of the vacancies formed during recrystallization was trapped in the microstructure due to the pinning effect of large impurities (Pb, Sb, and Bi), as shown in earlier observations [160].

5.3 Comparison of the Measured and the Calculated Released Heat Values

The values of the released heat measured by DSC for the 4N5 and 4N purity samples with the difference between the stored energies calculated before and after the DSC peak were compared. The stored

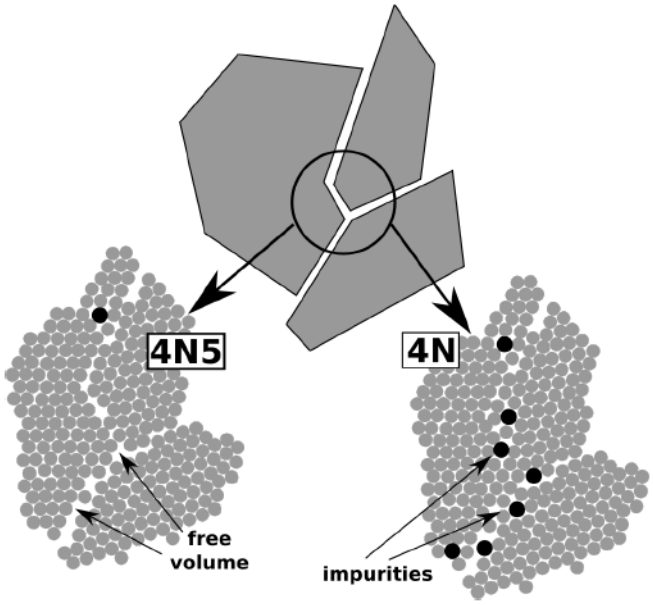

Figure 5.8: Schematic illustraton of the larger free volume at grain boundaries; comparison of the 4N and the 4N5 samples.

energy per unit mass in the two ECAP-processed UFG Ag samples before and after the DSC peak was determined as the sum of the energies of the lattice defects (grain boundaries, dislocations, twin faults, small dislocation loops, and vacancies) investigated in the previous sections. It is noted that the values of the calculated energies are rounded to the precision of the measured released heat which corresponds to two decimal places.

The energy stored in dislocations (E_{disl}) can be determined from the dislocation density using the following relationship [52]:

$$E_{\mathrm{disl}} = A\frac{Gb^2\varrho}{\varrho_{\mathrm{m}}}\ln\frac{1}{b\sqrt{\varrho}}, \tag{5.2}$$

where G is the shear modulus (30 GPa), b is the magnitude of Burgers vector (0.29 nm), ϱ is the dislocation density, ϱ_{m} is the mass density of silver (taken as $10.49 \times 10^3\,\mathrm{kg/m^3}$), and A denotes a factor which depends on the edge/screw character of the dislocations. The value of A is equal to $(4\pi)^{-1}$ and $(4\pi(1-\nu))^{-1}$ for screw and edge dislocations, respectively, where ν is Poisson's ratio (taken as 0.3).

The parameter q determined from x-ray line-profile analysis describes the edge/screw character of the dislocations. The theoretically calculated values of q for pure edge and screw dislocations in Ag are 1.62 and 2.35, respectively. In practice, the value of A was obtained from the experimentally determined q of 2.2 using a simple rule of mixtures [49, 53]:

$$A = \frac{q-1.62}{0.73}\frac{1}{4\pi} + \frac{2.35-q}{0.73}\frac{1}{4\pi(1-\nu)}. \tag{5.3}$$

The energy stored in dislocations calculated from the dislocation density determined by XLPA is $0.28\,\mathrm{J/g}$ for both samples before the DSC peak. After this peak in the recrystallized region, the dislocation density was smaller than the detection limit of XLPA ($10^{13}\,\mathrm{m}^{-2}$) which is two orders of magnitude lower than the value determined before the DSC peak. Therefore, this contribution to the stored energy may be neglected. In the remaining UFG region, the dislocation density is most probably higher than the detection limit, but its value is not easily determined by XLPA due to the relatively small volume fraction of this region. Therefore, an upper limit of E_{disl} in the remaining UFG region was calculated as the product of the dislocation density before the DSC peak and the fraction of the UFG volumes: thus, 0.02 and $0.04\,\mathrm{J/g}$ were obtained for the 4N5 and 4N purity samples, respectively. The calculated values of the stored energy are summarized in table 5.1.

The interfaces between the grains can be classified as low- and high-angle grain boundaries (LAGBs and HAGBs, respectively). The LAGBs usually consist of dislocations and XLPA measures dislocations in both the boundaries and the interiors of the grains so that the contribution of LAGBs to the stored energy is incorporated in equation (5.2). The energy of the HAGBs (E_{HAGB}) is given as [161]:

$$E_{\mathrm{HAGB}} = h\frac{3\gamma_{\mathrm{GB}}}{d\varrho_{\mathrm{m}}}, \tag{5.4}$$

where γ_{GB} is the average HAGB energy in Ag ($0.5\,\mathrm{J\,m^{-2}}$ [162]), h is the fraction of HAGBs (about 0.5 for fcc metals processed by four passes of ECAP [148]) and d is the average grain size. Before the DSC peak, the average grain size in both samples is $200\,\mathrm{nm}$ which gives $0.36\,\mathrm{J/g}$ for the grain boundary energy. It is noted that in the less pure material the segregation of large atoms to grain boundaries reduces the grain boundary energy [163]. However, taking into account the total concentration of large dopants in 4N purity sample ($c_{\mathrm{d}} = 4\times10^{-5}$ for Pb, Sb, and Bi), the reduction in grain boundary energy is negligibly small at about 2% [163]. After the DSC peak, the microstructure for both purity levels consists of recrystallized coarse-grains and the remaining UFG regions with average grain sizes of $5\,\mu\mathrm{m}$ and $500\,\mathrm{nm}$, respectively. The energy stored in HAGBs in the recrystallized fraction is negligible since, as shown in figure 5.6, most of them are twin boundaries having very low energy ($0.008\,\mathrm{J\,m^{-2}}$ [58]). Taking into account the relative fraction of the remaining UFG regions, the energies stored in the HAGBs after the DSC peak are ~0.01 and $\sim0.02\,\mathrm{J/g}$ for the 4N5 and 4N purity samples, respectively.

For the calculation of the stored energy contributions of twin faults investigated by XLPA, the grains were modelled by cubes with the edge length d. The energy of a twin fault lying parallel to a cube face is $\gamma_{\mathrm{twin}}d^2$, where γ_{twin} is the twin boundary energy in Ag. The number of parallel twin faults can be expressed as d/d_{twin}, where d_{twin} is the mean twin boundary spacing. Then, the stored energy for twin faults (E_{twin}) in cubic grains can be calculated as:

$$E_{\mathrm{twin}} = \gamma_{\mathrm{twin}}d^2\frac{d}{d_{\mathrm{twin}}}\frac{1}{d^3\varrho_{\mathrm{m}}} = \frac{\gamma_{\mathrm{twin}}\beta}{d_{111}\varrho_{\mathrm{m}}}, \tag{5.5}$$

where $d^3\varrho_m$ is the mass of the cubic grain, β is the twin-boundary frequency determined by XLPA ($0.7\pm0.1\%$ before the DSC peak for both impurity levels), d_{111} is the spacing between the neighboring $\{111\}$ planes (0.24 nm) and d_{twin} can be expressed as d_{111}/β. The value of E_{twin} is ~ 0.02 J/g for both 4N5 and 4N specimens before the DSC peak and practically zero after the peak due to the very large mean twin-boundary spacing ($> 1\,\mu$m).

The stored energy for the small dislocation loops (E_{loop}) with Burgers vector of $1/2\,\langle 110\rangle$ in the recrystallized fraction after the DSC peak may be expressed by modifying equation (5.2) and (5.3) as:

$$E_{loop} = g\frac{1}{8\pi}\left(1+\frac{1}{1-\nu}\right)\frac{Gb^2 f\varrho_{loop}}{\varrho_m}\ln\frac{D}{b}, \tag{5.6}$$

where g is the recrystallized volume fraction. The outer cut-off radius of dislocations in the loops was selected as the average diameter of the loops ($D = 7$ nm as determined by TEM) and ϱ_{loop} is the total length of dislocations in the loops in a unit volume (i.e. the dislocation density in the loops with both Burgers vectors) and f is the fraction of dislocation loops with Burgers vector of $1/2\,\langle 110\rangle$. The value of ϱ_{loop} was determined as the product of the average length of a loop ($D\pi$) and the volume density of the dislocation loops ($r_{loop} = 8\times10^{22}$ m^{-3}). Calculating the energies stored in the loops after the DSC peak using equation (5.6), values of ~ 0.09 J/g were obtained for both samples. As the density and the size of the dislocation loops immediately after ECAP appears to similar to the values after the DSC peak, the same stored energies were assumed for the loops both before and after the DSC peak. This means that the loops make a negligible contribution to the released heat despite their high density. The loops with Burgers vector of $1/3\,\langle 111\rangle$ are practically collapsed vacancy clusters, therefore their stored energy is included in the energy calculated from the vacancy concentration in the next paragraph.

The energy stored in the vacancies (E_{vac}) may be expressed by the measured vacancy concentration (c_v) as [52]:

$$E_{vac} = e_v c_v \frac{N_A}{M}, \tag{5.7}$$

where e_v is the formation energy of a vacancy (1.1 eV $= 0.176\times10^{-18}$ J [164, 165]), N_A is Avogadro's number (6×10^{23} mol^{-1}) and M is the molar mass (107.87 g/mol). The values of E_{vac} were determined from the vacancy concentrations measured by PAS and listed in table 5.1. It is noted that the segregation of the large dopants to vacancies with a maximum binding energy of ~ 0.3 eV [166] may reduce the vacancy energy by 30% which is negligible by comparison with other contributions.

Summing up the stored energies calculated for the different lattice defects, the total energies stored in the 4N5 and 4N purity specimens before and after the DSC peak are listed in table 5.1. These calculations show that the largest contributions to the stored energy before the DSC peak are given by dislocations and HAGBs. After the DSC peak, about $15-20\%$ of the stored energy is retained in the material due to the remaining UFG fraction and the dislocation loops in the recrystallized volumes.

Table 5.1: The difference between the stored energies determined before and after the peak is used to estimate the contributions of the various lattice defects to the heat released in the exothermic DSC peak. E_{disl}, dislocations; E_{HAGB}, high-angle grain boundaries; E_{twin}, twin boundaries; E_{loop}, small dislocation loops; E_{vac}, vacancies. 'Exp.' denotes the experimental value.

	4N5			4N		
	Before the DSC peak	After the DSC peak	Difference	Before the DSC peak	After the DSC peak	Difference
E_{disl} [J/g]	0.28	$0 - 0.02$	$0.26 - 0.28$	0.28	$0 - 0.04$	$0.24 - 0.28$
E_{HAGB} [J/g]	0.36	0.01	0.35	0.36	0.02	0.34
E_{twin} [J/g]	0.02	0	0.02	0.02	0	0.02
E_{loop} [J/g]	0.09	0.09	0	0.09	0.09	0
E_{vac} [J/g]	≥ 0.05	0.01	≥ 0.04	0.01	0.01	0
Sum [J/g]	≥ 0.80	$0.11 - 0.13$	$\geq 0.67 - 0.69$	0.76	$0.12 - 0.16$	$0.60 - 0.64$
Exp. [J/g]			0.78			0.59

The difference between the total energies obtained before and after the DSC peak gives the calculated released heat. For the 4N purity sample the measured heat (0.59 ± 0.04 J/g) and its calculated value ($0.60 - 0.64$ J/g) agree within the experimental error. For the 4N5 purity sample only a lower bound for the released heat can be calculated since the vacancy concentration was larger than the detection limit of PAS. In this case, the calculated value of the released heat is larger than $0.67 - 0.69$ J/g which is in accordance with the experimentally measured value of 0.78 ± 0.04 J/g. Assuming an agreement between the calculated and the measured values of the heat release for the 4N5 purity specimen, the vacancy concentration before the DSC peak can be determined from equation (5.7) as $\sim 1.5 \times 10^{-4}$. This means that the much lower heat released for the 4N purity sample compared to the 4N5 purity specimen is mainly attributed to an order of magnitude smaller vacancy concentration. It is emphasized that the vacancy concentration obtained by PAS includes also the free volumes in the grain boundaries. The segregation of impurities to these boundaries reduces the measured vacancy concentration in the 4N purity sample.

It should be noted that the degree of impurity segregation to grain boundaries depends not only on the concentration, but also on the type of dopants. The preference of a solute to dissolve either in an ordered crystal lattice or in a disordered grain boundary is characterized by the distribution coefficient, k [167]. For a dilute binary alloy, this quantity is defined as the ratio of the concentrations in the solid and the liquid phases under equilibrium conditions where the liquid phase corresponds to

the disordered phase. For a solute-solvent atom pair, if $k > 1$ or $k < 1$ the solute prefers either an ordered or a disordered environment, respectively. This preference depends on the ratio of the radii of the solute and solvent atoms, on the difference between their electronegativities and their valence numbers [166]. Among the impurities found in the silver materials used in this investigation, the dopants Cu, Sb, Se, Pb, and Bi have $k < 1$ [167–170]. In the 4N purity sample the concentration sum for these elements is 80 ppm and this is much higher than the concentration of 33 ppm for the 4N5 specimen although both impurity contents are very low. However, it was shown for rolled Cu-Ag alloys, where Ag solute in Cu has $k < 1$, that only 80 ppm Ag leads to a 30% reduction in the released heat compared to Cu with a Ag concentration of $30 - 40$ ppm [167]. The present results show a similar effect of impurities in Ag, thereby demonstrating that a very small difference in the impurity level produces a significant variation in the heat released during annealing.

Summarizing the results of this chapter, it was found that the exothermic DSC peaks for 4N purity samples appeared at higher temperatures and the released heat values were smaller than in the case of 4N5 purity specimens. However, the activation energies for recovery and recrystallization are similar for both materials at least after 4 passes of ECAP. The primary contributions to the stored energy before recovery/recrystallization are given by the grain boundaries and dislocations. A significant fraction of stored energy ($\sim 15 - 20\%$) was retained in the samples after the exothermic DSC peak due to the remaining UFG regions and the high density of small dislocation loops. The reduced heat released for the 4N purity sample is primarily due to the lower vacancy concentration before the DSC peak compared to the 4N5 purity specimen. This phenomenon is attributed to a reduction of free volumes by segregation of dopants at the grain interfaces.

Chapter 6

Defect Structure and its Thermal Stability in Silver Processed by High-pressure Torsion [R4, R10, R11]

In the previous three chapters the evolution of the microstructure during ECAP processing of silver samples with different impurity levels, as well as their room and high temperature stability were investigated in details. Besides ECAP there are other SPD methods for producing UFG microstructures. HPT is another very commonly used SPD technique even though the size of an HPT processed specimen is very limited. In this chapter, HPT processed pure silver samples will be investigated in order to compare the microstructure obtained by this technique with that produced by ECAP. Due to the very weak thermal stability of the HPT-processed 4N5 purity silver samples, the UFG microstructure was self-annealed between HPT and the analysis of the microstructure[1]. Therefore, only the results for the 4N samples will be presented here.

6.1 Microstructure After High-pressure Torsion

1, 10 and 20 turns of HPT were applied on cylinders ~ 10 mm in diameter and ~ 0.8 mm in thickness. The applied pressure was 6 GPa and the deformation was carried out at RT with a rotation rate of 1 rpm. The two anvils of the HPT device have shallow central depressions on their outer surfaces, with depths of ~ 0.25 mm and diameters of 10 mm at the bottom, and with slightly inclined walls having outer inclinations of 22°, as shown in figure 6.1. The thickness of the HPT-processed samples was 0.65 mm after releasing the applied pressure.

The microstructures of the HPT-processed disks were investigated close to the center, at the half radius and the periphery by x-ray line profile analysis[2]. The dislocation density and the twin boundary frequency are plotted in figure 6.2a as a function of the distance from the center of the disks. The dimensions of the area illuminated by x-rays were 0.3 and 1.5 mm parallel and perpendicular to the disk radius, respectively. This is reflected by the horizontal error bars of the datum points in figure

[1] HPT was performed in USA, while XLPA was carried out in Hungary.

[2] It should be noted that the HPT-processed Ag samples had a moderate {111} texture, as usually in the specimens processed by HPT [40]. However, this texture did not require to modify the evaluation procedure of the line profiles, since due to the severe deformation most probably all slip systems are equally populated by dislocations

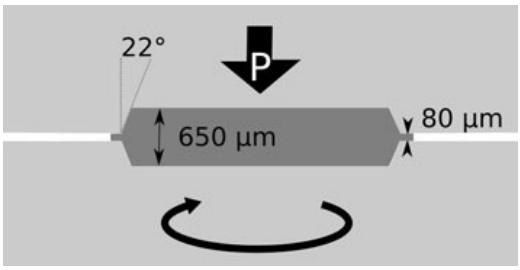

Figure 6.1: Schematic illustration of the geometry of the anvils and the workpiece used in HPT-processing.

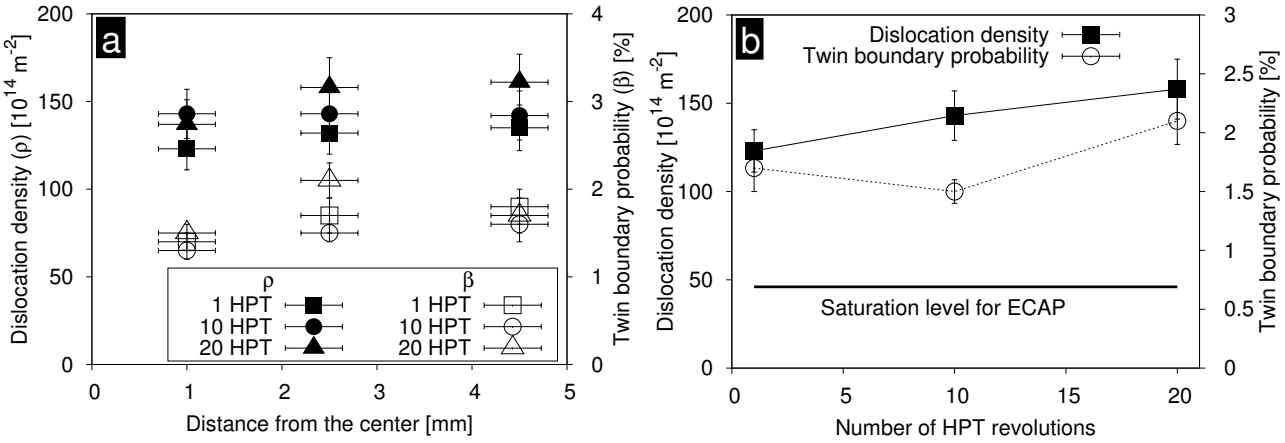

Figure 6.2: The dislocation density (solid symbols) and the twin boundary frequency (open symbols) as a function of the distance from the center of the HPT disks for different numbers of revolutions (a). The dislocation density and the twin boundary frequency measured at the half-radius of the disks as a function of number of HPT revolutions (b). On the bottom of subfigure (b) the saturation dislocation density and twin boundary frequency achievable by ECAP is marked.

6.2a. It can be seen that the defect densities change only slightly along the radius of the HPT disks. Therefore, we take the values measured at the half-radius as representative for a certain number of revolutions and these values are plotted in figure 6.2b. The dislocation density and the twin boundary frequency reached very high values of $132 \pm 13 \times 10^{14}\,\mathrm{m}^{-2}$ and $1.7 \pm 0.2\%$, respectively, even after 1 revolution and they increased only slightly during further HPT-processing. The maximum dislocation density and twin boundary frequency at the half radius of the HPT disks were $154 \pm 13 \times 10^{14}\,\mathrm{m}^{-2}$ and $2.1 \pm 0.2\%$, respectively, reached after 20 revolutions.

The defect densities measured on the HPT samples are about three times larger than the saturation values for ECAP and they can be explained by the high applied pressure of $P = 6\,\mathrm{GPa}$. Previous reports [171] have shown that in the case of ECAP the magnitude of pressure can be approximated by

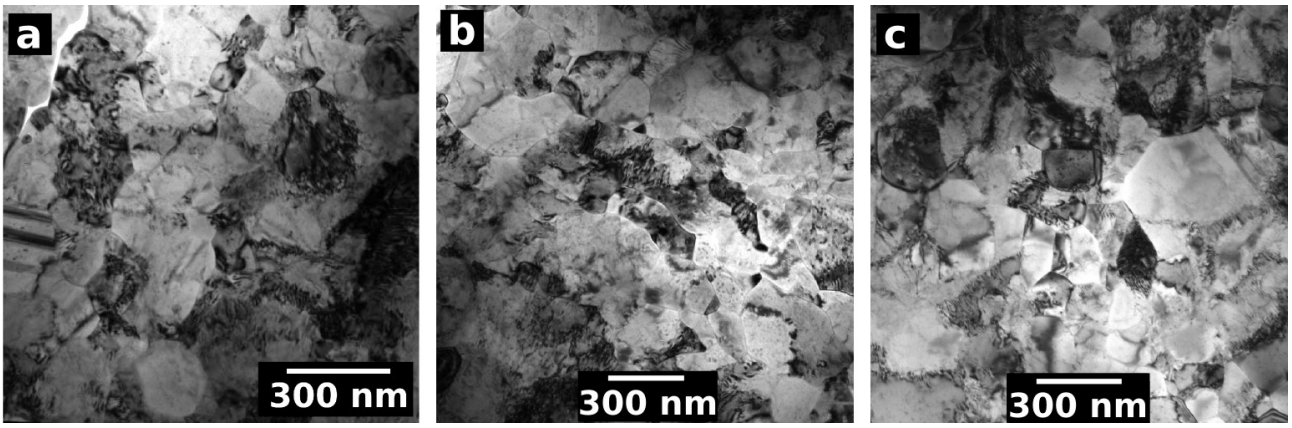

Figure 6.3: TEM images of the microstructures after 1 (a), 10 (b) and 20 (c) HPT revolutions.

the flow stress ($\sim$300 MPa for Ag, see figure 3.5, and 4.2) that is about one order of magnitude smaller than the applied pressure during HPT. The high pressure retards vacancy migration as the migration enthalpy is the sum of the migration energy ($E_{\mathrm{VM}} = 0.66$ eV [152]) and PV where V is the volume of a vacancy (9×10^{-30} m^3 in Ag calculated as the half of the volume per atom in the lattice). For HPT-processed Ag, $PV = 0.34$ eV which results in a five orders of magnitude smaller diffusion coefficient than in the case of ECAP as determined by a comparison of the values of the term of $\exp[-(E_{\mathrm{VM}} + PV)/kT]$, where k is the Boltzmann-constant and T is 300 K. This slower diffusion hinders the climb-controlled dislocation annihilation, resulting in very large dislocation density. Previous investigations [51] on Cu having a medium SFE revealed a similar ratio between the dislocations densities reached by HPT and ECAP. However, the twinning activity in Cu was not affected significantly by the pressure. The plastic deformation in low SFE Ag occurs by both dislocation slip and twinning. The twin faults usually form at glide obstacles, such as Lomer–Cottrell locks and grain boundaries where the local stress exceeds the critical stress required for twin nucleation. The number of these nucleation sites increases if the dislocation density is higher and this leads to a larger twin boundary frequency in the case of HPT compared with ECAP.

Figures 6.3 illustrate the microstructures after 1, 10 and 20 HPT revolutions. The mean grain size was 230 nm after 1 and 220 nm after 20 revolutions and that is very close to the saturation values determined for the ECAP-processed specimens (see chapter 3). This indicates that the lattice defect densities are more sensitive to the applied pressure than the grain size as was also observed for medium or high SFE fcc metals [51].

6.2 Thermal Stability of Silver Processed by High-pressure Torsion

The DSC thermogram obtained on a silver disk processed by 10 revolutions of HPT is shown in figure 6.4. Two overlapping exothermic peaks were detected between 400 and 500 K, which correspond to the recovery and recrystallization of the UFG microstructure. Without HPT processing there were no DSC peaks as the material was pure without any phase transformations. The first peak begins around 400 K and ends at $440 - 450$ K, where the second peak begins. The end of the second peak is at ~ 497 K. In order to reveal the reason for the double DSC peaks[3], samples were heat treated up to the temperatures corresponding to the end of the first peak, as well as to the middle and the end of the second peak (440, 460, and 497 K, respectively) at a heating rate of 10 K/min.

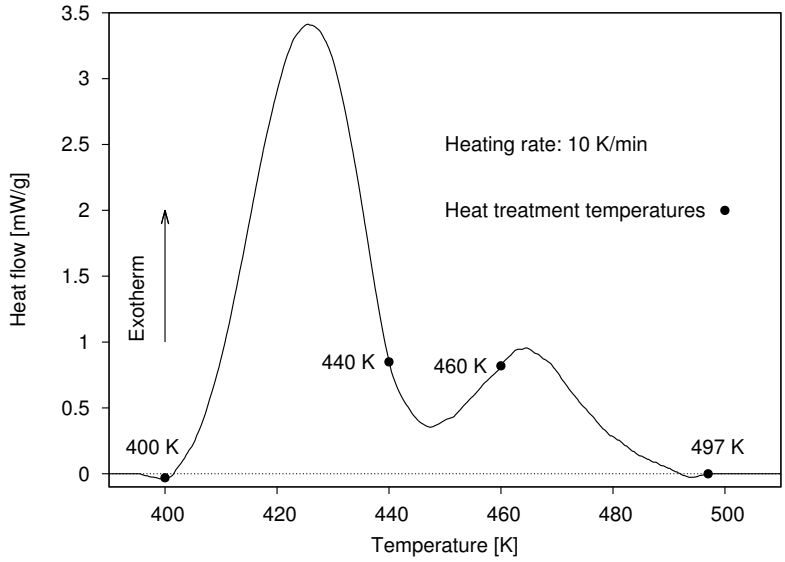

Figure 6.4: DSC thermogram obtained at a heating rate of 10 K/min for the sample processed by 10 revolution of HPT. The temperatures of heat treatments are indicated by solid circles.

Since the HPT processed microstructure only slightly changes along the diameter of the disk, it was suspected that the two DSC peaks were resulted by an inhomogeneous recovery/recrystallization of the UFG microstructure along the axial direction[4] of the disk. Therefore nanohardness maps (for details see subsection 2.3.1) were made on the cross sections of the HPT processed and the heat-treated disks. The nanohardness distributions are plotted as a function of the distance from the bottom surface in figure 6.5. It can be seen that after HPT the nanohardness distribution is homogeneous along the

[3] After ECAP there was only one exothermic peak during the DSC scan (see figure 5.1).

[4] prependicular to the surface

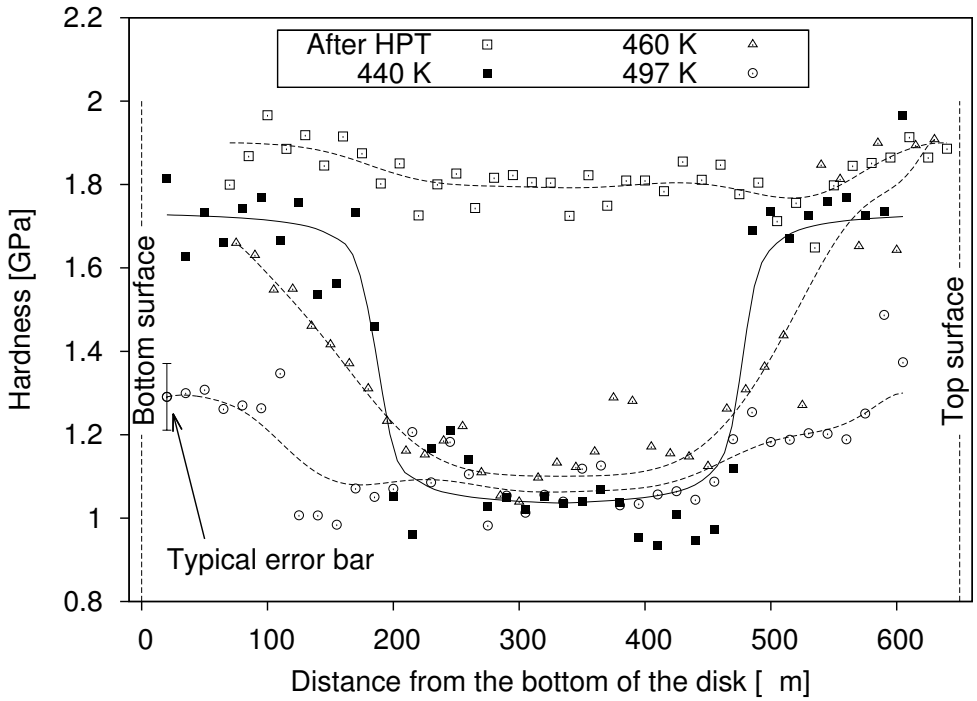

Figure 6.5: Nanohardness of the sample processed by 10 revolutions of HPT as a function of the distance from the bottom after different heat treatments. The solid and dashed lines are only guide to the eye. A typical error bar is also shown on the left side.

axial direction of the disk with a value of 1.8 ± 0.1 GPa. After annealing up to the first exothermic DSC peak, a relatively wide region of $250 - 300\,\mu$m in the middle of the disk shows a significant softening to a lower hardness value of 1.1 ± 0.1 GPa while the surface layers remain almost as hard as after HPT processing. There are clearly visible sharp transitions between the internal and surface regions. During the second exothermic peak (between 440 and 497 K), the surface regions of the disk also softened from about 1.8 GPa to 1.3 ± 0.1 GPa. However, the sharp transitions observed at 440 K disappeared at 460 K and instead the hardness increases almost linearly from the former transition layers to the surfaces. This result suggests that the softening of the surface region commences at the transition layers during the second exothermic peak.

The evolution of the grain structure during annealing of the HPT-processed disk was followed by EBSD on the cross section at the half radius[5]. Figures 6.6a and b show EBSD images with an inverse pole figure at the top right of figure 6.6b. These images were obtained after the heat treatments performed up to 400 and 497 K, respectively. The mean grain size was determined by averaging the equivalent circle diameters considering grain areas on EBSD images. At 400 K, the average grain size was ~ 170 nm throughout the sample if only the volumes with misorientations higher than 5° were

[5]The details of the EBSD investigations and the preparation of the surface is described in section 2.2

considered as separate grains. When this misorientation limit was increased to $15°$, the grain size value from EBSD evaluation increased to 200 nm. These values agree within the experimental error with those determined after HPT processing. After the second exothermic peak at 497 K, a fully recrystallized microstructure is observed throughout the disk with a characteristic grain size of $\sim 50\,\mu$m. The recrystallized grains contain a large number of subgrains with a size of $\sim 1\mu$m which are bounded by twin boundaries. The presence of these twinned volumes is explained by the very low twin boundary energy of silver.

Between the two exothermic peaks at about 440 K the nanohardness measurements showed a very narrow transition layer $\sim 170\,\mu$m under both surfaces of the disk (see figure 6.5). The EBSD image in figure 6.6c was taken in this region after the heat treatment up to 440 K. On the left side of figure 6.6c a part of a recrystallized grain with a size larger than the linear dimension of the image is shown. There are numerous small twin-oriented subgrains inside the large grain. The inset in figure 6.6c shows a higher magnification EBSD image of these fine subgrains taken from the designated square on the left of the dashed line. The right side of figure 6.6c corresponds to the surface region of the disk which remains as a UFG structure even after the heat treatment up to 440 K. The presence of a UFG structure is confirmed at the higher magnification in figure 6.6d. The average grain size values in the surface region at 440 K with misorientation limits of $5°$ and $15°$ were 165 and 180 nm, respectively.

In order to reveal whether any change took place in the surface region during the first exothermic peak, the grain size and the misorientation distributions in the surface layers were determined from the EBSD images at both 400 and 440 K and these results are plotted in figure 6.7. There are only negligible changes in the grain size and the misorientation distribution for the surface regions when the temperature increases from 400 to 440 K. The hardness and EBSD observations suggest that the first exothermic DSC peak is primarily caused by recovery and recrystallization in the middle of the disk, while the second peak corresponds to recovery and recrystallization of the surface regions of the HPT-processed disk. These results demonstrate that the UFG microstructure in the interior of the disk processed by 10 revolutions of HPT is less stable than the surface regions, leading to an inhomogeneous softening during the heat treatment in DSC. According to the nanohardness measurements, the volumes of the HPT-processed disk interior and the surface regions are very similar, however the released heat during the DSC scan was significantly smaller for the second peak corresponding to the recovery and recrystallization of the surface regions. This dichotomy can be explained by the remaining UFG volumes in the surface regions at 497 K as suggested by their slightly higher hardness compared to the values determined for the middle of the disk (see figure 6.5). Direct evidence for this assumption was not obtained, since the preparation of the surface by FIB limited the area to $100 \times 100\,\mu$m^2 investigated by EBSD. However, it was shown in section 5.2 for the same material processed by 4 passes of ECAP that 17% of the microstructure remained UFG even at high temperatures where no additional

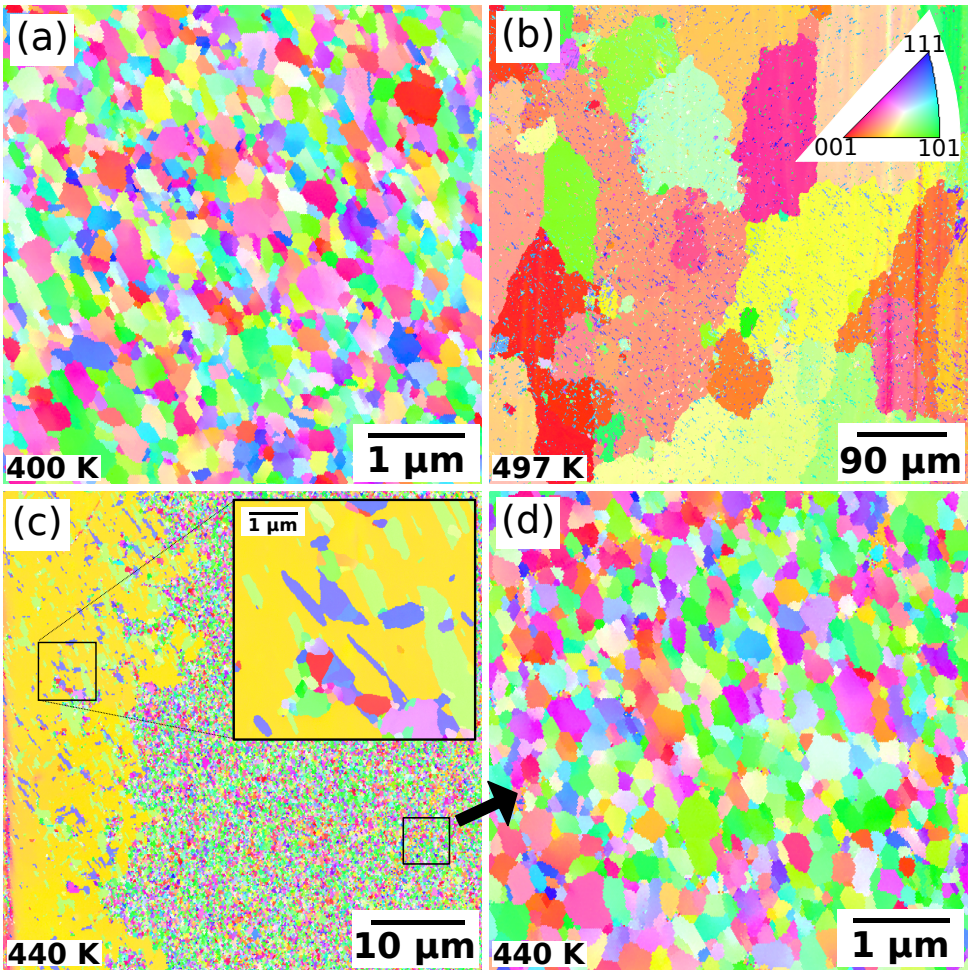

Figure 6.6: EBSD micrographs showing the UFG microstructure before the exothermic DSC peak at 400 K (a) and after the second peak at 497 K (b). The microstructure after the first DSC peak at 440 K is shown in (c) where the transition layer between the recrystallized interior and the UFG surface layer can be seen. The inset in (c) shows a part of the recrystallized grain in a higher magnification, illustrating that the large grain contains smaller twinned subgrains. A part of the UFG microstructure in the surface region is shown in a higher magnification in (d).

heat release was detected during annealing in DSC.

To investigate the reason for the gradient in the thermal stability in the axial direction of the HPT-processed disk, the characteristics of the microstructure were determined by XLPA as a function of the depth beneath the top surface. For this reason a sample was polished layer by layer with an Al_2O_3 suspension having a particle size of 1 μm in $\sim$100 μm steps and an x-ray diffractogram was recorded after each polishing step. The crystallite size, the dislocation density, and the twin-fault probability are shown at different locations from the top surface to the mid-plane of the disk in figure 6.8.

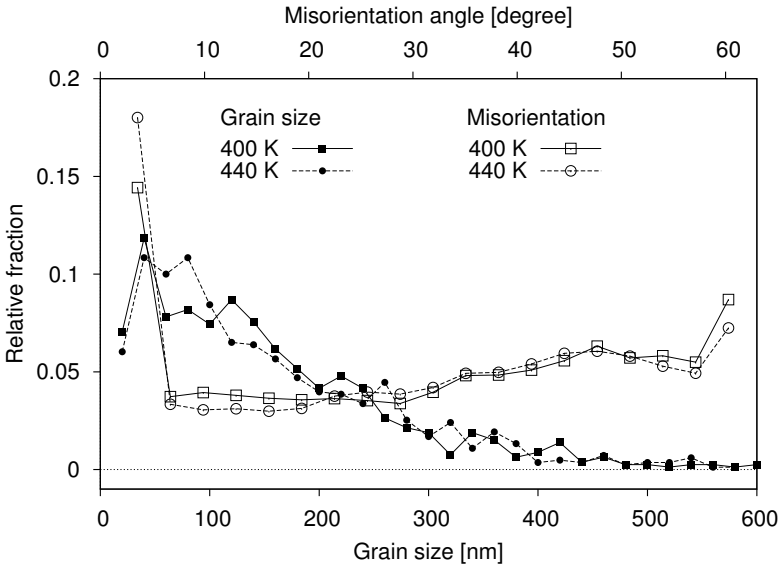

Figure 6.7: Grain size and misorientation angle distributions in the surface region before and after the first DSC peak at 400 and 440 K, respectively, as obtained from the EBSD images in figure 6.6a, d. In the determination of the grain size distribution, the volumes with misorientations higher than 5° were considered as separate grains.

These results provide clear evidence for axial inhomogeneity of the lattice defect structure in the HPT-processed sample. The average crystallite size, the dislocation density, and the twin-fault probability were 56 ± 6 nm, $109 \pm 11 \times 10^{14}$ m^{-2}, and $0.9 \pm 0.1\%$ at the top surface of the disk, respectively. In the surface layer with the thickness of $170\,\mu$m, the parameters of the microstructure did not change significantly. However, in the middle of the disk, at a distance of $300\,\mu$m from the surface, the dislocation density was lower ($79 \pm 9 \times 10^{14}$ m^{-2}) while the crystallite size (80 ± 9 nm) and the twin-fault probability ($1.6 \pm 0.1\%$) were larger than at the surface. Former studies [65, 129–131] have shown that plastic straining of low SFE fcc metals such as Ag, lattice dislocations are dissociated into twinning partials at glide obstacles such as Lomer–Cottrell locks or grain boundaries and consequently twins may then form by slipping of these partials in neighboring {111} lattice planes. The stronger twinning activity in the interior of the sample is most probably a consequence of the geometry of the quasi-constrained HPT processing facility since in the middle of the sample the metal can flow outwards during SPD while in the surface regions the material is constrained by the walls of the HPT anvils (see figure 6.1). The larger plastic straining in the middle of the sample most probably results in an increase of the number of glide obstacles where twinning may occur due to the large stresses [59].

In section 4.3 it is suggested that, in the volumes where the twin-fault probability increased at the expense of the dislocation density, the stored energy decreased due to the very low twin boundary energy of Ag. Thus, these volumes can act as nuclei for new defect-free grains during annealing, thereby

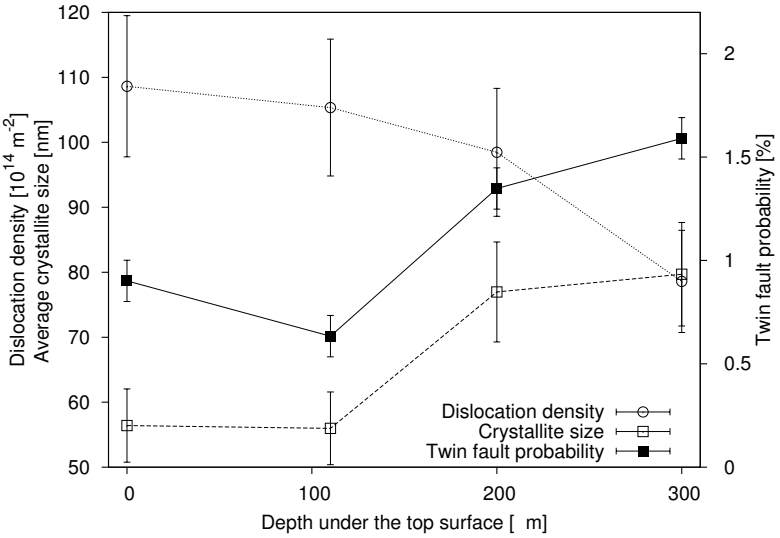

Figure 6.8: The average crystallite size, the dislocation density, and the twin-fault probability determined by x-ray line profile analysis as a function of the depth beneath the top surface.

reducing the time required for recrystallization in the middle of the HPT-processed Ag disk. The initiation of structural relaxation of the microstructure in the interior of the sample is also indicated by the larger crystallite size compared to the value determined in the surface region. It is noted that the crystallite size obtained by XLPA for metals processed by SPD is usually about $2-6$ times smaller than the grain size determined by TEM since the former quantity corresponds to the subgrain size [49]. Therefore, it is not necessary for the larger crystallite size in the middle of the disk to be accompanied by the larger grain size as obtained by EBSD. It should be noted that the nanohardness measurements and the microstructure investigations were performed only at the half-radius of the disk processed by 10 revolutions since in the previous section (6.1) it has been shown that the inhomogeneity in the hardness and microstructure in the radial direction is negligible even after 1 turn of HPT. The lack of a considerable variation in the microstructure along the radial direction indicates a saturation in the vicinity of the center of the disk processed by 10 HPT revolutions.

6.3 Discussion of the Thermal Stability of the HPT-processed Ag Samples

DSC scans for UFG fcc metals processed by SPD usually reveal only one exothermic peak in the thermograms. This peak corresponds to the recovery and recrystallization of the UFG microstructure. In the case of 99.998 and 99.99% purity Ni samples processed by HPT at RT, two exothermic peaks were

detected in the DSC thermograms [50, 83]. The first peak, appearing at a lower temperature of about 393 K at 10 K/min, corresponds to the disappearance of excess monovacancies while the larger second peak, at about 548 K, is associated with the annihilation of vacancy clusters and dislocations as well as recrystallization. The area under the first peak was about one order of magnitude smaller than for the second peak. The first 'monovacancy' peak was not observed for 99.99% Cu processed under the same conditions as most probably all the vacancies are clustered [50]. In the case of Ni, the high values of SFE and the high-melting point, together with the large pressures applied during HPT, retard the clustering of vacancies.

The single exothermic peak observed in the thermograms for the majority of SPD-processed UFG fcc metals indicates that the recovery and recrystallization occur at very close temperatures during DSC scans. However, when the UFG microstructure in Cu was obtained by the consolidation of powders using HPT technique, two exothermic peaks with similar areas were observed on the DSC thermogram [172]. The first and second peaks corresponded to the recovery and recrystallization of the microstructure, respectively. Both peaks appeared at higher temperatures than the single peak in the case of SPD-processed Cu. The more stable microstructure in the consolidated Cu sample is attributed to impurities and oxide dispersoids which are usually unavoidable in powder metallurgy. Thus, their pinning effect on grain boundaries is much stronger than on dislocations as suggested by the higher temperature of ~ 250 K for recrystallization compared to recovery in the sintered specimen.

In the case of the present HPT-processed Ag sample, the double DSC peak is not associated with the very different temperatures of the recovery and recrystallization processes but rather it is due to the difference between the thermal stability of the UFG microstructures in the middle and the surface regions of the disk. The variation of the temperature of recovery and recrystallization in the axial direction is caused by the change of the lattice defect structure. In the whole sample, extremely high-dislocation densities ($79 - 109 \times 10^{14}$ m^{-2}) were measured by comparison with the saturation values obtained for other pure fcc metals processed by HPT [49, 54, 173]. The very high- dislocation density is attributed to the low SFE of silver, as the annihilation of dislocations is hindered by the high degree of dislocation dissociation, as was discussed in the previous chapters. In low SFE metals such as Ag, twinning occurs at glide obstacles due to the large stresses [59].

In the middle of the disk the strain is larger than in the surface regions, as shown by model calculations [174], and this is due to the outflow of material between the anvils in quasi-constrained processing [175]. Therefore, in the interior of the disk it is anticipated that the number of glide obstacles is larger than in the surface regions, yielding larger twinning activity in accordance with the results of the present XLPA. It has been shown in section 4.3 that a larger twin-fault probability gave a weaker stability of the UFG microstructure against recrystallization. Therefore, in the middle of the disk where the twin fault probability is larger ($1.3 - 1.6 \pm 0.1\%$) than in the surface regions

$(0.7 - 0.9 \pm 0.1\%)$, the softening occurs at lower temperatures. Consequently, both the low SFE and the variation of the strain in the axial direction during HPT are necessary prerequisites for the observation of a double exothermic DSC peak. This is in accordance with the detection of a single DSC peak for pure Ag processed by ECAP (see figure 5.1). It should be noted that inhomogeneities in the microstructure lead to easier recrystallization in any deformed metallic material [176]. Thus, for low SFE silver the difference in the stored energies in the twinned and dislocated volumes causes the inhomogeneity in the microstructure.

Axial heterogeneity in hardness and microstructure has already been observed for other HPT-processed materials, such as pure Cu [174], an Al-Mg-Sc solid solution [177], Mg-alloys [178–180], and the Zr_3Al intermetallic compound [181]. However, in the AZ31 Mg alloy and in Cu the observations show higher hardness in the vicinity of the mid-plane of the sample and lower in the surface regions [174, 178–180]. These studies explained this phenomenon in terms of the smaller grain size in the middle of the sample caused by the higher strain which is probably caused by the outflow of the material between the anvils. In the case of pure silver, the higher strain near the mid-plane of the HPT disk caused easier softening during subsequent heat treatment.

As in the present Ag sample, the transition layers between the middle and surface regions in the AZ31 alloy and the Zr_3Al intermetallic compound were also very thin [179, 181]. The reason for the sharpness of these layers is not clear at the present time and requires further investigation. Nevertheless, it should be noted that the microstructure changes only slightly along the radial direction (see section 6.1) of the Ag disk either immediately after 10 revolution of HPT or after subsequent annealing. This suggests there is an early saturation of the dislocation density due to their strong dissociation because of the low SFE.

The Ag sample processed by HPT for one revolution showed a single exothermic peak during the DSC scan. The reason of the single exothermic peak is that the internal region of the sample processed by 1 turn was already recrystallized prior to the DSC experiment as confirmed by nanohardness measurements on the cross section, presented in figure 6.9. The thickness of this recrystallized volume and the hardness values of both the internal and surface regions in the disk deformed by 1 turn were very close to the values obtained for the sample processed by 10 turns of HPT after the first exothermic peak at 440 K. Therefore, the single exothermic peak obtained for the sample processed by 1 turn corresponds to the recrystallization of the surface regions and therefore it is similar to the second peak detected in the sample processed by 10 revolutions of HPT. The internal region of the sample processed by 1 turn may be recrystallized due to the increase of the temperature during HPT processing [47, 48] or due to transportation and storage before the investigation. In the sample deformed by 10 revolutions, the microstructure in the middle region remained UFG until the microstructural characterization

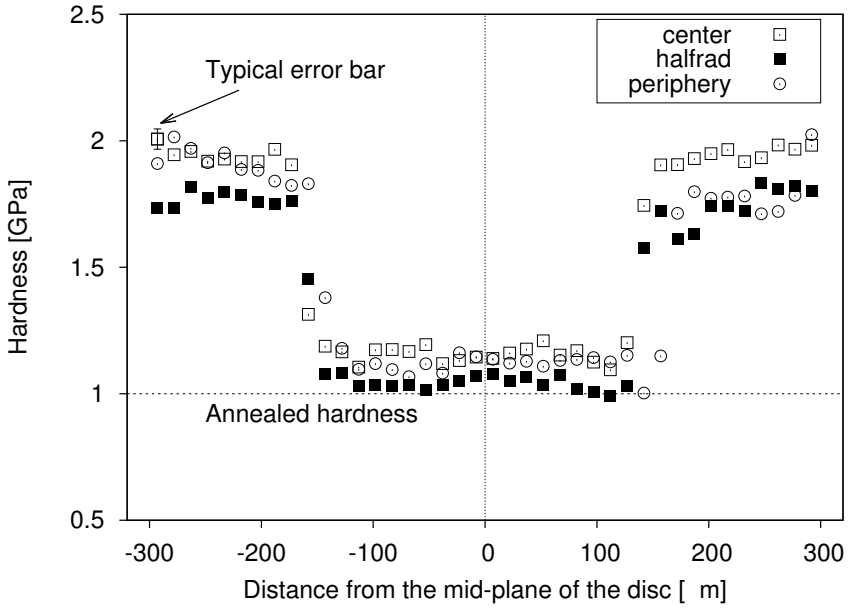

Figure 6.9: Nanohardness of the sample processed by 1 revolution of HPT along the axial direction. This time the x-axis shows the distance from the mid-plane of the disc. A typical error bar is shown on the left side.

which might be due to a shorter storage period at RT.

Figure 6.10 shows a SEM image of the cross section of the sample processed by 1 revolution of HPT and an EBSD micrograph illustrating the transition layer with the UFG region in the surface layer and the recrystallized interior region. Comparing figure 6.10b and 6.6c the similarity is obvious.

Summarizing this chapter, it has been shown that in the HPT-samples, the dislocation density was much higher than in the ECAP-processed samples as the high pressure in HPT retarded vacancy diffusion and thereby impeded the annihilation of dislocations by climb. The samples processed by HPT exhibited very heterogeneous microstructure in the axial direction of the disks. Due to the axial inhomogeneity of the microstructure the thermal stability of the HPT-processed samples differ significantly from that of the ECAP processed samples. Namely, a 'sandwich-like' microstructure evolved, in which the thermal stability of the surface layers was better than that in the middle of the disks. This structure is most likely the consequence of the different imposed strain in the surfaces and the interiors of the samples, since the surface layers are quasi constrained states during the deformation process, while in the middle part the material can outflow between the anvils of the HPT device. This difference caused a higher rate of twinning in the middle of the disk, which led to a lower thermal stability compared to the ECAP samples.

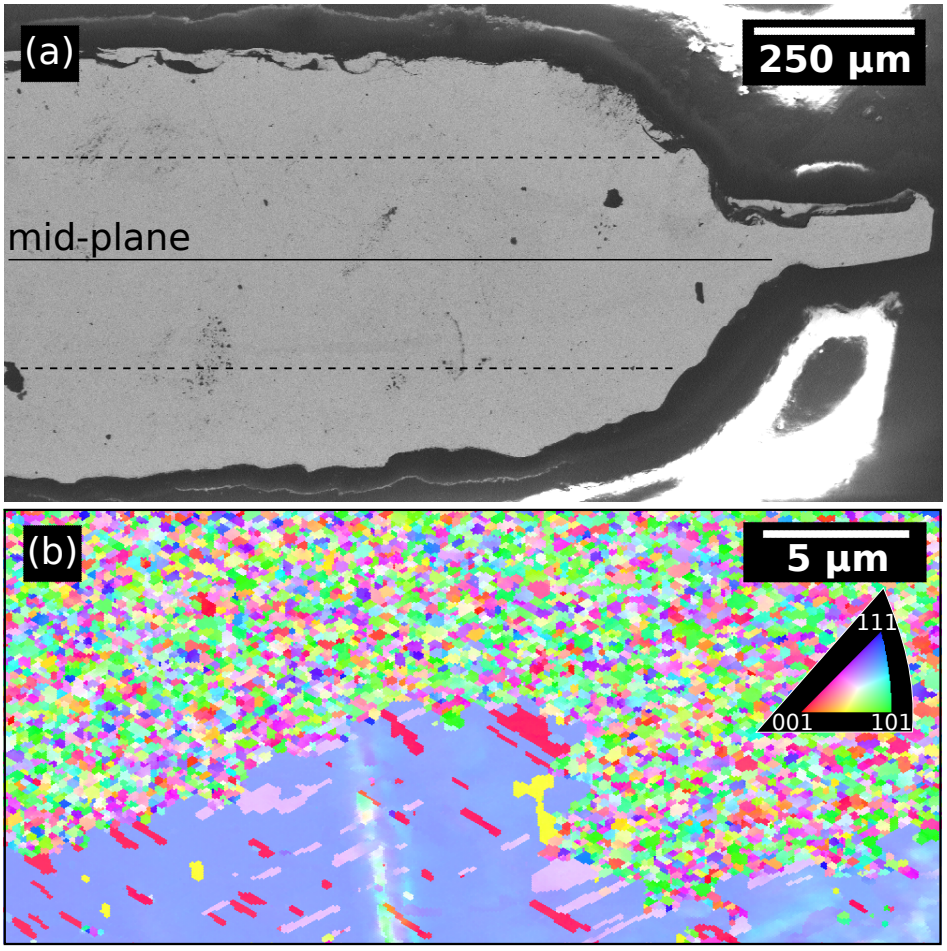

Figure 6.10: (a) SEM picture showing the cross-section of the sample processed by 1 revolution of HPT. The dashed lines represent the transition layer between the recrystallized internal and the UFG surface layers. (b) EBSD micrograph showing a magnified part of the transition layer.

Chapter 7

Microstructure of UFG Cu-Ag alloy Processed by Rolling and Subsequent Annealing [R12]

Until now we have seen the influence of the low SFE on the evolution of the UFG microstructure during ECAP and HPT deformation, as well as its effect on the low and high temperature thermal stability of the UFG microstructures in Ag. In this chapter, the microstructure and the mechanical behavior of an SPD-processed Cu-based alloy with Ag precipitates are studied. It will be shown that the combination of rolling at cryogenic temperature and subsequent annealing can yield heterogeneous microstructure which exhibits high strength and good ductility.

Deformation at cryogenic temperatures has been shown to produce UFG microstructures in many fcc metals and alloys [73–75, 77, 182, 183]. This is due to the suppression of dynamic recovery which helps in refining the microstructure. Recent results have shown that the effectiveness of cryogenic deformation (at liquid nitrogen temperature) in grain refinement depends on the SFE (as discussed in section 1.3) and there is an optimum SFE at which cryodeformation is very effective [184]. The UFG materials produced by the different SPD methods exhibit very high strengths but the tensile ductility is often very low (the uniform elongation is $< 2 - 3\%$). This is primarily due to the absence of work hardening, which in turn is due to the high defect density in the SPD-processed materials. The low ductility limits the industrial application of UFG materials.

In this chapter an approach for retaining high strength while recovering ductility is demonstrated. For this study a Cu-3 at.% Ag alloy, which is a precipitation-hardened material due to the very limited solubility of Ag in Cu at room temperature was selected. Figure 7.1 shows the Cu-rich part of the equilibrium phase diagram for the Cu-Ag binary system. The equilibrium solubility limit of Ag in Cu at room temperature practically zero. It should be noted that it is generally accepted that with decreasing grain size the solubility increases due to the increasing fraction of grain boundaries. However, a simulation study showed only a slight increase of the solubility of Ag in Cu at RT when the grain size decreased to the nanometer scale [185]. It is also noted that lattice imperfections (e.g. dislocations) were not included into this model, which may cause a further increase of the solubility of Ag in Cu at RT.

Additionally, the Cu-Ag alloy has medium SFE, and therefore twin formation is expected during both deformation and annealing. It has already been reported that a bimodal or multimodal

grain size distribution developed following short-time annealing at temperatures below recrystallization [73, 182]. Cu-Ag alloys are therefore suitable for combining approaches (i)-(iii) listed above in order to achieve high strength and good ductility. In the present investigation, severe cold rolling (SCR) at RT and cryogenic temperature (at liquid N_2 temperature (LNT)) followed by short-time annealing was employed to introduce fine deformation and annealing twins and precipitates in the microstructure. The microstructure and mechanical properties after rolling and annealing were studied and compared to other SPD-processed Cu-based alloys.

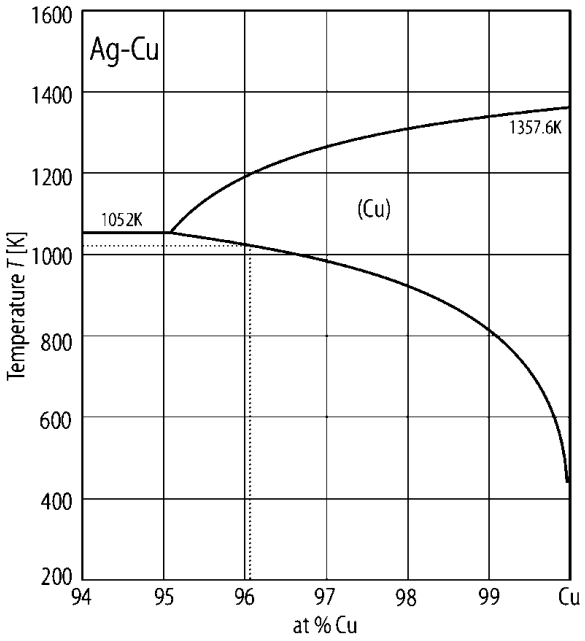

Figure 7.1: Cu-rich equilibrium phase diagram of the Cu-Ag binary system [186]. The temperature of the homogenization (750 °C $\approx$ 1023 K) and the corresponding solubility limit of Ag in Cu (about 4 at.%) is also shown.

Cu-3 at.% Ag alloy was prepared by induction melting (in Ar atmosphere) from high-purity (99.9%) elements and casting them into $15 \times 15 \times 150\,\mathrm{mm}^3$ graphite moulds. The alloy was homogenized at 750 °C for 5 h and quenched in water. The homogenized plates were subjected to rolling at RT and LNT (77 K). The plates subjected to cryorolling were dipped in liquid nitrogen for 15 min and were rolled from 15.5 mm to 2 mm thickness. The total thickness reduction was 85%, which corresponds to a true strain of ~ 2. It was achieved in multiple passes with about 10% reduction per pass. After each pass, the plate was immersed in liquid nitrogen for 2 min before further reduction.
Uniaxial tensile tests were conducted on selected samples using a mechanical testing machine (Instron 3367, UK) at an initial strain rate of $10^{-3}\,\mathrm{s}^{-1}$.

7.1 Recrystallization Studies of RT and LNT Rolled Cu-Ag Alloy

Recrystallization of RT and LNT rolled Cu-Ag samples was studied using DSC and microhardness measurements on isothermally annealed samples. Figure 7.2 shows the DSC thermograms of RT and LNT rolled Cu-Ag alloys. There is a major recrystallization peak at 420 °C and 450 °C for LNT and RT rolled alloys, respectively. The recrystallization temperature of the LNT rolled Cu-Ag alloy (400 °C) is significantly higher than that observed previously for LNT rolled Cu-11 at.% Al and Cu-4.9 at.% Zn alloys which showed recrystallization temperatures of 300 °C [77]. This indicates that Cu-Ag alloy has better thermal stability than the other two Cu alloys due to the smaller solubility limit of Ag in Cu which yields precipitation at grain boundaries, thereby hindering recrystallization.

There is another peak for both alloys at 320 °C; this is probably due to annihilation of vacancies.

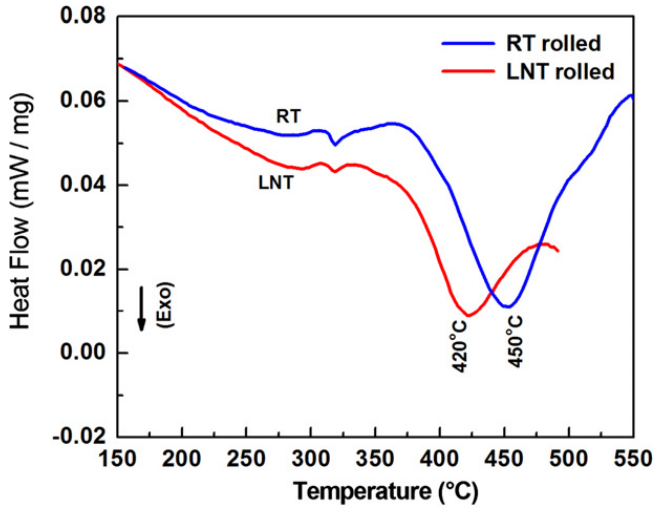

Figure 7.2: Heat flow obtained by differential scanning calorimetry at a heating rate of 10 K min^{-1} for the RT rolled and LNT rolled Cu-3 at.% Ag samples. Note that exothermic direction is downwards.

The recrystallization kinetics of RT and LNT rolled Cu-Ag alloys were evaluated using hardness tests on samples isothermally annealed to various durations. The Vickers microhardness measurements were performed on rolled and annealed (in the range of 375 − 450 °C for times of up to 30 min in air) samples using a microhardness tester (Matsuzawa MMT-7, Japan) with a load of 3 N and a dwell time of 10 s. Figure 7.3 shows the variation in hardness of RT and LNT rolled alloys after annealing in the temperature ranges of 375 − 450 °C for different times (5, 10, 15 and 30 min). The degree of recrystallization (X in vol.%) with time at a given temperature was calculated using the relation:

$$X\,(\%) = \frac{H_{\max} - H_{\mathrm{i}}}{H_{\max} - H_{\min}}, \tag{7.1}$$

where H_{max} is the maximum hardness (i.e. the hardness under as-rolled conditions), H_i is the hardness for the given temperature and time, and H_{min} is the minimum hardness (i.e. the hardness after annealing at the highest temperature for the longest duration). Evaluation of the hardness using equation 7.1 indicates that recrystallization kinetics is rapid in RT and LNT conditions at temperatures higher than $400\,°C$ and more than 90% of the volume is recrystallized within $10 - 15$ min of annealing. Recrystallization is much slower at 400 and $375\,°C$ in RT and LNT rolled samples, respectively (figure 7.3). These temperatures were therefore selected for further studies and a short-time annealing for 5 min was carried out. From the hardness results, it is estimated that about $15 - 20\%$ of the volume was recrystallized following the short annealing treatment. However, it is noted that recovery may also decrease the hardness in the beginning of annealing and therefore the recrystallized volume may be lower than the value estimated from the hardness reduction. It should also be noted that previous studies using a bimodal grain size approach have indicated an optimum coarse-grained volume of $15 - 30\%$ for achieving good ductility [182]. In addition to the bimodal microstructure, the short-time annealed samples of Cu-Ag alloy are expected to have fine Ag precipitates and annealing twins (due to the medium SFE of Cu and Cu-Ag alloy) in the recrystallized volume of the microstructure. In addition, there may be a partial recovery in the non-recrystallized regions of the specimens. The microstructures of the RT and LNT rolled samples and after subsequent annealing for 5 min at 400 and $375\,°C$, respectively, are studied by XRD, SEM and TEM as discussed below.

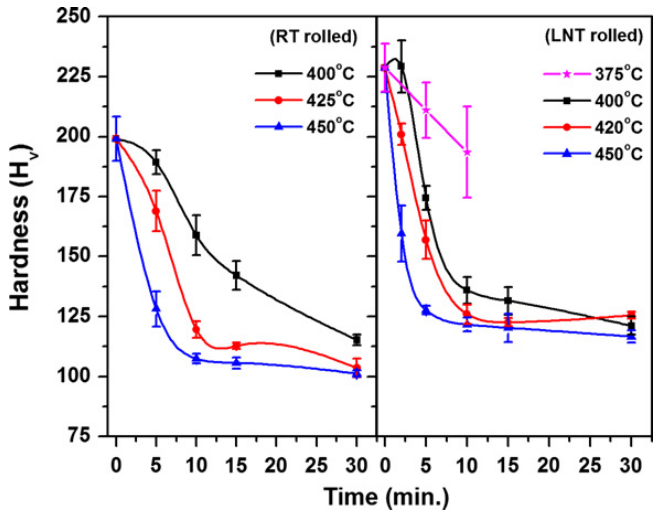

Figure 7.3: Variation of hardness (H_v) with annealing temperature and time for RT and LNT rolled Cu-Ag alloys (lines connecting data are only guide to the eye).

7.2 Microstructural Studies

7.2.1 X-ray Diffraction Analysis

The Ag solute content in Cu was determined from the lattice parameter measured by XRD. The values of the lattice parameter obtained for the Cu phase are listed in table 7.1. The lattice parameters of the Cu matrices in the samples rolled at RT and LNT are 0.3624 ± 0.0001 nm and 0.3622 ± 0.0001 nm, respectively. These values are significantly larger than the lattice parameter for pure Cu (0.3615 nm); this is most probably caused by the large solute Ag atoms in Cu. According to ref. [187], the lattice constant for dilute Cu-Ag alloys increases linearly with the Ag concentration and 1 at.% Ag in solution yields an increment of 0.0007 nm in the lattice parameter of Cu. From this, the Ag concentrations in the Cu matrix of RT and LNT rolled samples were estimated to be 1.3 ± 0.1 and 1.0 ± 0.1 at.%, respectively (see table 7.1). As the total concentration of Ag in the base alloy is 3 at.% (which corresponds to 5 wt.%), about 1.7 and 2 at.% Ag is expected to be present as secondary Ag phase in RT and LNT rolled alloys, respectively. Ag peaks were indeed observed in the XRD patterns of the as-rolled samples (see figure 7.4). According to the equilibrium phase diagram of the Cu-Ag system, the solubility limit of Ag in Cu is 4 at.% at 750 °C (the homogenization temperature in the present experiments), and therefore during the homogenization heat-treatment all Ag atoms were dissolved in the Cu matrix. Since only $1 - 1.3$ at.% Ag remained in solid solution following rolling at RT and LNT, it seems that Ag precipitates were formed during quenching and/or subsequent rolling tue to strain-induced precipitation.

Table 7.1: The lattice parameter (a) and the corresponding solute Ag concentration in the Cu matrix (c_{Ag}) of the Cu-3 at.% Ag alloy in RT rolled, RT rolled + annealed, LNT rolled and LNT rolled + annealed conditions. The error of the last digit of the lattice parameters is given in parentheses.

Sample	Region	a [nm]	c_{Ag} [at.%]
RT rolled		0.3624(1)	1.3 ± 0.1
RT rolled + annealed	1	0.3624(1)	1.3 ± 0.1
	2	0.3634(2)	2.7 ± 0.2
LNT rolled		0.3622(1)	1.0 ± 0.1
LNT rolled + annealed	1	0.3622(2)	1.0 ± 0.2
	2	0.3633(2)	2.6 ± 0.2

Table 7.2: The parameters of the microstructure for Cu matrix of the Cu-3 at.% Ag alloy in RT rolled, RT rolled + annealed, LNT rolled and LNT rolled + annealed conditions obtained by x-ray line profile analysis: the area-weighted mean crystallite size ($\langle x \rangle_{\text{area}}$), the dislocation density (ϱ) and the twin boundary frequency (β).

Sample	Region	$\langle x \rangle_{\text{area}}$ [nm]	ϱ [10^{14} m^{-2}]	β [%]
RT rolled		36 ± 4	32 ± 3	< 0.05
RT rolled + annealed	1	32 ± 4	14 ± 2	< 0.05
	2	41 ± 6	24 ± 3	< 0.05
LNT rolled		30 ± 3	48 ± 5	0.49 ± 0.07
LNT rolled + annealed	1	27 ± 3	8 ± 1	< 0.05
	2	55 ± 8	30 ± 4	< 0.05

The microstructural parameters of the Cu matrix in RT and LNT rolled samples were obtained by x-ray line profile analysis and are presented in table 7.2. As an example, the line profile fitting for the LNT rolled sample is shown in figure 7.4. The open circles and the solid line represent the measured data and the fitted curve, respectively. The peaks of Ag were not fitted and they were incorporated in the background during fitting. The crystallite sizes in the as-rolled conditions are about 30 nm, which is significantly smaller (by a factor of 2-5) than the crystallite sizes reported in pure Cu by different SPD methods [50, 51, 60]. This seems to indicate that the addition of Ag has promoted grain refinement by inhibiting recovery during SPD. It is noted that in SPD-processed metallic materials, the crystallite size is usually much smaller than the grain size obtained by TEM which can be attributed to the fact that the crystallites are equivalent to the coherently scattering domains. As the coherency of x-rays breaks even if they are scattered from volumes having quite small misorientations ($1 - 2^{\circ}$), the crystallite size corresponds rather to the subgrain size in the severely deformed microstructures [51]. Analysis of the microstructural parameters obtained from line profile analysis reveals that the crystallite size is smaller and the dislocation density is higher in the LNT rolled sample when compared to the RT rolled sample (table 7.2). Considerable twinning was not detected in the specimen rolled at RT while significant twin boundary frequency was measured in the LNT rolled sample. The practically zero value of the twin boundary frequency for the sample rolled at RT is not definitive proof of the lack of twinning as the lowest detection limit of twin boundary frequency is about 0.05% in the present analysis.

Following annealing of the RT and LNT rolled samples, each diffraction peak of the Cu matrix split into two components (see figures 7.5a and b). This phenomenon is believed to be caused by the development of an inhomogeneous solute atom distribution in the Cu matrix during annealing,

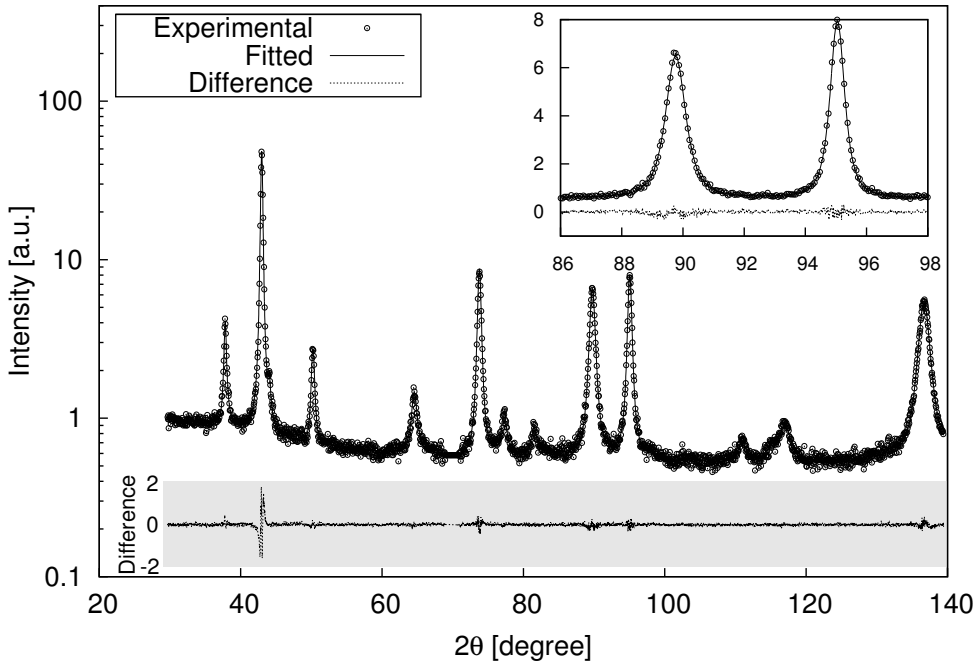

Figure 7.4: The CMWP fitting for LNT rolled Cu-3 at.% Ag. The open circles and the solid line represent the measured data and the fitted curves, respectively. The difference between the measured and fitted diffractograms is shown at the bottom of the figure. The inset presents a magnified part of the diffraction pattern.

resulting in a variation of the lattice parameters of the Cu matrices. Each line profile was evaluated by fitting with the sum of two profile components having different Bragg angles which correspond to two distinct regions of the matrix having different average lattice parameters. It should be noted that most probably the description of the distribution of the solute concentration by only two distinct solute contents is a simplification. Nevertheless, this procedure characterizes the inhomogeneity of the chemical composition of the matrix. The lattice parameters and the corresponding Ag solute concentrations for the two regions of the matrix have been determined and are listed in table 7.1. Region 1 has the same lattice parameter as for the matrix after rolling but before annealing. Region 2 has a significantly larger lattice parameter, indicating an increase in Ag solute concentration from 1.3 ± 0.1 to 2.7 ± 0.2 at.% and from 1.0 ± 0.1 to 2.6 ± 0.2 at.% during annealing of the RT and LNT rolled samples, respectively. The partial dissolution of the Ag phase is also confirmed by the decrease in the relative intensity of its XRD peaks. The equilibrium solubility limit of Ag in Cu at the temperature of annealing ($375 - 400\,^{\circ}$) is ~ 0.4 at.%, and therefore a decrease of the solute atom concentration from $1.0 - 1.3$ at.% during annealing of the rolled samples would have been expected. Our experiments revealed an opposite tendency, i.e. an increase in the solute Ag content in a part of the Cu matrix (region 2). The nanocrystalline microstructure (nanosized Ag particles in nanostructured

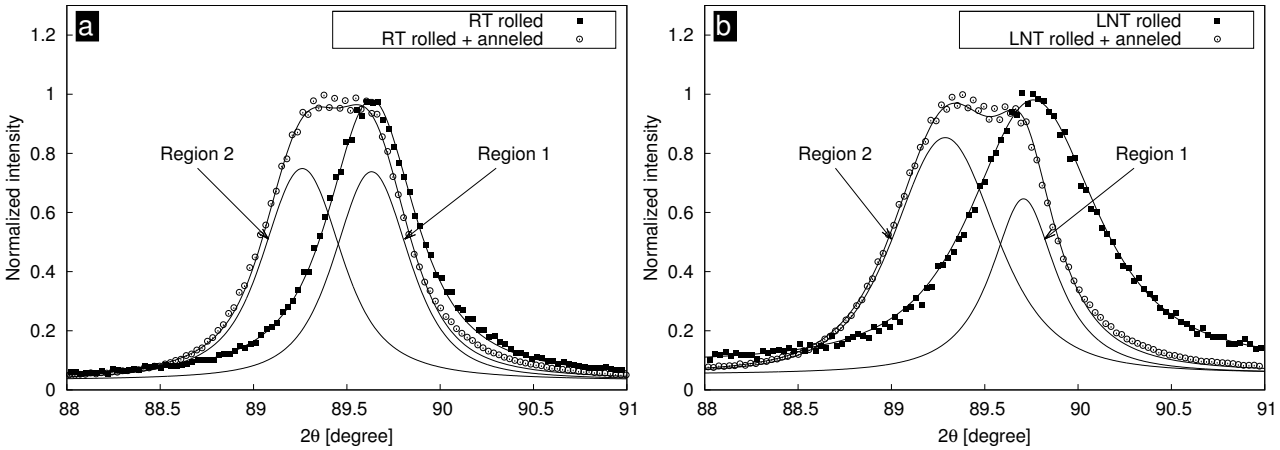

Figure 7.5: The CMWP fitting for 311 reflection of the Cu–3 at.% Ag samples for (a) RT rolled, and RT rolled and annealed, as well as (b) LNT rolled, and LNT and rolled and annealed conditions. The symbols and the solid lines represent the measured data and the fitted curves, respectively. The diffraction peak in annealed condition is a sum of two reflections related to regions 1 and 2 which have different average lattice parameters.

Cu matrix) developed during rolling could lead to a much higher solubility limit of Ag in Cu than predicted by the equilibrium phase diagram. Enhanced solubilities have been experimentally observed in nanocrystalline materials produced by different synthesis techniques [188, 189]. This phenomenon could be caused by the large specific interface energy of Ag nanoparticles, which raises the free energy, and consequently the equilibrium solubility is enhanced as [190]:

$$c_{\mathrm{r}} = c_{\infty} \exp\left(\frac{2\gamma V_{\mathrm{m}}}{rRT}\right), \tag{7.2}$$

where r is the radius of spherical Ag precipitates, T is the temperature of annealing ($\sim 670\,\mathrm{K}$), c_{∞} ($0.4\,\mathrm{at.\%}$) and c_{r} are the equilibrium solute Ag concentrations in the Cu matrix with Ag dispersoids having infinitely small curvature (large radius) and radius of r, respectively, c is the interface energy ($\sim 1.5\,\mathrm{J\,m^{-2}}$ [191]) between the Cu matrix and the Ag precipitates, R is the molar gas constant and V_{m} is the molar volume of Ag ($10^{-5}\,\mathrm{m^3/mol}$). This is often referred to as Gibbs-Thomson effect and becomes significant for precipitate diameters smaller than $10\,\mathrm{nm}$ [190, 192]. The average crystallite size of Ag particles was about 20 nm in the rolled samples as estimated from the breadth of XRD peaks of Ag, and for this size ($r = 10\,\mathrm{nm}$) the Gibbs-Thomson effect is not significant. The solute concentration observed in region 2 ($\sim 2.6\,\mathrm{at.\%}$) can be obtained from equation 7.2 only for the particles as small as $6\,\mathrm{nm}$. This suggests that the regions where the dissolution occurred (region 2) contained the smaller Ag precipitates ($< 6\,\mathrm{nm}$). This assumption is supported by the increase in the average size of Ag crystallites from ~ 20 to about $30\,\mathrm{nm}$ during annealing as observed by XRD. Another effect that may increase the solubility of Ag in Cu is the very high densities of lattice defects (e.g. grain bound-

aries and dislocations) in the rolled Cu matrices. These defects increase the free energy, which may be reduced by the replacement of Cu atoms by large solute Ag atoms at the dilated volumes around these defects as shown, for instance, in [163]. The decrease in free energy due to the replacement of Cu by Ag atoms at the defect sites may be larger than the increase in free energy due to the dissolution of Ag precipitates, and this could be the thermodynamic driving force for the increase in the solute Ag concentration in the rolled alloys during annealing. The Ag content in region 2 of the annealed samples is ~ 2.7 at.% at $\sim 400\,^{\circ}$C which is only slightly smaller than the nominal Ag concentration of the base alloy, suggesting that most of precipitates in region 2 were dissolved during annealing. Comparison of the integrated intensities under the x-ray peaks belonging to the two regions indicates that the volume fractions of region 2 where the dissolution occurred is similar to region 1 where the solute content did not change.

Regions 1 and 2 with different Ag contents obtained after annealing of RT and LNT rolled samples were investigated by x-ray line profile analysis. In the fitting of the experimental patterns, each theoretical line profile consisted of two peaks corresponding to the two regions. From the fitting, the microstructural parameters for regions 1 and 2 were determined and listed in table 7.2. The results reveal that in region 1 (with lower Ag content in the matrix) the crystallite size did not change significantly, while the dislocation density decreased by $\sim 60 - 80\%$ after annealing the RT and LNT rolled specimens for 5 min at 400 and 375 °C respectively. In region 2 (with higher Ag content in the matrix), the crystallite size increased slightly and the dislocation density decreased only by $\sim 25 - 40\%$ (see table 7.2). The lattice constants and the microstructural parameters suggest that during annealing of the rolled samples there was a competition between the dissolution of Ag precipitates and the recovery of the highly distorted microstructure. In the volumes where the dissolution of the precipitates was negligible (region 1), the solute Ag content remained low and the dislocation density decreased significantly due to recovery. However, the increased concentration of solute Ag atoms in region 2 hindered the recovery, resulting in retention of the high dislocation density. This is due to the pinning effect of the larger solute Ag atoms on dislocations in the Cu matrix, which inhibits their cross-slip and climb, two important mechanisms of recovery. On the other hand, the increase in the average size of Cu crystallites in region 2 can be explained by the growth of Cu crystallites into the volumes occupied formerly by the Ag precipitates, as discussed below.

7.2.2 Microscopy Analysis of the Microstructure

TEM images obtained on the RD-TD plane (RD: rolling direction; TD: transverse direction) of RT and LNT rolled samples are shown in figures 7.6a and b, respectively. These images reveal a cell-like

structure with a high dislocation density. The grain sizes of the Cu matrix estimated from the TEM images are in the range of $100 - 200$ nm in both the RT and LNT rolled specimens. The grain size obtained by TEM is about 3-6 times larger than the crystallite size determined by XRD as the latter quantity usually corresponds to the subgrain size in severely deformed microstructures [51]. Since Cu and Ag are metals with medium/low SFE, mechanical twinning is an important deformation mechanism. Also, since the concentration of Ag is low (< 8 wt.%), the alloy is less likely to deform through shear bands [193]. Study of the microstructure in ND-TD sections (ND: normal direction) of RT and LNT rolled samples revealed that, in addition to a high density of dislocations, deformation twins also formed in some locations of the specimens (see figures 7.6c and d). The twin spacing is smaller in the LNT rolled sample ($\sim 20 \pm 13$ nm) in comparison with the RT rolled specimen ($\sim 30 \pm 22$ nm). Dislocations were also found within the twinned regions. It is clear from the TEM investigations that the defect density is higher after rolling at LNT when compared with RT rolling and this is consistent with the XRD analysis (see table 7.2). However, the XRD results did not show considerable twin boundary frequency in the RT rolled sample, which suggests that twinning operates in only a few locations of the alloy during rolling at RT.

The microstructures of the RT and LNT rolled samples were also studied after annealing. The TEM micrographs of RT rolled and annealed (at $400\,^{\circ}$C for 5 min) and LNT rolled and annealed (at $375\,^{\circ}$C for 5 min) specimens are shown in figures 7.7a and b, respectively. The diffraction pattern obtained from the region shown in figure 7.7a is presented in figure 7.7c, revealing a more or less continuous ring-type pattern which is indicative of a fine-grained material with random local texture. The TEM image in figure 7.7d shows that annealing led to a significant recovery of the microstructure in some volumes of the RT rolled specimen. Mechanical twins were no longer observed but very fine annealing twins (with spacing in the range of $10 - 20$ nm) were detected. TEM results indicate that the grain size distribution after the short-time annealing is inhomogeneous containing UFG grains with a grain size of about 500 nm (see figures 7.7a and b) as well as nanostructured grains about $40 - 50$ nm in size (see figure 7.7d).

Figure 7.8 shows the EBSD image quality (IQ) map in the ND-TD section for the RT rolled sample after short-annealing. The IQ map reveals regions with higher pattern quality (bright regions in figure 7.8), indicating that these volumes have recovered/recrystallized during annealing. The analysis of the grain size distributions obtained from EBSD scans indicates that in both samples nearly 85% of the grains are $< 1\,\mu$m and there are a few extremely large grains with sizes of $\sim 10\,\mu$m in the ND-TD plane. EBSD analysis of the RD-TD planes (not shown here) indicated that the size of these large grains along the rolling direction is up to $100\,\mu$m. This further confirms the bimodal nature of the grain size distribution in the annealed samples. In comparison, EBSD studies on the as-rolled samples (not shown here) revealed that the grain size distribution was narrow, with 90% of grains being < 300 nm and

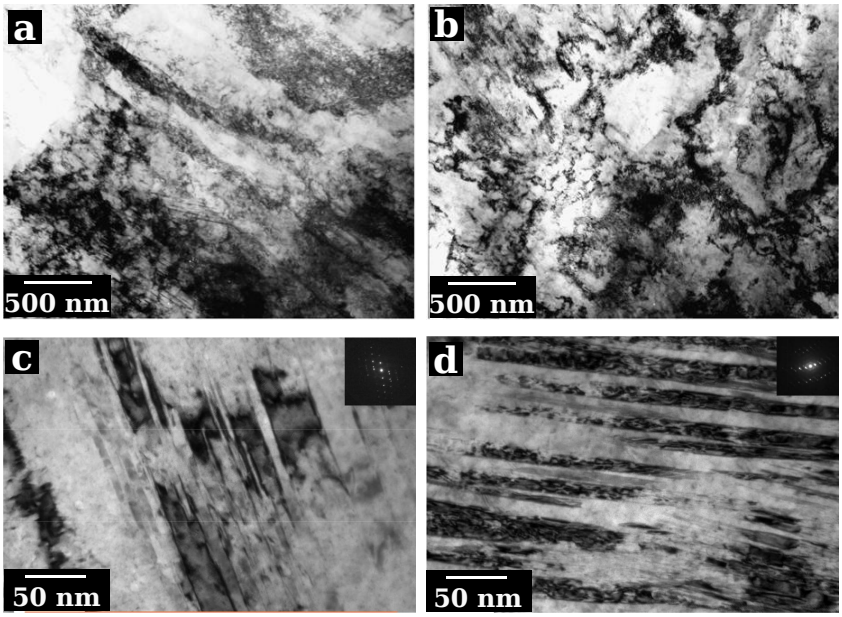

Figure 7.6: Bright-field TEM micrographs of Cu-3 at.% Ag alloys for (a) RT rolled condition in the RD-TD plane, (b) LNT rolled condition in the RD-TD plane, (c) RT rolled condition in the ND-TD plane (the inset shows the corresponding diffraction pattern) and (d) LNT rolled condition in the ND-TD plane (the inset shows the corresponding diffraction pattern).

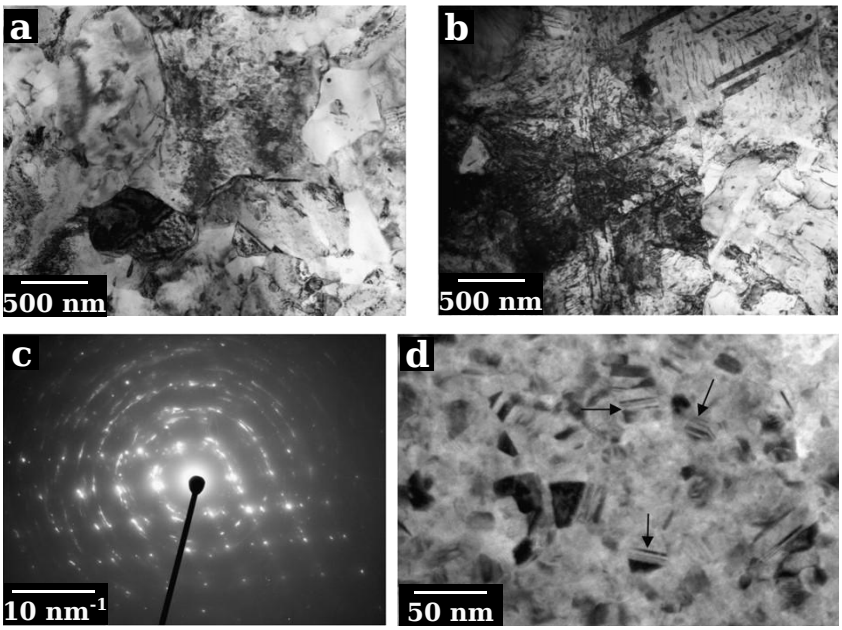

Figure 7.7: Bright-field TEM micrographs of Cu-3 at.% Ag alloy in the RD-TD plane for (a) RT rolled and annealed condition, (b) LNT rolled and annealed condition, (c) SAED pattern from the region shown in (a), and (d) image for RT rolled and annealed sample at higher magnification showing fine twins marked with arrows.

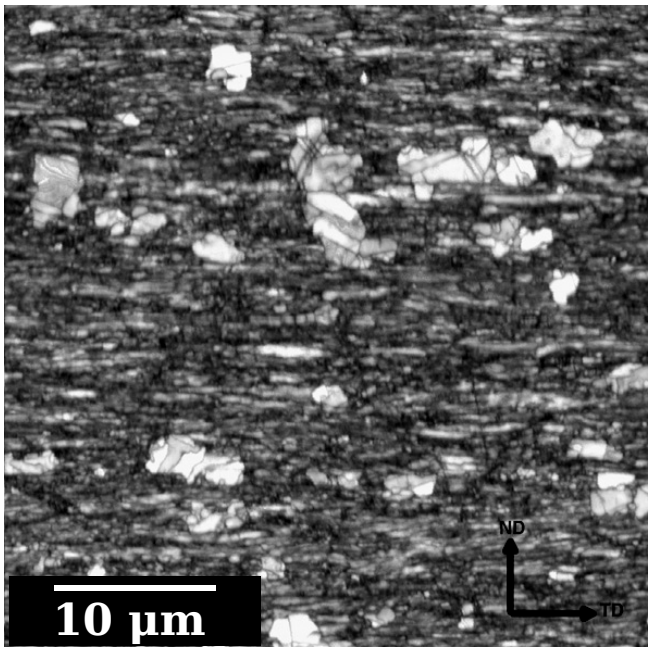

Figure 7.8: Electron backscatter diffraction image quality map for RT rolled and annealed Cu-3 at.% Ag samples.

only a few grains in the size range $1-3\,\mu$m. Analysis of misorientation angle distributions showed that the grain boundaries are predominantly low-angle boundaries with an average misorientation angle of 4° in the rolled samples, while after annealing the average misorientation angle increased to $\sim 12^\circ$.

To find microscopic evidence for the solute inhomogeneity observed in x-ray analysis (see subsection 7.2.1), backscattered SEM studies on LNT rolled as well as LNT rolled and annealed samples were carried out, as shown in figure 7.9a and b, respectively. The Ag precipitates appear bright in the figures due to atomic number contrast. These precipitates in the LNT rolled sample are more homogeneously distributed and some of them appear to be located along the grain boundaries (see the marked precipitates in figure 7.9a). Following annealing, one could identify distinct regions with and without Ag precipitates (marked as region 1 and region 2 in figure 7.9b) and the precipitates in region 1 are predominantly spherical with a size of $20-30\,$nm. Similar regions were also observed in RT rolled and annealed sample. These results are consistent with the x-ray line profile analysis in which an inhomogeneous solute distribution after annealing was detected. It may be noted that discontinuous or cellular precipitation is known to occur in coarse-grained Cu-Ag alloys during the ageing of the supersaturated solid solution [194,195]. Discontinuous precipitates with lamellar morphology were found predominantly at random high-angle grain boundaries due to the faster Ag diffusion along these boundaries [192,194]. Discontinuous precipitation has a deleterious effect on the mechanical properties and usually small amounts of a third element (e.g. Zr) are added to suppress it [195]. The high-angle

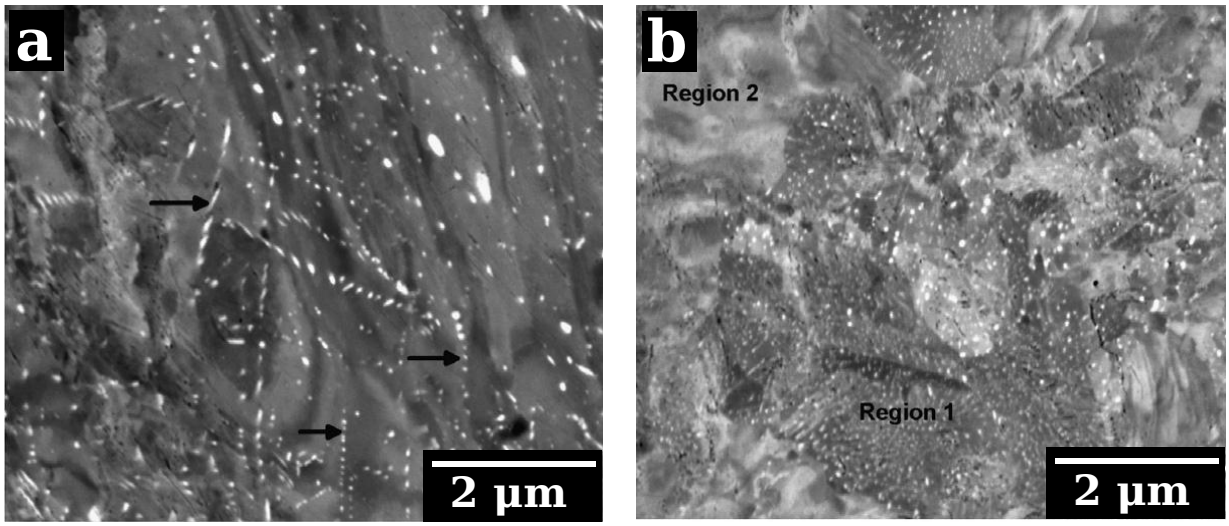

Figure 7.9: Backscatter SEM images of Cu-3 at.% Ag alloy in (a) LNT rolled condition and (b) LNT rolled and annealed condition. The aligned Ag particles along grain boundaries in (a) and the regions 1 and 2 with different solute content in the Cu matrix are indicated in (b).

annular dark-field (HAADF) image in figure 7.10a shows discontinuous precipitates (which appear in bright contrast) in some regions of the RT rolled and annealed sample. In the upper left corner of figure 7.10a, the white halo around the volume containing discontinuous precipitates (marked by a dashed curve) indicates large Ag solute content in the Cu matrix (corresponding to region 2), which was most probably formed by migration of the precipitation reaction front. This is referred to as discontinuous dissolution in which the receding discontinuous precipitation reaction front dissolves the second phase, resulting in discontinuous change in the composition across the reaction front. A schematic description of the discontinuous dissolution and the associated microstructural changes is shown in figure 7.10b. Discontinuous precipitation and discontinuous dissolution are a class of discontinuous reactions and these have been observed in many alloys, including the Cu-Ag system [196].

7.3 Mechanical Properties

The mechanical properties were studied by uniaxial tension at an initial strain rate of $10^{-3}\,s^{-1}$. Figure 7.11 shows the engineering stress-strain curves for RT rolled, LNT rolled and annealed samples. The RT and LNT rolled samples exhibit high ultimate tensile strengths (UTSs) with negligible uniform elongation ($\sim 1\%$). The strength of the RT rolled sample ($\sim 575\,MPa$) is $\sim 20\%$ less than that for the LNT rolled sample ($\sim 710\,MPa$). After annealing of the RT rolled sample, the UTS decreased

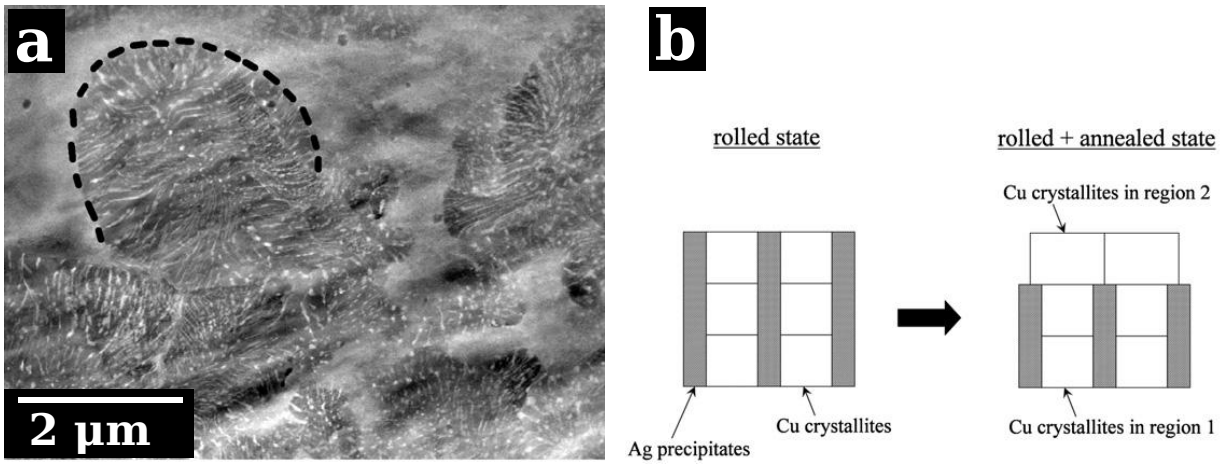

Figure 7.10: (a) High-angle annular dark-field TEM image of Cu-3 at.% Ag in RT rolled and annealed condition showing discontinuous Ag precipitates. The precipitation is outlined with dashed curve. (b) A schematic of discontinuous dissolution during the migration of the precipitation reaction front.

only slightly (by ~ 20 MPa) with significant improvement in the uniform elongation (from 1 to 10%). Similarly, annealing of the LNT rolled sample resulted in a decrease in the UTS by ~ 60 MPa and the ductility improved from 1 to 8%. The UTS obtained for the LNT rolled and annealed sample is ~ 90 MPa higher when compared to the RT rolled sample. The higher strength for LNT rolled Cu-Ag sample compared to RT rolled specimen can be attributed to the larger dislocation density and twin boundary frequency (see the XRD results in subsection 7.2.1). It was well documented that nanoscale twins improve the strength, as they are effective barriers to dislocation motion. It should be pointed out that there are two types of twins (annealing/growth twins and mechanical deformation twins) and the formation of both types is promoted by a decrease in SFE. The twin boundary strengthening was shown to follow a Hall–Petch-type relation as a function of the twin boundary spacing [81]. Refining the twin spacing through SPD has contributed to significantly enhanced strengths in pure Cu (~ 600 MPa following DPD) and in Cu-4.5 wt.% Al alloy (~ 900 MPa) but the tensile ductility was negligible [60, 76, 77, 81]. This is most likely due to the fact that deformation twins are incoherent and behave as a random high-angle grain boundary which does not promote strain hardening. On the other hand, decreasing the spacing of the growth/annealing twins (down to 15 nm) resulted in high strength and ductility in pulse electrodeposited Cu [78]. However, softening was observed when the twin boundary spacing was reduced to below 15 nm [197]. Analysis of strain hardening of the present annealed Cu-Ag samples using a Hollomon-type equation ($\sigma = K\varepsilon^n$) showed that the strain-hardening exponent n was 0.06 ± 0.01 for both rolled and annealed samples, indicating considerable work hardening. The increased strain-hardening capacity for the annealed samples compared to the

rolled samples could be attributed to (i) the formation of a bimodal microstructure as revealed by XRD, SEM and EBSD; and (ii) the formation of fine annealing twins as shown in TEM images. However, according to the XRD analysis, which examines a larger volume than TEM, extensive twin formation cannot be expected during short-time annealing of the rolled samples. Therefore, it appears that the bimodal microstructure developed during annealing is the main reason of the increase of ductility. It should be noted that the bimodal microstructure in the present alloy refers not only to the grain size distribution but also to the regions of varying solute content and dislocation densities. In other words, the recovery of ductility is most probably caused by the decrease of the dislocation density in region 1, which yields a considerable work hardening during subsequent tension, thereby increasing the uniform elongation compared to the rolled specimens. At the same time, in region 2 the increase of the solute Ag concentration during annealing hindered the annihilation of dislocations, and therefore the strength was only slightly reduced in comparison with the rolled samples.

A comparison of the stress–strain behavior of the present Cu-Ag alloys with previously published

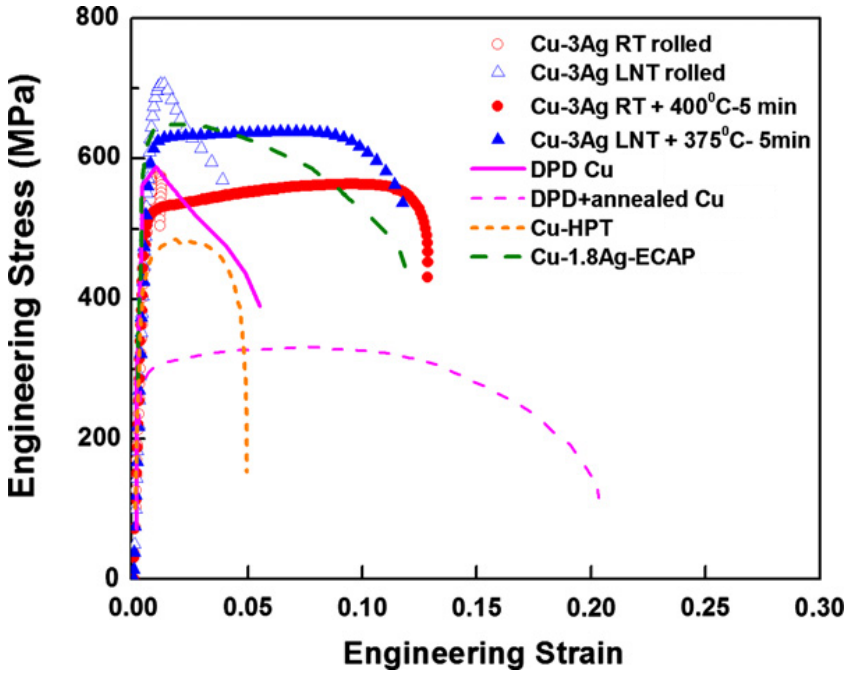

Figure 7.11: Engineering stress-strain curves for RT and LNT rolled as well as the annealed Cu-3 at.% Ag alloys. Stress-strain data taken from the literature for DPD Cu [82], DPD and annealed Cu [82], HPT-processed Cu [60], ECAP-processed Cu-1.8 at.% Ag alloy [198] are also included for comparison.

data on Cu and Cu-alloys processed by SPD methods is shown in figure 7.11. The stress-strain data of Cu (following DPD [82], DPD + annealed Cu [82], HPT for 5 revolutions at a pressure of 6 GPa [51,60]), Cu-3 wt.% Ag after 8 ECAP passes by route B_c [198]) are also included in the figure. From figure 7.11,

it is clear that RT/LNT rolled and annealed Cu-Ag alloys exhibit the best combination of strength and ductility. This is mainly due to development of a bimodal microstructure during annealing of SPD processed Cu- Ag alloys.

In summary, we demonstrated an approach for retaining high strength while recovering ductility in a Cu-3 at.% Ag alloy via cold rolling at room and cryogenic temperatures and short-time annealing just below the recrystallization temperature. After annealing, an inhomogeneous solute atom distribution developed in both Cu-Ag alloys due to the dissolution of nanosized Ag particles, resulting in regions with varying Ag content in the Cu matrix. In the region where the solute concentration increased, the dislocation density developed during rolling was retained in the Cu matrix even after annealing, while in the region where the Ag solute content did not increase, significant decrease in dislocation density was observed. Therefore, in the rolled and annealed samples, bimodal microstructures were developed where both the dislocation density and the solute concentration vary considerably. The as-rolled samples exhibited high ultimate tensile strengths close to $600 - 700$ MPa with negligible uniform elongation ($\sim 1\%$). After short-time annealing the strength decreased only by $\sim 20 - 60$ MPa with significant improvement in the uniform elongation (from 1 to 10%). This is attributed to the bimodal microstructure in the Cu matrix since the reduction of the dislocation density in some regions increased the strain-hardening capacity of the material.

New Scientific Results

The new scientific results can be summerized as follows:

1. The influence of impurities on the evolution of microstructure in Ag during ECAP-processing was investigated. The type and density of lattice defects were determined in 99.99 at.% (4N) and 99.995 at.% (4N5) purity silver. The minimum grain size achieved by ECAP in pure Ag was about 200 nm irrespective of the impurity atom concentration. The dislocation density also showed similar evolution for both 4N5 and 4N impurity levels: first it increased and saturated after 8 passes at similar values and then decreased. The saturation dislocation density was very large compared to other fcc metals due to the high degree of dislocation dissociation caused by the low SFE which hindered the annihilation of dislocations during SPD. The evolution of twin boundary frequency was very different for the two impurity concentrations: it increased monotonously up to 16 passes in the case of 4N5 purity samples while for 4N purity specimens it saturated after 4 passes and then decreased with increasing number of passes. The impurity atoms were most probably concentrated preferentially at the grain boundaries with decreasing grain size thereby hindering the emission of twinning partials from boundaries that led to a decrease of the twinning activity in the less pure material after 4 passes [R1–R4].

2. The samples processed for $4-16$ passes showed self-annealing (softening without heat-treatment) during storage at room temperature. Despite the small difference in purity, the 4N samples exhibited a much lower degree of softening than 4N5 specimens as impurity atoms pinned dislocations and grain boundaries thereby hindering both recovery and recrystallization. In the case of the 4N5 purity samples, an increasing number of ECAP passes led to a more rapid self-annealing due to the increase of the fraction of the twinned volumes that can act as nuclei for recrystallization. At the same time, the 4N purity specimen processed through 16 passes exhibited lower degree of softening than the samples processed through 4 or 8 passes, and this is due to the lower level of twinning [R2, R3, R5–R7].

3. The high temperature thermal stability of ECAP-processed 4N5 and 4N purity UFG silver were compared according to DSC experiments. The results showed that the activation energies for recovery and recrystallization were similar for both materials but the temperature of the exothermic DSC peak maximum was higher and the heat released was lower for the 4N purity sample. The primary contributions to the stored energy before recovery/recrystallization were given by the grain boundaries and the dislocations. A significant fraction of stored energy ($15-20\,\%$)

was retained in the samples after the exothermic DSC peak due to the remaining UFG regions and the high density of small dislocation loops. The reduced heat released for the 4N purity sample is primarily due to the lower vacancy concentration before the DSC peak, as compared to the 4N5 purity specimen. This phenomenon is attributed to a reduction of free volumes by segregation of dopants at the grain interfaces [R8, R9].

4. The minimum grain size achieved by SPD in 4N purity Ag was about 200 nm for both ECAP and HPT, i.e. its value is not very sensitive to the method of SPD. However, the retarding effect of the high pressure in HPT on the dislocation annihilation resulted in a $2-3$ times larger dislocation density than in ECAP-processing. The samples processed by HPT exhibited an inhomogeneous microstructure in the axial direction of the disk which resulted in spatially heterogeneous thermal stability of the UFG microstructure. During annealing in the middle of the HPT-processed disk the recrystallizaton occurred earlier than in the surface layers, which yield a double exothermic peak in the DSC thermogram. [R4, R10, R11].

5. The defect structure in Cu–3 at.% Ag alloy processed by cold rolling at room and cryogenic temperatures and subsequently annealed at high temperature was studied. After annealing, an inhomogeneous solute atom distribution developed in the Cu matrix due to the heterogeneous dissolution of nanosized Ag particles, resulting in regions with varying Ag content in the matrix. In the region where the solute concentration increased, the dislocation density developed during rolling was retained in the Cu matrix even after annealing, while in the region where the Ag solute content did not increase, significant decrease in dislocation density was observed. Therefore, in the rolled and annealed samples, bimodal microstructures were developed where both the dislocation density and the solute concentration vary considerably. The as-rolled samples exhibited high strength with negligible uniform elongation. After short-time annealing the strength decreased marginally with significant improvement in the uniform elongation. This is attributed to the bimodal microstructure in the Cu matrix since the reduction of the dislocation density in some regions increased the strain-hardening capacity of the material [R12].

Acknowledgements

First of all, I would like to thank my outstanding supervisor Prof. Jenő Gubicza, for his continuous assitance even for preparing this thesis or any of my manuscripts and presentations and without who I would have not started my doctoral studies.

I would also like to thank to Prof. Géza Tichy, for introducing me into the scientific work and also for his further help at any time.

Many thanks to my friends Gergely Markó and Péter Jenei, to all of my co-authors and Dr. Nguyen Quang Chinh, Dr. Zoltán Dankházi, Alajos Ö Kovács, Péter Szommer, Prof. Guy Dirras, Prof. Terence G. Langdon, Dr. Megumi Kawasaki, Zsolt Fogarassy, Dr. János L. Lábár and Gábor Varga. Contrary my endeavour this list is certainly not complete.

Special thanks to Krisztina Juhász for everything, and to my family (Anna, Antal, Orsi and András) for tolerating my varying mood during the hard periods.

Travelling grant from the Doctoral School of Eötvös Loránd University is also gratefully acknowledged.

My work was partially supported by the Hungarian Research Found (OTKA, project No. K81360) and the Hungarian Science and Technology (TÉT) project (project No. TÉT_10-1-2011-0737).

Abbreviations

4N	purity level of 99.99 at.%
4N5	purity level of 99.995 at.%
DSC	differential scanning calorimetry
EBSD	electron backscatter diffraction
ECAP	equal-channel angular pressing
eCMWP	extended convolutional multiple whole profile (fitting procedure)
fcc	face centered cubic
FIB	focused ion beam
HAGB	high angle grain boundary
HPT	high-pressure torsion
IQ	image quality
LAGB	low angle grain boundary
LNT	liquid nitrogen temperature
PAS	positron annihilation spectroscopy
RT	room temperature
SEM	scanning electron microscope
SFE	stacking fault energy
SPD	severe plastic deformation
TEM	transmission electron microscope
UFG	ultrafine-grained
XLPA	x-ray line profile analysis

Bibliography

[1] E. O. Hall, *Proceedings of the Physical Society. Section B* **64**, 747 (1951).

[2] N. Petch, *J. Iron Steel Inst.* pp. 25–30 (1953).

[3] Y. T. Zhu, T. C. Lowe, T. G. Langdon, *Scripta Materialia* **51**, 825 (2004).

[4] H. Gleiter, *Proceedings of the 2nd International Symposium on Metallurgy and Materials Science, Risø*, L. H. Hansen N, Horsewell A, Leffers T, ed. (National Laboratory, Denmark, Roskilde, 1981), p. 15.

[5] H. Gleiter, *Progress in Materials Science* **33**, 223 (1989).

[6] U. Erb, A. El-Sherik, G. Palumbo, K. Aust, *Nanostructured Materials* **2**, 383 (1993).

[7] M. J. Luton, C. S. Jayanth, M. M. Disko, S. Matras, J. Vallone, *MRS Proceedings* **132**, 79 (2011).

[8] R. Z. Valiev, R. R. Mulyukov, V. V. Ovchinnikov, *Philosophical Magazine Letters* **62**, 253 (1990).

[9] R. Valiev, N. A. Krasinikov, N. K. Tsenev, *Materials Science and Engineering: A* **137**, 35 (1991).

[10] R. Musalimov, R. Valiev, *Scripta Metallurgica et Materialia* **27**, 1685 (1992).

[11] Y. Estrin, A. Vinogradov, *Acta Materialia* **61**, 782 (2013).

[12] V. Segal, V. Reznikov, A. Drobyshevskiy, V. Kopylov, *Russian Metall (Metally)* **1**, 99 (1981).

[13] V. Segal, *Materials Science and Engineering: A* **197**, 157 (1995).

[14] V. Segal, S. Dobatkin, R. Valiev, *Russian Metall (Metally)* **2004**, 1.

[15] N. Smirnova, *et al.*, *Fizika Metallov i Metallovedenie* **61**, 1170 (1986).

[16] R. Valiev, O. Kaibyshev, R. Kuznetsov, R. Musalimov, N. K. Tsenev, *Proc. USSR Acad. Sci* **301**, 864 (1988).

[17] A. Zhilyaev, *et al.*, *Acta Materialia* **51**, 753 (2003).

[18] G. A. Salishchev, O. R. Valiakhmetov, R. M. Galeyev, *Journal of Materials Science* **28**, 2898 (1993).

[19] V. Valitov, G. Salishchev, S. K. Mukhtarov, *Izv. Ross. Akad. Nauk, Met.* **3**, 127 (1994).

[20] Y. Saito, N. Tsuji, H. Utsunomiya, T. Sakai, R. Hong, *Scripta Materialia* **39**, 1221 (1998).

[21] Y. Saito, H. Utsunomiya, N. Tsuji, T. Sakai, *Acta Materialia* **47**, 579 (1999).

[22] P. Gorria, J. A. Blanco, Loorentz, Y. G. Ko, *Journal of Alloys and Compounds* **536**, S122 (2012).

[23] Y. G. Ko, *Journal of Alloys and Compounds* **586**, S205 (2014).

[24] W. Polkowski, P. Jóźwik, M. Polański, Z. Bojar, *Materials Science and Engineering: A* **564**, 289 (2013).

[25] H. G. Jeong, Y. Jeong, D. J. Yoon, S. G. Choi, W. J. Kim, *Solid State Phenomena* **116-117**, 235 (2006).

[26] J. LIU, R. KAWALLA, *Transactions of Nonferrous Metals Society of China* **22**, s504 (2012).

[27] R. Z. Valiev, T. G. Langdon, *Progress in Materials Science* **51**, 881 (2006).

[28] K. Nakashima, Z. Horita, M. Nemoto, T. G. Langdon, *Materials Science and Engineering: A* **281**, 82 (2000).

[29] M. Furukawa, Y. Iwahashi, Z. Horita, M. Nemoto, T. G. Langdon, *Materials Science and Engineering: A* **257**, 328 (1998).

[30] M. Nemoto, Z. Horita, M. Furukawa, T. G. Langdon, *Metals and Materials* **4**, 1181 (1998).

[31] S. Lee, T. G. Langdon, *MRS Proceedings* **601**, 359 (2011).

[32] Y. Iwahashi, M. Furukawa, Z. Horita, M. Nemoto, T. G. Langdon, *Metall. Mater. Trans. A* **29**, 2245 (1998).

[33] Y. Iwahashi, Z. Horita, M. Nemoto, T. G. Langdon, *Acta Materialia* **46**, 3317 (1998).

[34] K. Oh-Ishi, Z. Horita, M. Furukawa, M. Nemoto, T. G. Langdon, *Metall. Mater. Trans. A* **29**, 2011 (1998).

[35] Y. T. Zhu, T. C. Lowe, *Materials Science and Engineering: A* **291**, 46 (2000).

[36] P.-l. Sun, P.-w. Kao, C.-p. Chang, *Metall. Mater. Trans. A* **35**, 1359 (2004).

[37] V. V. Stolyarov, Y. Zhu, I. V. Alexandrov, T. C. Lowe, R. Z. Valiev, *Materials Science and Engineering: A* **299**, 59 (2001).

[38] D. Yamaguchi, Z. Horita, M. Nemoto, T. G. Langdon, *Scripta Materialia* **41**, 791 (1999).

[39] H. S. Kim, *Materials Transactions* **42**, 536 (2001).

[40] A. Zhilyaev, T. G. Langdon, *Progress in Materials Science* **53**, 893 (2008).

[41] M. Degtyarev, T. Chashchukhina, L. Voronova, A. Patselov, V. Pilyugin, *Acta Materialia* **55**, 6039 (2007).

[42] A. Zhilyaev, *et al.*, *Acta Materialia* **51**, 753 (2003).

[43] F. Wetscher, A. Vorhauer, R. Pippan, *Materials Science and Engineering: A* **410**, 213 (2005).

[44] R. Islamgaliev, F. Chmelik, R. Kuzel, *Materials Science and Engineering: A* **237**, 43 (1997).

[45] C. Xu, Z. Horita, T. G. Langdon, *Acta Materialia* **55**, 203 (2007).

[46] A. Zhilyaev, K. Oh-ishi, T. Langdon, T. McNelley, *Materials Science and Engineering: A* **410-411**, 277 (2005).

[47] R. B. Figueiredo, P. H. R. Pereira, M. T. P. Aguilar, P. R. Cetlin, T. G. Langdon, *Acta Materialia* **60**, 3190 (2012).

[48] K. Edalati, R. Miresmaeili, Z. Horita, H. Kanayama, R. Pippan, *Materials Science and Engineering: A* **528**, 7301 (2011).

[49] J. Gubicza, *Defect Structure in Nanomaterials* (Woodhead Publishing Ltd., Cambridge, UK, 2012).

[50] D. Setman, E. Schafler, E. Korznikova, M. Zehetbauer, *Materials Science and Engineering: A* **493**, 116 (2008).

[51] J. Gubicza, S. Dobatkin, E. Khosravi, a.a. Kuznetsov, J. Lábár, *Materials Science and Engineering: A* **528**, 1828 (2011).

[52] E. Schafler, G. Steiner, E. Korznikova, M. Kerber, M. Zehetbauer, *Materials Science and Engineering: A* **410-411**, 169 (2005).

[53] J. Gubicza, S. Dobatkin, E. Khosravi, *Materials Science and Engineering: A* **527**, 6102 (2010).

[54] J. Čížek, *et al.*, *Acta Materialia* **59**, 2322 (2011).

[55] I. Kovács, L. Zsoldos, *Dislocations and plastic deformation* (Pergamon Press, London, 1973).

[56] L. E. Murr, *Interfacial Phenomena in Metals and Alloys* (Addison Wesley, Reading, 1975).

[57] D. Chung, W. Buessem, F. Vahldiek, S. Mersol, *Anisotropy in single crystal refractory compounds* (Plenum Press, New York, 1968).

[58] J. P. Hirth, J. Lothe, *Theory of Dislocations* (John Wiley and Sons Inc., New York, 1982), second edn.

[59] P. Müllner, C. Solenthaler, *Materials Science and Engineering: A* **230**, 107 (1997).

[60] Y. Zhao, X. Liao, Z. Horita, T. G. Langdon, Y. Zhu, *Materials Science and Engineering: A* **493**, 123 (2008).

[61] Y. H. Zhao, *et al.*, *Applied Physics Letters* **92**, 081903 (2008).

[62] H. Yang, X.-X. Wu, X.-Y. San, L. Shen, X.-K. Zhu, *Procedia Engineering* **36**, 307 (2012).

[63] X.-y. San, X.-g. Liang, L.-p. Cheng, L. Shen, X.-k. Zhu, *Transactions of Nonferrous Metals Society of China* **22**, 819 (2012).

[64] C. Huang, *et al.*, *Materials Science and Engineering: A* **556**, 638 (2012).

[65] Z. Wang, *et al.*, *Scripta Materialia* **60**, 52 (2009).

[66] L. Balogh, *et al.*, *Acta Materialia* **56**, 809 (2008).

[67] Y. Wang, *et al.*, *Materials Science and Engineering: A* **527**, 4959 (2010).

[68] V. Yamakov, D. Wolf, S. R. Phillpot, H. Gleiter **50**, 5005 (2002).

[69] D. Wolf, V. Yamakov, S. Phillpot, a. Mukherjee, H. Gleiter, *Acta Materialia* **53**, 1 (2005).

[70] S. Qu, *et al.*, *Acta Materialia* **57**, 1586 (2009).

[71] N. Tsuji, Y. Ito, Y. Saito, Y. Minamino, *Scripta Materialia* **47**, 893 (2002).

[72] F. Dong, *et al.*, *Materials Science and Engineering: A* **587**, 185 (2013).

[73] Y. Wang, M. Chen, F. Zhou, E. Ma, *Nature* **419**, 912 (2002).

[74] T. Shanmugasundaram, B. Murty, V. Subramanya Sarma, *Scripta Materialia* **54**, 2013 (2006).

[75] V. Niranjani, K. Hari Kumar, V. Subramanya Sarma, *Materials Science and Engineering: A* **515**, 169 (2009).

[76] W. Zhao, N. Tao, J. Guo, Q. Lu, K. Lu, *Scripta Materialia* **53**, 745 (2005).

[77] V. Subramanya Sarma, K. Sivaprasad, D. Sturm, M. Heilmaier, *Materials Science and Engineering: A* **489**, 253 (2008).

[78] L. Lu, Y. Shen, X. Chen, L. Qian, K. Lu, *Science (New York, N.Y.)* **304**, 422 (2004).

[79] K. Tao, *et al.*, *Applied Physics Letters* **90**, 101911 (2007).

[80] T. Lee, C. Chang, P. Kao, *Materials Science and Engineering: A* **408**, 131 (2005).

[81] Y. Zhang, N. Tao, K. Lu, *Acta Materialia* **59**, 6048 (2011).

[82] Y. Li, Y. Zhang, N. Tao, K. Lu, *Scripta Materialia* **59**, 475 (2008).

[83] D. Setman, M. B. Kerber, E. Schafler, M. J. Zehetbauer, *Metallurgical and Materials Transactions A* **41**, 810 (2010).

[84] T. Ungár, E. Schafler, P. Hanák, S. Bernstorff, M. Zehetbauer, *Materials Science and Engineering: A* **462**, 398 (2007).

[85] O. Mishin, a. Godfrey, *Metallurgical and Materials Transactions A* **39**, 2923 (2008).

[86] A. Zhilyaev, G. Nurislamova, S. Suriñach, M. Baro, T. G. Langdon, *Materials Physics and Mechanica* **5**, 23 (2002).

[87] J. Gubicza, *et al.*, *Journal of Alloys and Compounds* **378**, 248 (2004).

[88] J. Gubicza, L. Balogh, R. Hellmig, Y. Estrin, T. Ungár, *Materials Science and Engineering: A* **400-401**, 334 (2005).

[89] W. Cao, C. Gu, E. Pereloma, C. Davies, *Materials Science and Engineering: A* **492**, 74 (2008).

[90] Y. Huang, A. Menovsky, F. de Boer, *Nanostructured Materials* **2**, 587 (1993).

[91] B. Günther, A. Kumpmann, H.-D. Kunze, *Scripta Metallurgica et Materialia* **27**, 833 (1992).

[92] A. Zhilyaev, G. Nurislamova, R. Valiev, M. Baro, T. Langdon, *Metallurgical and Materials Transactions A* **33**, 1865 (2002).

[93] J. Čížek, *et al.*, *Physical Review B* **65**, 094106 (2002).

[94] a. P. Zhilyaev, *et al.*, *Physica Status Solidi (a)* **198**, 263 (2003).

[95] A. Zhilyaev, B. Kim, J. Szpunar, M. Baro, T. G. Langdon, *Materials Science and Engineering: A* **391**, 377 (2005).

[96] N. Lugo, N. Llorca, J. J. Suñol, J. M. Cabrera, *Journal of Materials Science* **45**, 2264 (2010).

[97] J. Lian, R. Z. Valiev, B. Baudelet, *Acta Metallurgica et Materialia* **43**, 4165 (1995).

[98] S. Tjong, H. Chen, *Materials Science and Engineering: R: Reports* **45**, 1 (2004).

[99] C.-M. Kuo, C.-S. Lin, *Scripta Materialia* **57**, 667 (2007).

[100] G. Wang, *et al.*, *Materials Science and Engineering: A* **346**, 83 (2003).

[101] Y. Estrin, *et al.*, *Acta Materialia* **54**, 5581 (2006).

[102] H. Matsunaga, Z. Horita, *Materials Transactions* **50**, 1633 (2009).

[103] J. Sólyom, *Fundamentals of the Physics of Solids: Volume 1: Structure and Dynamics* (Springer, 2007).

[104] J. I. Langford, D. Louër, P. Scardi, *Journal of Applied Crystallography* **33**, 964 (2000).

[105] A. Guinier, *X-ray diffraction in crystals, imperfect crystals, and amorphous bodies* (Dover Publications, INC., New York, 1994).

[106] J. Gubicza, J. Szépvölgyi, I. Mohai, G. Ribárik, T. Ungár, *Journal of Materials Science* **35**, 3711 (2000).

[107] B. E. Warren, B. L. Averbach, *Journal of Applied Physics* **23**, 497 (1952).

[108] M. Wilkens, *Fundamental Aspects of Dislocation Theory*, J. Simmons, R. DeWit, R. Bullough, eds. (National Bureau of Standards (US), Washington, DC, USA, 1969), pp. 1195–1221, spec. publ edn.

[109] T. Ungár, *Powder Diffraction* **23**, 125 (2012).

[110] T. Ungár, G. Tichy, *Physica Status Solidi (a)* **425**, 425 (1999).

[111] A. Borbély, I. C. Dragomir, G. Ribárik, T. Ungár, *Journal of Applied Crystallography* **36**, 160 (2003).

[112] G. Williamson, W. Hall, *Acta Metallurgica* **1**, 22 (1953).

[113] L. Balogh, Síkhibák karakterizációja röntgen vonalprofil analízis alapján köbös és hexagonális kristályokban, Ph.D. thesis, Eötövös Loránd University (2009).

[114] G. Ribárik, Modeling of diffraction patterns based on microstructural properties, Ph.D. thesis, Eötvös Lonránd University (2008).

[115] M. M. J. Treacy, J. M. Newsam, M. W. Deem, *Proceedings of the Royal Society A: Mathematical, Physical and Engineering Sciences* **433**, 499 (1991).

[116] G. Hölzer, M. Fritsch, M. Deutsch, J. Härtwig, E. Förster, *Physical Review A* **56**, 4554 (1997).

[117] L. Balogh, G. Ribárik, T. Ungár, *Journal of Applied Physics* **100**, 023512 (2006).

[118] R. Lyles, S. Rothman, W. Jäger, *Metallography;(United States)* **11**, 361 (1978).

[119] H. E. Kissinger, *Analytical Chemistry* **29**, 1702 (1957).

[120] J. B. Nelson, D. P. Riley, *Proceedings of the Physical Society* **57**, 160 (1945).

[121] P. Kirkegaard, M. Eldrup, O. E. Mogensen, N. J. Pedersen, *Computer Physics Communications* **23**, 307 (1981).

[122] P. Folegati, I. Makkonen, R. Ferragut, M. Puska, *Physical Review B* **75**, 054201 (2007).

[123] S. B. Shrivastava, H. P. Bonde, *Physica Status Solidi (b)* **88**, 269 (1978).

[124] T. Hehenkamp, *Journal of Physics and Chemistry of Solids* **55**, 907 (1994).

[125] P. Gallagher, *Metallurgical Transactions* **1**, 2429 (1970).

[126] J. Gubicza, S. Dobatkin, Z. Bakai, N. Q. Chinh, T. G. Langdon, *Materials Science Forum* **567-568**, 181 (2007).

[127] J. Gubicza, N. Q. Chinh, P. Szommer, A. Vinogradov, T. G. Langdon, *Scripta Materialia* **56**, 947 (2007).

[128] P. V. Liddicoat, *et al.*, *Nature communications* **1**, 63 (2010).

[129] J. Venables, *Philosophical Magazine* **6**, 379 (1961).

[130] J. B. Cohen, J. Weertman, *Acta Metallurgica* **11**, 996 (1963).

[131] Y. T. Zhu, X. Z. Liao, S. G. Srinivasan, E. J. Lavernia, *Journal of Applied Physics* **98**, 034319 (2005).

[132] F. D. Torre, *et al.*, *Acta materialia* **52**, 4819 (2004).

[133] Y. T. Zhu, *et al.*, *Applied Physics Letters* **95**, 031909 (2009).

[134] J. Friedel, *Dislocations and mechanical properties of crystals* (John Wiley and Sons Inc., New York, 1957).

[135] B. Escaig, *Journal de Physique* **29**, 225 (1968).

[136] A. N. Stroh, *Proceedings of the Royal Society A: Mathematical, Physical and Engineering Sciences* **223**, 404 (1954).

[137] G. Saada, *Journal de Physique III* **1**, 945 (1991).

[138] T. Ungár, M. Zehetbauer, *Scripta Materialia* **35**, 1467 (1996).

[139] A. Argon, W. Moffatt, *Acta Metallurgica* **29**, 293 (1981).

[140] R. Birringer, S. Schumacher, R. Strauß, H. Gleiter, *Acta Metall* **37**, 2485 (1989).

[141] J. Gubicza, N. Chinh, T. Csanádi, T. Langdon, T. Ungár, *Materials Science and Engineering: A* **462**, 86 (2007).

[142] N. Q. Lam, S. J. Rothman, H. Mehrer, L. J. Nowicki, *Physica Status Solidi (b)* **57**, 225 (1973).

[143] R. E. Hoffman, D. Turnbull, *Journal of Applied Physics* **22**, 634 (1951).

[144] H. P. Stüve, A. F. Padilha, F. Jr Siciliano, *Materials Science and Engineering: A* **333**, 361 (2002).

[145] H. Paul, J. H. Driver, C. Maurice, A. Piatkowski, *Acta materialia* **55**, 575 (2007).

[146] M. Kumar, A. J. Schwartz, W. E. King, *Acta Materialia* **50**, 2599 (2002).

[147] O. Mishin, J. Bowen, *Metallurgical and Materials Transactions A* **40**, 1684 (2009).

[148] M. Kawasaki, Z. Horita, T. G. Langdon, *Materials Science and Engineering: A* **524**, 143 (2009).

[149] S. D. Terhune, *et al.*, *Metall. Mater. Trans. A* **33A**, 2173 (2002).

[150] W. Skrotzki, *et al.*, *Acta Materialia* **55**, 2211 (2007).

[151] L. Chen, F. Spaepen, *Journal of Applied Physics* **69**, 679 (1991).

[152] R. W. Balluffi, *Journal of Nuclear Materials* **70**, 240 (1978).

[153] C. Hidalgo, S. Linderoth, d. N. Diego, *Physical Review B* **36**, 6740 (1987).

[154] H. Häkkinen, S. Mäkinen, M. Manninen, *Physical Review B* **41**, 12441 (1990).

[155] V. Gröger, *et al.*, *Materials Science Forum* **210-213**, 743 (1996).

[156] H.-E. Schaefer, R. Würschum, R. Birringer, H. Gleiter, *Physical Review B* **38**, 9545 (1988).

[157] K. Lücke, G. Gottstein, *Acta Metallurgica* **29**, 779 (1981).

[158] Y. Estrin, G. Gottstein, L. S. Shvindlerman, *Acta Materialia* **47**, 3541 (1999).

[159] L. S. Shvindlerman, *et al.*, *Journal of Materials Science* **41**, 7725 (2006).

[160] D. Wegner, *J. Phys. F: Met. Phys.* **18**, 2291 (1988).

[161] F. Humphreys, M. Hatherly, *Recrystallization and related annealing phenomena* (Elsevier, Oxford, 2004), second edn.

[162] D. Wolf, *Acta Metallurgica* **32**, 735 (1984).

[163] P. C. Millett, R. P. Selvam, A. Saxena, *Acta Materialia* **55**, 2329 (2007).

[164] M. Doyama, J. Koehler, *Physical Review* **127**, 21 (1962).

[165] L. J. Cuddy, E. S. Machlin, *Philosophical Magazine* **7**, 745 (1962).

[166] U. Klemradt, *et al.*, *Physical Review B* **43**, 9487 (1991).

[167] F. Haessner, G. Hoschek, G. Tölg, *Acta Metallurgica* **27**, 1539 (1979).

[168] B.-Z. Lee, C. Oh, D. Lee, *Journal of Alloys and Compounds* **215**, 293 (1994).

[169] J. Liu, C. Guo, C. Li, Z. Du, *Thermochimica Acta* **539**, 44 (2012).

[170] I. Karakaya, W. T. Thompson, *Journal of Phase Equilibra* **11**, 266 (1990).

[171] R. B. Figueiredo, P. R. Cetlin, T. G. Langdon, *Acta Materialia* **55**, 4769 (2007).

[172] P. Jenei, J. Gubicza, E. Yoon, H. Kim, J. Lábár, *Composites Part A: Applied Science and Manufacturing* **51**, 71 (2013).

[173] H. Zhang, X. Huang, N. Hansen, *Acta Materialia* **56**, 5451 (2008).

[174] H. J. Jeong, *et al.*, *Journal of Materials Science* **47**, 7828 (2012).

[175] Y. Song, E. Y. Yoon, D. J. Lee, J. H. Lee, H. S. Kim, *Materials Science and Engineering: A* **528**, 4840 (2011).

[176] O. Ivasishin, S. Shevchenko, N. Vasiliev, S. Semiatin, *Materials Science and Engineering: A* **433**, 216 (2006).

[177] G. Sakai, K. Nakamura, Z. Horita, T. G. Langdon, *Materials Science and Engineering: A* **406**, 268 (2005).

[178] R. B. Figueiredo, M. T. P. Aguilar, P. R. Cetlin, T. G. Langdon, *Metallurgical and Materials Transactions A* **42**, 3013 (2011).

[179] R. B. Figueiredo, T. G. Langdon, *Materials Science and Engineering: A* **528**, 4500 (2011).

[180] M. Kawasaki, R. B. Figueiredo, T. G. Langdon, *Journal of Materials Science* **47**, 7719 (2012).

[181] D. Geist, C. Rentenberger, H. Karnthaler, *Acta Materialia* **59**, 4578 (2011).

[182] Z. Lee, D. Witkin, V. Radmilovic, E. Lavernia, S. Nutt, *Materials Science and Engineering: A* **410–411**, 462 (2005).

[183] X. H. An, *et al.*, *Applied Physics Letters* **92**, 201915 (2008).

[184] V. Subramanya Sarma, *et al.*, *Materials Science and Engineering: A* **527**, 7624 (2010).

[185] G. Garzel, J. Janczak-Rusch, L. Zabdyr, *Calphad: Computer Coupling of Phase Diagrams and Thermochemistry* **36**, 52 (2012).

[186] P. R. Subramanian, J. H. Perepezko, *Journal of Phase Equilibria* **14**, 62 (1993).

[187] J. Song, H. Li, J. Li, S. Wang, S. Zhou, *Applied Optics* **41**, 5413 (2002).

[188] B. Murty, M. Datta, S. Pabi, *Sadhana (Academy Proceedings)* **28**, 23 (2003).

[189] F. Wu, P. Bellon, A. Melmed, T. Lusby, *Acta Materialia* **49**, 453 (2001).

[190] M. Perez, *Scripta Materialia* **52**, 709 (2005).

[191] F. Delogu, *The Journal of Physical Chemistry C* **114**, 19946 (2010).

[192] D. A. Porter, K. E. Easterling, M. Sherif, *Phase Transformations in Metals and Alloys* (CRC Press, Taylor & Francis Group, New York, 2009), third edn.

[193] A. Gaganov, J. Freudenberger, W. Grünberger, L. Schultz, *International Journal of Materials Research* **6**, 425 (2004).

[194] R. Wirth, H. Gleiter, *Acta Metallurgica* **29**, 1825 (1981).

[195] A. Gaganov, J. Freudenberger, E. Botcharova, L. Schultz, *Materials Science and Engineering: A* **437**, 313 (2006).

[196] I. Manna, *Interface Science* **6**, 113 (1998).

[197] L. Lu, X. Chen, X. Huang, K. Lu, *Science (New York, N.Y.)* **323**, 607 (2009).

[198] Y. G. Ko, S. Namgung, B. U. Lee, D. H. Shin, *Journal of Alloys and Compounds* **504**, S448 (2010).

Publications of the Author Related to This Thesis

[R1] J. Gubicza, N. Q. Chinh, J. L. Lábár, Z. Hegedűs, and T. G. Langdon, "Twinning and dislocation activity in silver processed by severe plastic deformation," *Journal of Materials Science*, vol. 44, pp. 1656–1660, Feb. 2009.

[R2] J. Gubicza, N. Q. Chinh, J. L. Lábár, Z. Hegedűs, and T. G. Langdon, "Unique Features of Ultrafine-Grained Microstructures in Materials Having Low Stacking Fault Energy," *Materials Science Forum*, vol. 659, pp. 171–176, Sept. 2010.

[R3] Z. Hegedűs, J. Gubicza, M. Kawasaki, N. Q. Chinh, Z. Fogarassy, and T. G. Langdon, "The effect of impurity level on ultrafine-grained microstructures and their stability in low stacking fault energy silver," *Materials Science and Engineering: A*, vol. 528, pp. 8694–8699, Nov. 2011.

[R4] Z. Hegedűs, J. Gubicza, M. Kawasaki, N. Q. Chinh, Z. Fogarassy, and T. G. Langdon, "Microstructure of low stacking fault energy silver processed by different routes of severe plastic deformation," *Journal of Alloys and Compounds*, vol. 536, pp. S190–S193, Sept. 2012.

[R5] J. Gubicza, N. Q. Chinh, J. L. Lábár, Z. Hegedűs, P. Szommer, G. Tichy, and T. G. Langdon, "Delayed microstructural recovery in silver processed by equal-channel angular pressing," *Journal of Materials Science*, vol. 43, pp. 5672–5676, July 2008.

[R6] J. Gubicza, N. Q. Chinh, J. L. Lábár, G. Tichy, Z. Hegedűs, C. Xu, and T. G. Langdon, "Stability of microstructure in silver processed by severe plastic deformation," *International Journal of Materials Research (formerly Zeitschrift für Metallkunde)*, vol. 100, no. 06, pp. 884–887, 2009.

[R7] J. Gubicza, N. Q. Chinh, J. L. Lábár, Z. Hegedűs, and T. G. Langdon, "Principles of self-annealing in silver processed by equal-channel angular pressing: The significance of a very low stacking fault energy," *Materials Science and Engineering: A*, vol. 527, pp. 752–760, Jan. 2010.

[R8] Z. Hegedűs, J. Gubicza, M. Kawasaki, N. Q. Chinh, Z. Fogarassy, and T. G. Langdon, "The Influence of Impurity Content on Thermal Stability of Low Stacking Fault Energy Silver Processed by Severe Plastic Deformation," *Materials Science Forum*, vol. 729, pp. 222–227, Nov. 2012.

[R9] Z. Hegedűs, J. Gubicza, M. Kawasaki, N. Q. Chinh, Z. Fogarassy, K. Süvegh, and T. G. Langdon, "High temperature thermal stability of ultrafine-grained silver processed by equal-channel angular pressing," *Journal of Materials Science*, vol. 48, pp. 1675–1684, Oct. 2012.

[R10] Z. Hegedűs, J. Gubicza, M. Kawasaki, N. Q. Chinh, J. L. Lábár, and T. G. Langdon, "Stability of the ultrafine-grained microstructure in silver processed by ECAP and HPT," *Journal of Materials Science*, vol. 48, pp. 12–19, Jan. 2013.

[R11] Z. Hegedűs, J. Gubicza, P. Szommer, N. Q. Chinh, Y. Huang, and T. G. Langdon, "Inhomogeneous softening during annealing of ultrafine-grained silver processed by HPT," *Journal of Materials Science*, vol. 48, pp. 7384–7391, July 2013.

[R12] K. Sitarama Raju, V. Subramanya Sarma, a. Kauffmann, Z. Hegedűs, J. Gubicza, M. Peterlechner, J. Freudenberger, and G. Wilde, "High strength and ductile ultrafine-grained Cu–Ag alloy through bimodal grain size, dislocation density and solute distribution," *Acta Materialia*, vol. 61, pp. 228–238, Jan. 2013.

Publications of the Author Unrelated to This Thesis

[U1] J. Gubicza, N. Q. Chinh, J. L. Lábár, Z. Hegedűs, C. Xu, and T. G. Langdon, "Microstructure and yield strength of severely deformed silver," *Scripta Materialia*, vol. 58, pp. 775–778, May 2008.

[U2] N. Q. Chinh, J. Gubicza, T. Czeppe, J. Lendvai, Z. Hegedűs, C. Xu, and T. G. Langdon, "Effect of Pre-Aging on the Microstructure and Strength of Supersaturated AlZnMg Alloys Processed by ECAP," *Materials Science Forum*, vol. 584-586, pp. 501–506, 2008.

[U3] J. Gubicza, N. Q. Chinh, J. L. Lábár, S. Dobatkin, Z. Hegedűs, and T. G. Langdon, "Correlation between microstructure and mechanical properties of severely deformed metals," *Journal of Alloys and Compounds*, vol. 483, pp. 271–274, Aug. 2009.

[U4] J. Gubicza, K. Máthis, Z. Hegedűs, G. Ribárik, and A. L. Tóth, "Inhomogeneous evolution of microstructure in AZ91 Mg-alloy during high temperature equal-channel angular pressing," *Journal of Alloys and Compounds*, vol. 492, pp. 166–172, Mar. 2010.

[U5] S. G. Chowdhury, J. Gubicza, B. Mahato, N. Q. Chinh, Z. Hegedűs, and T. G. Langdon, "Texture evolution during room temperature ageing of silver processed by equal-channel angular pressing," *Scripta Materialia*, vol. 64, pp. 1007–1010, June 2011.

[U6] G. Dirras, T. Chauveau, A. Abdul-Latif, J. Gubicza, S. Ramtani, Q. Bui, Z. Hegedűs, and B. Bacroix, "Ultrafine-Grained Aluminum Processed by a Combination of Hot Isostatic Pressing and Dynamic Plastic Deformation: Microstructure and Mechanical Properties," *Metallurgical and Materials Transactions A*, vol. 43, pp. 1312–1322, Dec. 2011.

[U7] K. Bobor, Z. Hegedűs, J. Gubicza, I. Barkai, P. Pekker, and G. Krallics, "Microstructure and mechanical properties of Al 7075 alloy processed by differential speed rolling," *Periodica Polytechnica Mechanical Engineering*, vol. 56, no. 2, p. 111, 2012.

– Summary –

Defect Structure in Ultrafine-grained Silver and a Copper-Silver Alloy Processed by Severe Plastic Deformation

Zoltán Hegedűs

Ultrafine-grained (UFG) materials are currently a major focus in materials science due to their unique properties in comparison to their coarse-grained counterparts. Specifically, an important feature of UFG materials is their high strength at ambient temperatures. Severe plastic deformation (SPD) methods, such as equal channel angular pressing (ECAP), high-pressure torsion (HPT) and rolling at liquid nitrogen temperature are effective tools for producing bulk UFG metals. The mechanical properties, such as the strength and ductility, are strongly affected by the lattice defect structure of UFG metallic materials. The evolution of the microstructure during SPD have been studied extensively for face-centered cubic (fcc) metals with medium or high stacking fault energies (SFEs). At the same time, a very little information is available on the defect structure in UFG fcc metals with low SFE. The main goal of my PhD work was to study the effect of low SFE on the evolution of lattice defects (e.g. dislocations and planar faults) during processing of the UFG microstructure by different SPD methods. The majority of the results presented in my thesis were obtained on silver as this material has the lowest SFE in pure fcc metals. The evolution of the defect structure as a function of strain applied in SPD was investigated for two impurity levels. The influence of impurities and the method of SPD (ECAP or HPT) on the room and high temperature thermal stability of the UFG microstructures were also studied. Additionally, the effect of the combination of cryogenic rolling and subsequent annealing on the microstructure and mechanical properties of a copper-silver alloy was studied.

It was obtained that a small change in the impurity concentration (from 0.005% to 0.01%) has only minor influence on the grain refinement and the increase of the dislocation density in ECAP-processed silver samples, but it has a strong effect on twinning. The evolved twin boundary probability was considerably higher in the purer sample, which affects significantly the thermal stability of the UFG microstructure. The highly twinned regions act as nuclei during recrystallization, therefore the purer sample showed self-annealing during room temperature storage. In the less pure silver only negligible recovery and recrystallization occurred in the same period of storage. According to high temperature investigations, there was no significant difference in the activation energy of recrystallization for the two impurity levels. However, the temperature of recrystallization was higher and the released heat was lower for the less pure sampe. The latter observation was explained by the smaller vacancy concentration in the less pure silver after ECAP.

It was shown that the saturation dislocation density in the HPT-processed silver was about 2-3 times higher than after ECAP. This can be attributed to the very high hydrostatic pressure applied during HPT, which retards the annihilation of dislocations. It was also revealed that in HPT-processed silver disks the lattice defect structure and the thermal stability varied along the axial direction of the disks. Hence, two exothermic peaks were detected during the calorimetric measurements: the recrystallization of the internal and the more stable surface regions in a disk give signals at lower and higher temperatures, respectively.

It was also shown that during the heat treatment of rolled Cu-Ag samples, heterogeneous microstructure evolved, because the very small (with the size of several nanometers) silver precipitates dissolved into the copper matrix, hereby increasing locally the solute silver atom concentration. In these regions, the higher alloying element concentration hindered the significant annihilation of dislocations during the heat treatment, while in other volumes a remarkable recovery took place. The evolution of this heterogeneous microstructure considerably improved the ductility of the alloy, as compared to the rolled material, while the strength only slightly decreased.

– Összefoglaló –

Nagymértékű képlékeny deformációval előállított ultrafinom szemcsés ezüst és réz-ezüst ötvözet rácshiba szerkezete

Hegedűs Zoltán

Az ultrafinom szemcsés (UFG) anyagok vizsgálata jelenleg az anyagtudomány egyik legaktívabb területe, köszönhetően az UFG anyagok kiemelkedő tulajdonságainak a nagyszemcsés anyagokhoz képest. Különösen fontos az UFG anyagok szobahőmérsékleti magas szilárdsága. A nagymértékű képlékeny deformációs (SPD) eljárások, mint például a könyöksajtolás (ECAP), a nagynyomású csavarás (HPT) vagy a hengerelés folyékony nitrogén hőmérsékleten, alkalmasak tömbi UFG anyagok előállítására. A mechanikai tulajdonságok, mint a szilárdság vagy az alakíthatóság, nagymértékben függenek az anyag rácshiba szerkezetétől. A mikroszerkezet fejlődését a nagymértékű képlékeny deformáció során részletesen megvizsgálták nagy és közepes rétegződési hibaenergiájú lapcentrált köbös (fcc) fémekben, ugyanakkor keveset tudunk az alacsony rétegződési hibaenergiájú fémek mikroszerkezetének kialakulásáról az SPD során. Munkám fő célja a különböző SPD eljárások hatására kialakuló hibaszerkezet (diszlokációk és síkhibák) tanulmányozása volt alacsony rétegződési hibaenergiájú fémekben. A vizsgálatok nagy részét ezüst mintákon végeztem, mert az ezüstnek van a legalacsonyabb rétegződési hibaenergiája a tiszta fcc fémek között. Tanulmányoztam a szennyezettségi szint, illetve az SPD módszer (ECAP vagy HPT) hatását az UFG mikroszerkezet fejlődésére és termikus stabilitására. Ezen kívül megvizsgáltam az alacsony hőmérsékletű hengerlés és az ezt követő hőkezelés hatását egy réz-ezüst ötvözet mikroszerkezetére és mechanikai tulajdonságaira.

Kutatásaim eredményeképpen megmutattam, hogy könyöksajtolt ezüstben a szennyezőtartalom kis mértékű növelése (0.005%-ról 0.01%-ra) csak csekély hatással van a szemcsefinomodásra és a diszlokációsűrűség növekedésére, ugyanakkor jelentősen befolyásolja az ikresedést. A tisztább anyagban nagyobb ikerhatár gyakoriság alakult ki, ami jelentős hatással volt a finomszemcsés szerkezet termikus stabilitására. Az erősen ikresedett tartományok nukleációs helyként funkcionálnak az újrakristályosodásban, így a tisztább mintában a szobahőmérsékleti hevertetés során önlágyulás következett be. A szennyezettebb anyagban ugyanannyi idő alatt megújulás vagy újrakristályosodás csak elhanyagolható mértékben jelentkezett. A magas hőmérsékleti vizsgálatok azt mutatták, hogy a különböző szennyezettségi fokú ezüst minták újrakristályosodásának aktiválási energiája között nincs mérhető különbség. Ugyanakkor az újrakristályosodás hőmérséklete magasabb, míg a hőkezelés során felszabadult tárolt hő kisebb a szennyezettebb minta esetén. Ez utóbbi megfigyelés oka, hogy a szennyezettebb mintában az ECAP után kisebb a vakancia koncentráció.

A kutatások során arra is fény derült, hogy ezüstben HPT-vel 2-3-szor nagyobb telítési diszlokációsűrűség érhető el, mint ECAP-pal. Ennek oka a HPT során alkalmazott nagy hidrosztatikus nyomás, ami akadályozza a diszlokációk annihilációját. Megmutattam, hogy HPT-vel alakított ezüst korongokban a felületre merőleges irányban változik a rácshibaszerkezet és ezzel együtt az ultrafinom-szemcsés mikroszerkezet termikus stabilitása is. Ennek következtében a pásztázó kaloriméteres mérésekben két exoterm csúcs jelentkezik: alacsonyabb hőmérsékleteknél a minta belseje, míg magasabb hőmérsékleteknél a nagyobb stabilitású felszíni rétegek megújulása és újrakristályosodása ad jelet.

Megmutattam, hogy hengerelt réz-ezüst ötvözet hőkezelése során heterogén mikroszerkezet alakult ki. Ennek oka, hogy a kis méretű (néhány nanométer átmérőjű) ezüst kiválások beoldódtak a réz mátrixba, ezzel lokálisan megnövelve az oldott ezüst koncentrációját. Ezekben a tartományokban a nagyobb ötvöző koncentráció megakadályozta a hengerlés során keletkezett diszlokációk nagy mértékű annihilációját a hőkezelés alatt, míg az anyag más részeiben jelentős megújulás ment végbe. Megállapítottam, hogy ez a heterogén mikroszerkezet jelentősen javította az ötvözet alakíthatóságát a hengerelt anyagéhoz képest, miközben a szilárdság csak kis mértékben csökkent.